Universität Leipzig
Fakultät für Physik und Geowissenschaften
Felix-Bloch-Institut für Festkörperphysik
Abteilung Angewandte Quantensysteme

Investigation of morphological changes of PMMA films during ion irradiation with high throughput imaging

Bachelor Thesis

presented by:
Mauricio Omar Bassallo Aguilar

Primary Referee: Prof. Dr. Jan Meijer
Second Referee: Dr.-Ing. Michael Kieschnick

September 20, 2019

Contents

1 Introduction **1**

2 Theoretical basics **2**
2.1 Polymethyl methacrylate (PMMA) . . . 2
2.2 Cleaning of silicon surfaces . . . 2
2.3 Spin coating . . . 5
2.4 Ion implantation . . . 7
2.4.1 Ion Stopping . . . 7
2.4.2 Ion range and Range Distribution . . . 10
2.4.3 Displacement and Radiation Damage . . . 12
2.4.4 Stopping and Range of Ions in Matter (SRIM) . . . 15
2.4.5 100 keV Ion Implanter . . . 17
2.5 Measurement equipments on surfaces . . . 19
2.5.1 Atomic Force Microscopy (AFM) . . . 19
2.5.2 DektakXT Stylus Profiler . . . 24
2.6 Optical Properties . . . 25
2.6.1 Refraction Index of Materials . . . 25
2.6.2 Interference in thin films . . . 27
2.7 Effects on the properties of PMMA due to ion implantation . . . 29
2.7.1 Effects on structural properties . . . 29
2.7.2 Effects on optical properties . . . 30

3 Experimental Methods **33**
3.1 Sample preparation . . . 33
3.1.1 Cleaning procedures of the silicon wafers . . . 33
3.1.2 Coating procedure of the silicon wafers . . . 35
3.2 Implantation . . . 36
3.3 Thickness and topography measurements . . . 37

4 Results and discussion **40**
4.1 Video Analysis of the implantations . . . 40
4.1.1 Color Change under different coating thicknesses . . . 41
4.1.1.1 Thicker samples . . . 41
4.1.1.2 Thinner samples . . . 45
4.1.2 Color Change under different ion energies . . . 50
4.1.3 Color Change under different ion species . . . 53
4.2 Topography of the PMMA surface . . . 56
4.2.1 Thickness change under ion irradiation . . . 56
4.2.2 Relation between the thickness change and the color change in PMMA . . . 59

5 Conclusions and Outlook **63**

6 Bibliography **65**

7 Appendix **67**
7.1 Appendix A: Table of the dose values before the decay of the intensity starts . . . 67
7.2 Appendix B: Table of coefficients of the fitting curves . . . 68

8 Acknowledgements **69**

9 Statement of authorship **70**

1 Introduction

Nastasi and Mayer [1] mention that ion beam processing of materials results from the interaction of atoms into the surface layer of a solid substrate by bombardment of the solid with ions in the electron-volt to mega-electron energy range. Mechanical, electrical, optical, magnetic, and superconducting properties all are affected by the presence of such foreign atoms. That makes the ion beam processing a tool used in several applications, such as in the manufacture of silicon-integrated circuits and in the improvement of some material properties (like, for instance, corrosion resistance, surface hardening, wear reduction, etc).

In some implantations just a limited area is available to work on it, so that in these cases it is required to use narrow beams. Beam sizes in the range of sub milimeters are achieved using small apertures. Nevertheless, the drawback of this beams is that, even though the flux density stays the same, the beam current drops heavily. Then, due to the small beam size, beam positioning also becomes a problem to solve. The common way in order to know where these micrometers ion beams have impacted in the wafer is coating a thin film on this one with some material, which is going to react with the beam creating a change of color in this film. The spin-coated thin film material commonly used as resist films is the PMMA (Polymethyl methacrylate), which is a well studied material used both in the industry (for instance, in micro/nanofabrication processes) and also in many other areas [2].

Many research have studied different properties of the PMMA under ion implantations. Research about the optical properties have shown that variables like refractive index [3; 4; 5] and transmittance [6] can change, even significantly. Also, research about structural properties mention that the implantations of ions can lead to degradation of the organic host of PMMA, modifying its structure in the affected zone by the implantation and leading it to another process called carbonisation [6; 7; 8]. These results could explain why there is a change of color during the whole implantation, or at least, in one part of the implantation. However, it is not clear how this change of color of the PMMA could behave under different parameters of implantations, like the thickness of the coating, the ion species, the energy of the ion and the dose.

In this context, it is useful to have a tool that allows to get information about the change of color during the whole implantation. A good option for that end is a video analysis of the ion implantation, which allows to compare, analyze and correlate the behaviour of the change of color with the different implantation parameters, like for instance the applied dose with the color obtained. Also, in order to contrast the information obtained from the video analysis with what happens on the implanted surface of PMMA, profilometer measurements after implantations would be also necessary.

For that end, in this research, different PMMA coating thicknesses on silicon (Si) wafers were used for three different implanted ions ($^{1}H^{-}$, $^{12}C^{-}$ and $^{74}Ge^{-}$), ion energies and doses. One video was recorded for each implantation and these ones were analized using a video analysis program. Finally, topography measurements of the implanted surfaces were carried out using equipments with a precision of 10 nanometers.

2 Theoretical basics

2.1 Polymethyl methacrylate (PMMA)

First of all, one has to take into account general considerations about the polymers. According to Fink [9], polymers are macromolecules built up of a large number of repeating molecular units, which are linked together by covalent bonds. The different molecules and separate segments of the same molecule are attracted to each other by intermolecular Van der Waals forces. The polymers also show a level of organization, where each level has some particular characteristics. In the case of PMMA, the first level (the "primary structure") is —-[CH_2—$C(CH_3)(COOCH_3)$]—. The methyl methacrylate monomers are produced from natural oil by means of acetone and cyanide acid. They can be polymerized to PMMA along several routes and the linkage along the length of the polymer backbone is —$\overset{|}{\underset{|}{C}}$—$\overset{|}{\underset{|}{C}}$— which is known as 'homopolymers' bounded by single bonds as it is shown in Figure 1:

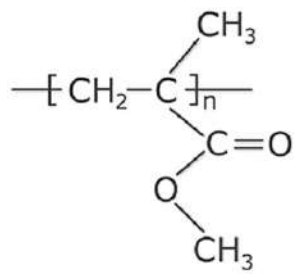

Figure 1: Monomer of PMMA

The PMMA homopolymers have a high hardness and stiffness, but they are brittle. This negative property can be avoided by copolymerization with elastomers such as polybutadiene. Copolymerization with styrenes yields optically clear modifications. PMMA is highly insulating. Its workability is excellent, however, it is inflammable. PMMA is highly transparent ($\backsim$ 92%) for visible light and even for UV. Some other important properties of PMMA are: its density around 1.17-1.20 g/cm^3, dielectric constants around 2.2-3.7 depending on the conditions, index of refraction of 1.49, among others [10].

2.2 Cleaning of silicon surfaces

Many of the sources that reference about the cleaning of Si surfaces are basically focused in getting the best cleaning as possible in order to use in the fabrication of semiconductor microelectronic devices. In these cases, a very clean surface has become critically important because trace impurities are especially detrimental during several steps in the production of these devices. For the purpose of coating with PMMA on Si surfaces, the level of cleaning is going to depend of the coating thickness and the minimum adherence needed for coating process. So the level of cleanliness used in the production of semiconductor devices is not required for the PMMA coating process. However, it is going to be necessary to ensure a sufficient cleaning in order to get a homogeneous PMMA coating on Si surfaces.

The impurities on silicon surfaces occur basically in three forms: (i) contaminant films, (ii) discrete particles, and (iii) adsorbed gases. According to Kern [11], the first two can be classified as

molecular compounds, ionic materials, and atomic species. For our purpose, we are more interested in the molecular compounds and ionic materials. Molecular compounds are mostly particles or films of condensed organic vapors from lubricants, greases, photoresist, solvent residues, components from plastic storage containers, and metal oxides or hydroxides. On the other hand, ionic materials comprise cations and anions, mostly from inorganic compounds that may be physically adsorbed or chemically bonded (chemisorbed), such as sodium ions, fluoride ions, and chlorine ions. Specially, about molecular contaminant films, Kern [11] mentions that these on surfaces can mask effective cleaning or rinsing, causing poor adhesion of deposited layers.

The most known procedure is the wet cleaning process called RCA (Radio Corporation of America) because it was developed there, introduced to device production in 1965 and published in 1970 by Kern and Poutinen [11]. The procedure is based on a two-step oxidizing and complexing treatment with hydrogen peroxide solutions: (i) an alkaline mixture at high pH followed by (ii) an acidic mixture at low pH. In the first step, the silicon wafers are exposed (or submerged, according to the original RCA) into a hot mixture of water-diluted hydrogen peroxide and ammonium hydroxide with the purpose of removing organic surface films by oxidative breakdown and dissolution to expose the silicon or oxide surface for concurrent or subsequent decontamination reactions. In the second step, the rinsed wafers are exposed (or submerged, according to the original RCA) to a hot mixture of water-diluted hydrogen peroxide and hydrochloric acid in order to remove alkali ions and cations such as Al^{+3}, Fe^{+3} and Mg^{+2} that form NH_4OH-insoluble hydroxides in basic solutions [11]. Itano et al. [12] concluded that the particle removal efficiency from silicon wafer surfaces is superior using alkaline solutions instead of acid solutions, suggesting that the mixing ratio of $NH_4OH - H_2O_2 - H_2O$ solution should be set at 0.05:1:5, and introducing the cold ultra pure rinsing between the $NH_4OH - H_2O_2 - H_2O$ cleaning and the hot ultra pure water cleaning in order to obtain both sufficient particle removal efficiency and surface smoothness of the wafers. Also, they explained the mechanism for removing particle adsorbed on the wafer surface with $NH_4OH - H_2O_2 - H_2O$ in the following way: the particles adsorbed on the wafer surfaces are first lifted off when the wafer surfaces are etched and then, these particles are electrically repelled from the surfaces by the alkaline solution (see Figure 2).

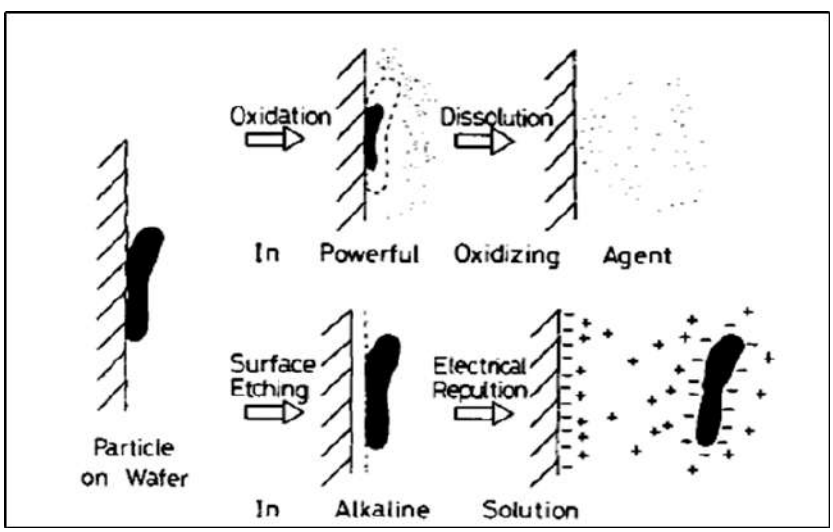

Figure 2: The mechanism of particle removal from the wafer surfaces by acid and alkaline solution [12]

Other cleaning procedures have been developed in the following years. One group of this cleaning procedure is the dry-cleaning techniques. In this group we can find methods like UV/Ozone cleaning and CO_2 snow cleaning.

The first one, the UV/Ozone cleaning procedure, is primarily the result of photosensitized oxidation processes. The contaminant molecules are excited and/or dissociated by the absorption of short wavelength UV light. Atomic oxygen and ozone are produced simultaneously when O^+ is dissociated by the absorption of UV with wavelengths less than 245.4 nm. Atomic oxygen is also produced when ozone is dissociated by the absorption of the UV and longer wavelengths of radiation. The excited contaminant molecules and the free radicals produced by the dissociation of contaminant molecules react with atomic oxygen to form simpler, volatile molecules, such as CO_2, H_2O, and N_2. Vig [13] concluded that the UV/ozone cleaning procedure is a highly effective method of removing a variety of contaminants from surfaces, which is a simple-to-use dry process, inexpensive to set up and operate and capable to produce clean surfaces at room temperature, either in a room atmosphere or in a controlled atmosphere

The second one, the CO_2 snow cleaning, consists in a high-velocity gas/particle stream of CO_2 snow. There are two primary mechanisms for CO_2 snow cleaning: particle removal by momentum transfer and organic removal by the solvent action of a transient liquid CO_2 phase. The particle removal is accomplished by the combined actions of momentum transfer and an aerodynamic drag force. A moving gas exerts an aerodynamic drag force on a particle, and this force is proportional to its cross-sectional area. Gas flow alone cannot generate sufficient forces to remove micrometer- and submicrometer-sized particles bound by physical means such as Van der Waals forces. In fact, the aerodynamic drag force at or near a surface is zero, the "dead zone" of no flow. CO_2 snow cleaning introduces mass, as dry ice particles, into the gas stream, and the snow strikes the particle. This is shown in Figure 3. This collision transfers momentum from the snow to the surface contaminant, thereby potentially overcoming the surface adhesive forces, liberating the surface particulate. Once liberated from the surface, the particle is easily carried away with the high velocity gas.The mechanism for organic removal involves the presence of liquid CO_2, an excellent solvent for non polar hydrocarbons. During the short impact time, stresses increase at the snow-surface interface, and the pressure can easily exceed the dry ice yield stress and triple point pressure. The dry ice particle liquefies and acts as a solvent while this is in contact with the surface, as shown in Figure 4. When the dry ice particle starts to rebound off the surface, the interfacial pressures decrease and the dry ice particle resolidifies, carrying the contamination away [14].

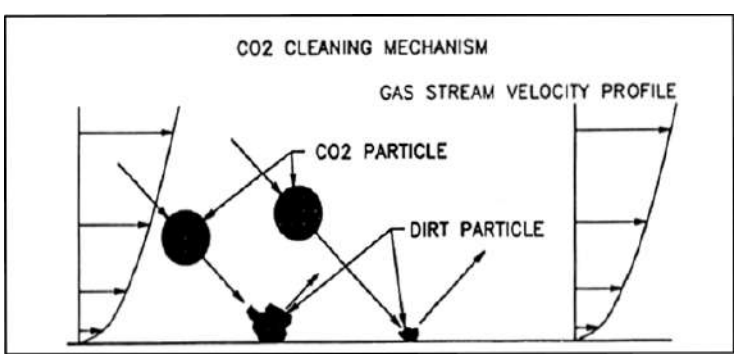

Figure 3: The mechanism of CO_2 snow of particle removal by momentum transfer [14]

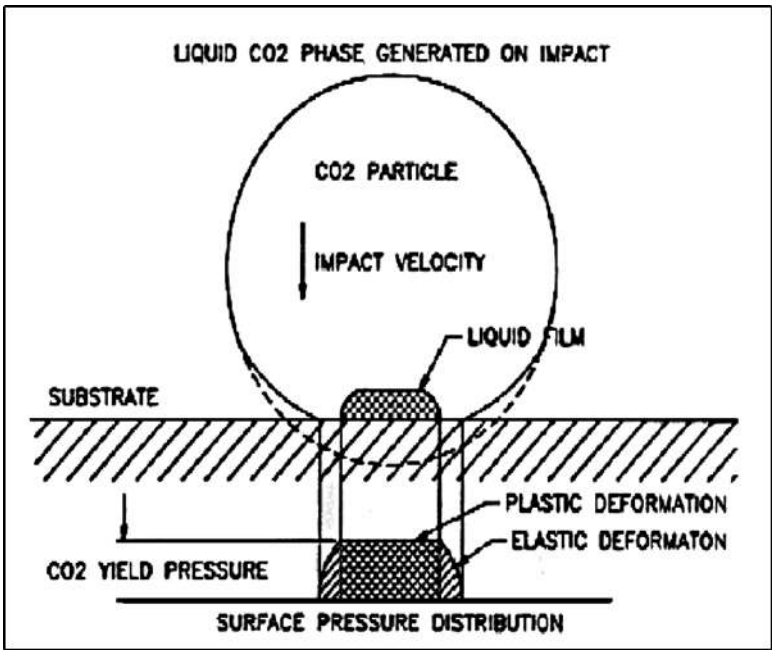

Figure 4: The mechanism of organic removal by the solvent action of a transient liquid CO_2 [14]

2.3 Spin coating

A typical spin coating process (see Figure 5), according to the Micro/Nano Technology Center of University of Louisville [15] consists of three steps: a dispense step in which the resin fluid is deposited onto the substrate surface, a high-speed spin step to thin the fluid, and a drying step to eliminate excess solvents from the resulting film.

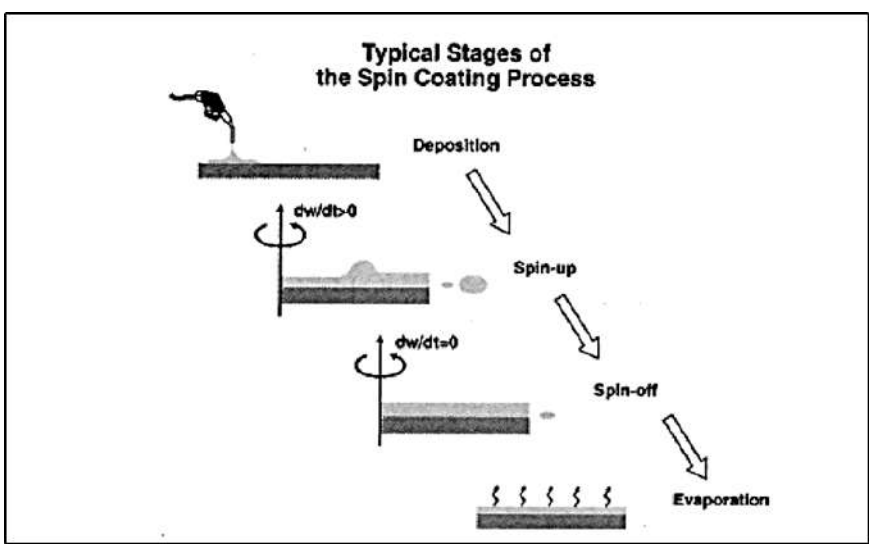

Figure 5: Stages of the spin coating process [16]

Dispense step:

Two common methods of dispense are Static dispense and Dynamic dispense.

- *Static dispense* is simply depositing a small puddle of fluid on or near the center of the substrate. This can range from 1 to 10 cm^3 depending on the viscosity of the fluid and the size of the substrate to be coated. Higher viscosity and/or larger substrates typically require a larger puddle to ensure full coverage of the substrate during the high-speed spin step.
- *Dynamic dispense* is the process of dispensing while the substrate is turning at low speed. A speed of about 500 RPM is commonly used during this step of the process. This serves to spread the fluid over the substrate and can result in less waste of resin material.

High-speed spin step:

After the dispense step it is common to accelerate to a relatively high speed to thin the fluid to near its final desired thickness. Typical spin speeds for PMMA coating in this step range from 1500-3000 RPM, again depending on the properties of the fluid as well as the substrate. This step can take from 10 seconds to two minutes. In general, higher spin speeds and longer spin times create thinner films. Relatively minor variations of ± 50 RPM at this stage can cause a resulting thickness change of 10%.

Drying step:

It is sometimes added after the high speed spin step to further dry the film without substantially thinning it. Under typical industrial conditions, the extra solvent of the PMMA layer is removed in an oven at a temperature of 60°C for 30 minutes after spin coating or also it could be dried in an Argon atmosphere for 1 hour at 60°C and then for another 1 hour at 120°C in order to remove residual solvents and to anneal the polymer films. This can be advantageous for thick films since long drying times may be necessary to increase the physical stability of the film. The drying rate of the resin fluid during the spin process is defined by the nature of the fluid itself (volatility of the solvent systems used) as well as by the air surrounding the substrate during the spin process.

Some authors found useful relations for the determination of the thickness h based on some parameters of the coating procedure (like ω = angular velocity spin, c = concentration of polymer in the solvent).

Walsh et al. [17; 18] obtained relations for the thickness h of the coated polymer PMMA under two different solvents:

$$h = 0.92 \cdot c^{1.56} \omega^{-0.51} \quad \text{Solvent: Toluene}$$

$$h = 4.3 \cdot c^{1.33} \omega^{-0.50} \quad \text{Solvent: Chloroform}$$

Mohajerani et al. [19] obtained the following equation for thickness h, but for another solvent:

$$h = 3.2 \cdot c^{1.66} \omega^{-0.53} \quad \text{Solvent: Dichloroethane}$$

Mohajerani et al. [19] observed that the striation form on the surface of the PMMA is often seen in solvents which have high evaporation rate. Also, they noted that increasing the concentration of solution will rapidly decrease the uniformity of the layer. Therefore, lower concentrations are highly recommended.

Tippo et al. [20] also obtained results for other solvents, and also Toluene:

$$h = 951.79 \cdot e^{0.445c}\omega^{-0.453} \quad \text{Solvent: DMF (dimethylformamide)}$$

$$h = 1586.26 \cdot e^{0.375c}\omega^{-0.430} \quad \text{Solvent: nBA (n-butylacetate)}$$

$$h = 1502.12 \cdot e^{0.370c}\omega^{-0.410} \quad \text{Solvent: Toluene}$$

Tippo et al. [20] observed that uniform and pinhole-free PMMA films were obtained using DMF and nBA. Also, among all spin speeds experimented, 2000 RPM was found to give the least thickness fluctuation.

2.4 Ion implantation

2.4.1 Ion Stopping

Energy-Loss Process

When an energetic ion penetrates a solid, it undergoes a series of collisions with the atoms and electrons in the target. According to Nastasi and Mayer [1], in these collisions the incident particle loses energy at a rate of dE/dx of a few to 100 eV/nm, depending on the energy, mass and atomic number of the ion as well as on the mass, atomic number and density of the substrate material. However, such lose energy rate can vary with many orders of magnitude if we used different ions, even using the same energy. As the incident ion penetrates the solid, undergoing collisions with atoms and electrons, the distance traveled between collisions and the amount of energy lost per collision are random processes. This energy-loss rate is determined by screened Coulomb interactions with the substrate atoms and electrons. It is customary to distinguish two different mechanisms of energy-loss (see Figure 6): (1) nuclear collisions, in which energy is transmitted as translatory motion to a target-atom as a whole, and (2) electronic collisions, in which the moving particle excites or ejects atomic electrons. Then, the energy-loss rate,dE/dx, can be expressed as:

$$\frac{dE}{dx} = \left.\frac{dE}{dx}\right|_n + \left.\frac{dE}{dx}\right|_e$$

where the subscripts n and e denote nuclear and electronic collisions, respectively.

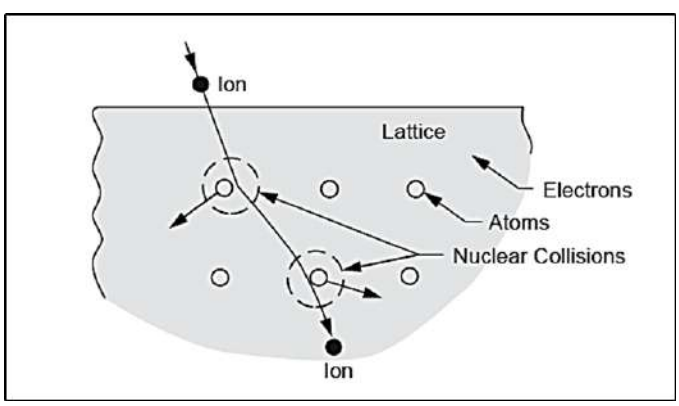

Figure 6: An incident ion on a lattice is deflected by nuclear collisions and also loses energy in electron collisions [1]

Nuclear Stopping

Nuclear stopping is concerned with the average energy-loss that results from elastic collisions with target-atoms. The nuclear stopping power or nuclear energy-loss rate is the energy lost by a moving particle due to elastic collisions per unit length traveled in the target. In order to derive an expression for the nuclear stopping, we need to derive an expression for the transferring of energy during a scattering event. To do so, one first develops the probability functions for scattering events. As depicted in Figure 7, a flux of energetic incident particles traverses a thin target of thickness Δx of and unit area, containing a total of N target atoms per unit volume. Each target nucleus presents an effective scattering area, σ, to this projectile.

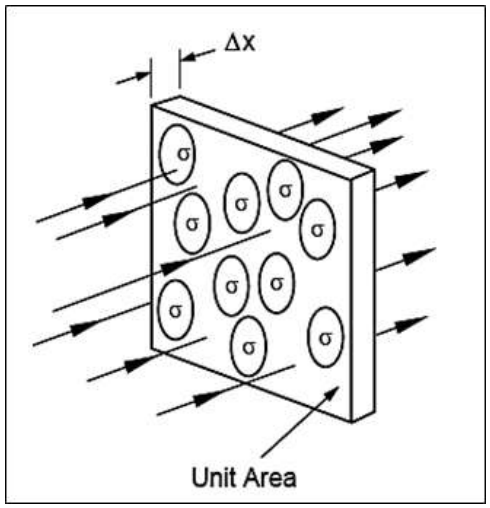

Figure 7: Schematic view of a portion of a scattering foil, with each target atom presenting an effective scattering area, σ [1]

The thin target in Figure 7 contains a total of $N\Delta x$ target nuclei per unit area. The product $(\sigma N \Delta x)$ represents the total fraction of the target surface area, which acts as an effective scattering center to the incident energetic particles. Then, we can define the probability of a projectile with energy E undergoing a scattering event or a collision with a target nucleus while traversing a thickness Δx as

$$P(E) = N\sigma(E)\Delta x.$$

This equation defines the total collision cross-section, $\sigma(E)$, between an energetic particle of energy E and the target atoms. The total cross-section gives a measure of the probability for any type of collision to occur where energy transfers are possible, for energies up to and including the maximum transfer energy value given by $T_M = 4M_1M_2E/(M_1 + M_2)^2$, where M_1 is the mass of the ion, M_2 is the mass of the target atom and E is the initial energy of the ion.

Now, let us consider the condition in which we wish to know the probability that a projectile with energy E will transfer an amount of energy between T and $T+$ dT to a target atom. Then, such a probability function defines the differential energy-transfer cross-section, d$\sigma(E)$/dT, and is obtained by differentiating $P(E)$:

$$P(E,T)\ dT \equiv \frac{dP(E)}{dT}\ dT = N\Delta x \frac{d\sigma(E)}{dT}\ dT$$

where $P(E,T)$ is the probability that an ion with energy E will undergo a collision producing an energy-transfer in the range T and $T+$ dT while traversing a distance Δx, and is simply defined as the ratio of the differential cross-section to the total energy-transfer cross-section. The average energy-loss by the moving particle in the distance dx is obtained by multiplying the last expression by the transfer energy T and integrating over all possible values of T.

$$\langle dE \rangle = \int T \, \frac{dP(E)}{dT} \, dT = N \int_{T_{min}}^{T_M} T \, \frac{d\sigma(E)}{dT} \, dT \, dx$$

For infinitesimal dx, omitting the averaging symbol on dE, we have:

$$\left.\frac{dE}{dx}\right|_n = N \int_{T_{min}}^{T_M} T \, \frac{d\sigma(E)}{dT} \, dT$$

where $\left.\frac{dE}{dx}\right|_n$ is the nuclear stopping power. The lower limit in the integration T_{min} is the minimum energy-transferred and need not be zero. One value used for T_{min} is the energy needed to displace an atom from its lattice site, approximately 20–30eV. The upper limit T_M is again the maximum energy transfer $T_M = 4M_1M_2E/(M_1+M_2)^2$.

Electronic Stopping

As it was said before, the energy-transferred by the ion to the target electrons is called electronic stopping. A comparison of the nuclear and electronic stopping cross-sections expressed in reduced notation is shown in Figure 8. Taking into account that the reduced energy ε (which physically gives a measure of how energetic the collision is and how close the ion gets to the nucleus of the target atom) is proportional to ion energy and that $\varepsilon^{\frac{1}{2}}$ is proportional to ion velocity.

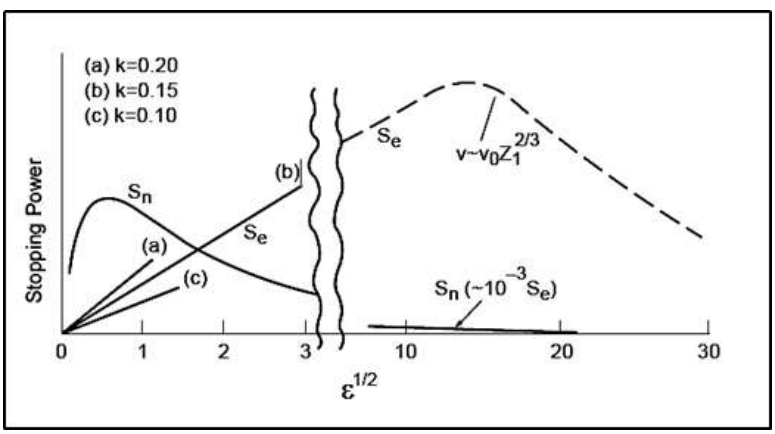

Figure 8: Reduced nuclear and electronic stopping cross-section as a function of $\varepsilon^{\frac{1}{2}}$ [1]

At higher velocities, the charge state of the ion increases and ultimately becomes fully stripped of all its electrons at $v \geqslant v_0 Z_1^{\frac{2}{3}}$. At this point, the ion can be viewed as a positive point charge Z_1,

moving with a velocity greater than the mean orbital velocity of the atomic electrons in the shells or subshells of the target atoms. When the projectile velocity v is much greater than that of an orbital electron (fast-collision case), the influence of the incident particle on an atom may be regarded as a sudden, small external perturbation. This picture leads to Bohr's theory of stopping power. The collision produces a sudden transfer of energy from the projectile to the target electron. The energy-loss from a fast particle to a stationary nucleus or electron can be calculated from scattering in a central force field. The stopping cross-section decreases with increasing velocity because the particle spends less time in the vicinity of the atom. In this high-energy, fast collision regime, the values of electronic stopping are proportional to $\frac{{Z_1}^2}{E}$ (where $v^2 \sim E$).

2.4.2 Ion range and Range Distribution

Ion Range concepts

To define some concepts about ion range, it is going to be useful starts with a two-dimensional schematic view (Figure 9) of an individual ion's path in the ion implantation process as it comes to rest in a material.

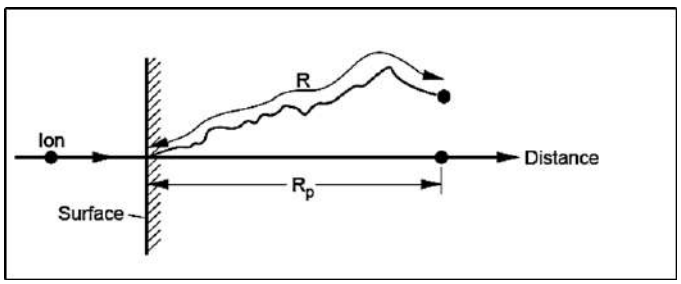

Figure 9: An incident ion on a surface with total path length R with a projected range R_p along the direction parallel to that of the incident ion [1]

As one can see, the ion does not travel to its resting place in a straight path due to collisions with target atoms The actual integrated distance traveled by the ion is called the *range*, R. The ion's net penetration into the material, measured along the vector of the ion's incident trajectory, which is perpendicular to the surface in this example, is called the *projected range*, R_p. A more general three-dimensional presentation of the penetration of a projectile into a solid is shown (Figure 10).

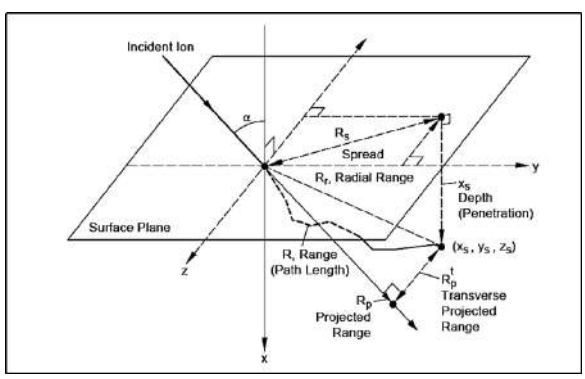

Figure 10: 3D schematic drawing of the penetration of a projectile into a solid [1]

In this schematic, an energetic projectile enters the sample surface at the point $(0, 0, 0)$, at an angle α to the surface normal. The projectile is stopped at the point (x_s, y_s, z_s). For this presentation of an ion's penetration into a solid, we define the range, R, and the projected range, R_p, consistent with the definitions used in Figure 7. However, since the incident ion is not parallel to the surface normal, the depth of penetration, x_s, which is defined as the perpendicular distance below the surface of which the projectile comes to rest, is not equal to the projected range. If $\alpha = 0$, these two quantities would be equal. The radial range, R_r, is the distance from the surface at the point of entrance, $(0, 0, 0)$, to the point where the projectile comes to rest, (x_s, y_s, z_s). The spreading range, R_s, is the distance between the point where the projectile enters the surface and the projection of the projectile's final resting place onto the surface plane. The transverse projected range, R_p^t, is the vector connecting the radial range and the projected range. For a single projectile coming to rest at the point (x_s, y_s, z_s), we have the following mathematical descriptions for the quantities defined in Figure 10:

1. the range spread

$$R_s = (y_s^2 + z_s^2)^{1/2}$$

2. the radial range

$$R_r = (x_s^2 + y_s^2 + z_s^2)^{1/2}$$

3. the transverse projected range

$$R_p^t = [(x_s sin\alpha - y_s cos\alpha)^2 + z_s^2]^{1/2}$$

4. the longitudinal projected range

$$R_p = [(R_r)^2 + (R_p^t)^2]^{1/2}$$

For normal-incidence projectiles, the range spreading is equal to the transverse projected range.

Range Distribution

Because the stopping of an ion is a stochastic (random) process, the collision sequence, the subsequent ion deflection and the ion's total path length in coming to rest vary randomly from ion to ion. As a result, ions with the same energy, with the same incident angle onto the sample surface and into the same material, do not necessarily come to rest in the same place. Hence, all ions of a given type and incident energy do not necessarily have the same range. Instead, if one was to examine the range history of many ions, a statistically broad distribution in the depths to which ions penetrate would be observed, similar to that shown in Figure 11. The distribution in projected ranges is referred to as the range distribution or range straggling, with the most probable projected range referred to as the average or mean projected range. A statistical distribution would also be observed for all the quantities defined in Figure 10.

The depth distribution *N(x)* of implanted ions, normalized for an ion implantation dose ϕ_i, is given by the expression:

$$N(x) = \frac{\phi_i}{\Delta R_p (2\pi)^{1/2}} \, exp\left[-\frac{1}{2}\left(\frac{x - R_p}{\Delta R_p}\right)^2 \right]$$

where R_p is the projected range (mean depth of the distribution) and ΔR_p is the projected range straggling (standard deviation of the distribution). Assuming that all implanted ions are retained, the dose is related to the ion depth distribution by

$$\phi_i = \int_{-\infty}^{\infty} N(x)dx$$

The expression for peak atomic density in the ion implantation distribution is obtained by setting $x = R_p$ in the expression of $N(x)$:

$$N(R_p) = N_p = \frac{\phi_i}{\Delta R_p (2\pi)^{1/2}} \cong \frac{0.4\phi_i}{\Delta R_p}$$

where N_p is in units of $\frac{atoms}{cm^3}$ and for ϕ_i in units of $\frac{atoms}{cm^2}$ and ΔR_p in centimeters.

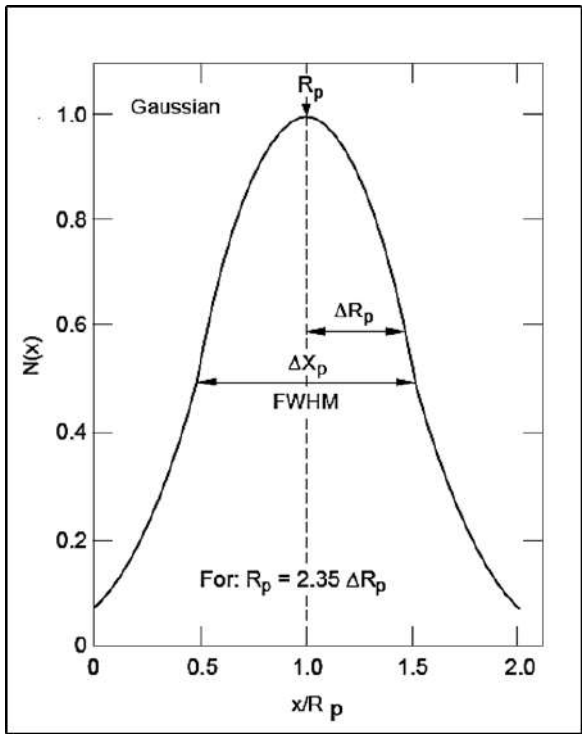

Figure 11: Gaussian range distribution for implanted ions with $R_p = 2.35\Delta R_p$ [1]

2.4.3 Displacement and Radiation Damage

According to Nastasi and Mayer [1], radiation damage theories are based on the assumption that a lattice atom struck by an energetic ion or recoiling target atom must receive a minimum amount of energy in the collision to be displaced from its lattice site. The energy required to displace the lattice atom represents the displacement threshold and is called the displacement energy, E_d. If in the collision process the energy transfer to the lattice atom, T, is less than E_d, the struck atom undergoes large amplitude vibrations without leaving its lattice position. The vibrational energy

of the struck atom is quickly shared with nearest neighbors and appears as a localized source of heat. However, if T is greater than E_d, the struck atom is able to move out of the potential well that represents its stable lattice site and move off into the lattice as a displaced atom. In the simplest case, the displaced atom leaves a vacancy and occupies an interstitial site in the lattice. This vacancy-interstitial defect is referred to as a *Frenkel pair* or *Frenkel defect*. A Frenkel defect is defined as a lattice vacancy created by removing an atom from its site and placing it at an interstitial position within the lattice. Thus a Frenkel pair is a vacancy and an interstitial.

The displacement energy, E_d, is the energy that a target atom has to receive in order to leave its lattice site and form a stable interstitial. This energy depends on the direction of the momentum of the target atom. Therefore, a range of displacement energies exists for the creation of a Frenkel pair. The threshold energy for atomic displacement can be determined experimentally by monitoring changes in the material's electrical resistivity using electron irradiation at liquid helium temperatures. Measurements are typically made on single crystal material as a function of both the electron's accelerating voltage and the orientation of the crystal with respect to the electron beam. Since the recoil direction of the struck atom is determined by the dynamics of the collision, it will be a random variable during real experiments. The directional dependence of E_d, coupled with the randomness of the initial directions of the struck atom, imply that the notion of a sharp displacement threshold is oversimplified. In reality, there is a range of displacement energies for which a displacement may occur. A weighted average over the displacement directions leads to an average displacement energy, which is the value most typically used as E_d.

Displacement due to a Primary Knock-on (PKA)

Displacement due to PKA examine the production of displaced atoms from a single PKA of energy E. As it is shown in Figure 12, a primary recoil atom is produced when an energetic incident particle (ion) undergoes a collision with a lattice atom.

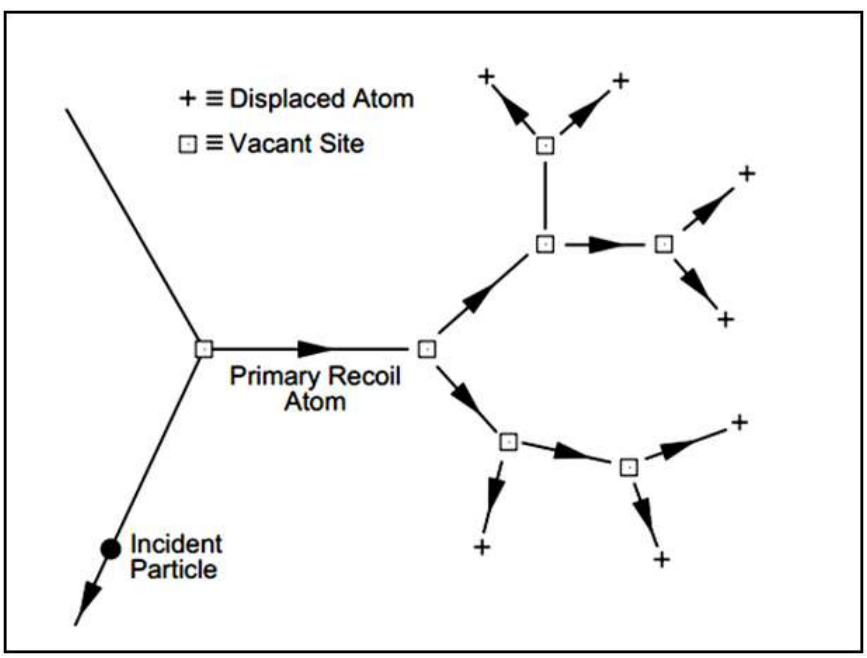

Figure 12: Schematic of the formation of the collision cascade by PKA [1]

If the energy transferred to the PKA is large enough, $E \ggg E_d$, the PKA can continue the knock-on atom processes, producing secondary recoil atom displacements, which in turn can displace additional atoms. Such an event will result in many collision and displacement events occurring in near proximity to each other. The multiple displacement sequence of collision events is commonly referred to as a *collision* or *displacement cascade*. The *average number* of displaced atoms in a cascade produced by a PKA of energy E will be denoted by $\langle N_d(E) \rangle$, also known as the *displacement damage function*.

The simplest calculation of the damage function, $\langle N_d(E) \rangle$, is based on the hard sphere model of Kinchin and Pease. The following assumptions are made in the Kinchin and Pease model:

1 Collisions are between like atoms, i.e., $M_1 = M_2$;

2 The probability of transferring energy during the collision process is determined by a hard sphere cross-section, i.e.;

$$P(E,T)\ dT \cong \frac{dT}{\gamma E} = \frac{dT}{E}$$

where $\gamma = 1$ for $M_1 = M_2$

3 The cascade is created by a sequence of two-body collisions;

4 All collisions are elastic, only consider nuclear processes, ignoring electronic stopping;

5 The energy consumed in displacing an atom, E_d, is neglected in the energy balance of the binary collision that transfers kinetic energy to the struck atom;

6 The arrangement of the atoms in the solid is random, and effects due to the crystal structure are neglected;

7 A lattice atom receiving less than a critical energy E_d is not displaced. Similarly, if a knock-on atom emerges from a collision with $E < E_d$, it does not contribute further to the cascade. Also, atoms receiving energy between E_d and $2E_d$ are displaced but cannot themselves further increase the total number of displacements

Now, from the assumptions 2, 4 and 7; the ***total modified Kinchin–Pease displacement damage function*** is given by:

$$\langle N_d(E) \rangle = \begin{cases} 0 & (for\ E < E_d) \\ 1 & (for\ E_d < E < \dfrac{2E_d}{\xi}) \\ \dfrac{\xi\ \nu(E)}{2E_d} & (for\ \dfrac{2E_d}{\xi} \leq E < \infty) \end{cases}$$

where $\xi < 1$ and depends on atomic interactions (i.e., the interaction potential), and $\nu(E)$ is the amount of PKA energy not lost to electronic excitation, commonly referred to as the *damage energy*. Both analytical theory and computer simulations suggest a value near $\xi = 0.8$.

Primary knock-on-Atom Damage Energy

A PKA loses energy in both electronic and nuclear collisions as it slows down and comes to rest in a crystal. Only the latter process creates lattice disorder around the ion track and is responsible for radiation-damage effects. Therefore, in considering the disorder created by a PKA, one must first determine the partition of energy between electronic and nuclear processes. A similar procedure was used in determining the range distribution of implanted atoms. The difference between range and disorder calculations is that, in the latter case, the energy partition of the displaced atoms must be considered as well. As in the case of ion-range distributions, the crystal structure can influence the amount of energy lost in nuclear collisions.

As a theoretical treatment for the distribution of energy between electronic and nuclear processes for both the primary and the secondary knocked-on particles, consider η as the sum total of the energy given to electrons, ν as the total energy ending up in atomic motion, and $\eta + \nu = E \equiv$ *the energy of the incoming particle.*

For example, in Figure 13, it is shown ν/E, the fraction of PKA energy deposited in the solid in the form of atomic collision, as a function of PKA energy for several monoatomic materials for the case $M_1 = M_2$.

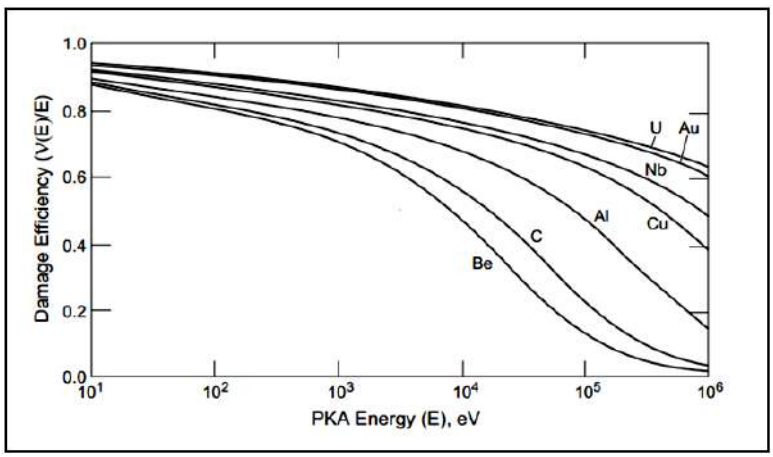

Figure 13: The fraction of the PKA energy deposited in atomic collisions as a function of PKA energy and self-ion type [1]

2.4.4 Stopping and Range of Ions in Matter (SRIM)

SRIM is a group of computer programs which calculate interaction of ions with matter. The programs were developed by James F. Ziegler and Jochen P. Biersack around 1983 and are being continuously upgraded with the major changes occurring approximately every five years. SRIM has a TRIM (Transport of ions in matter) as a group of programs, which calculates the stopping and range of ions into matter using a quantum mechanical treatment of ion-atom collisions. These calculations are made efficiently by the use of statistical algorithms based on Monte Carlo simulation method, namely the "binary collision approximation". According to Ziegler [21], what TRIM makes is follow a large number of individual ion or particle "histories" in a target. Each history begins with a given ion energy, position and direction. The particle is assumed to change direction as a result of binary nuclear collisions and move in straight free-flight-paths between collisions. The energy

is reduced as a result of nuclear (elastic) and electronic (inelastic) energy losses, and a history is terminated either when the energy drops below a pre-specified value or when the particle's position is outside the target. This method is applicable to a wide range of incident energies from approximately 0.1 keV to several MeV, depending on the masses involved. The nuclear and electronic stopping powers are assumed to be independent, so that particles lose energy in discrete amounts in nuclear collisions and lose energy continuously from electronic interactions.

For the evaluation of atom-atom scattering, TRIM uses an analytic formula called ***Magic Formula***, which was developed by J.P Biersack and collaborators and permits to increase computing speed by up to 50 times over other methods because it allowed for the first time a quick solution to the scattering problem with high precision, instead of having to do the complete evaluation of the scattering integral. This Magic Formula is given by:

$$cos(\frac{\Theta}{2}) = \frac{B + R_c + \Delta}{R_0 + R_C}$$

where Θ is the scattering angle, $B \equiv p/a$, $R_0 \equiv r_0/a$, $R_C \equiv \rho/a$, $\Delta \equiv \delta/a$, p is the impact parameter, r_0 is the distance of closest approach, $\rho \equiv \rho_1 + \rho_2$, $\delta \equiv \delta_1 + \delta_2$, ρ_1 and ρ_2 are radii of curvature of the trajectories at closest approach, δ_1 and δ_2 are small corrections terms, $a = 0.8853\ a_0/(Z_1^{2/3} + Z_2^{2/3})$, a_0 is the Bohr radius and Z_1, Z_2 are the incident particle and target atomic numbers, respectively.

In the TRIM program, the energy transferred to a target atom is analyzed further to yield such results as (i) ionization by recoiling atoms in a cascade, (ii) damage energy and number of vacancies produced in a collision cascade, and (iii) damage energy and number of sub-threshold collisions in the cascade which transfer energies less than E_d (displacement energy), where knock-on atoms cannot permanently escape their lattice site and their energy ends up in lattice vibrations (phonons). For a quick calculation of the target damage, TRIM uses the theory proposed by Kinchin and Pease. From this theory, the *defect producing energy*, E_ν, is obtained from the *transferred energy*, T, of the recoil by taking into account electronic losses:

$$E_\nu = \frac{T}{1 + k_d\ g(\varepsilon_d)}$$

where the electronic losses are governed by:

$$k_d = 0.1334\ Z_2^{2/3} M_2^{-1/2}$$

and

$$g(\varepsilon_d) = \varepsilon_d + 0.40244\ \varepsilon_d^{3/4} + 3.4008\ \varepsilon_d^{1/6}$$

where

$$\varepsilon_d = 0.01014\ Z_2^{7/3} T$$

From the transferred energy, the number of displacements is calculated by the well known "modified Kinchin-Pease model":

$$\nu = 1,\ if:\ E_D < E < 2.5E_D$$

and

$$\nu = \frac{0.8E_\nu}{2E_D},\ if:\ E_\nu > 2.5E_D$$

where E_D is the displacement energy, Z_2 the atomic number of the target atom and M_2 the mass of the target atom. Thus, the number of vacancies per depth interval are calculated and provided as standard output of the TRIM program.

2.4.5 100 keV Ion Implanter

According to Fink [9], in principle, one can produce pure beams of any ion at any energy with an ion implanter. In this research, the 100 keV ion implanter of the Universität Leipzig was used (see Figure 14), whose *High Voltage* (HV) is $U_{HV} = 100\ kV$.

Figure 14: 100 keV ion implanter of the Universität Leipzig

According to the description given by Küpper [22], in order to generate negatively charged ions, a so-called SNICS II source (Source of Negative Ions by Cesium sputtering) is used. A schematic representation of the functional principle is shown in Figure 15. In this Figure 15, there is a container (sky brown) with Cesium, which is heated to about 140°C and thus vaporizes the Cesium. The steam passes through a small tube in the enclosed area of the Ionizer (crimson) and cathode (orange). The cathode is essentially a small hollow Copper cylinder, in which the material to be sputtered or implanted is pressed. Part of the Cesium vapour condenses on the surface of the cooled cathode, another part (gray) hits the ionizer and is ionized. At the position of cathode (Ca), a negative potential U_{Ca} is applied which accelerates the positively charged Cesium ions and focuses (black) towards the cathode. When the positively charged Cesium ions hit the cathode, two types of particles can now be produced by the sputtering process. On the one hand, depending on the cathode material, directly negatively charged ions are generated. On the other hand, neutral particles or positively charged ions can be generated during sputtering. However, as the positively charged ions pass through the thin layer of condensed Cesium vapour, they absorb electrons on the surface of the cathode and thus receive their negative charge. Then, by applying a positive potential U_{Ex} to the extractor (Ex), the negatively charged particles (sky blue) are extracted from the area of the source and fed to the actual acceleration and further beam guidance. This extractor also adjusts the beam to the remainder of the accelerator assembly, as it is a variable lens for ions due to the applied voltage.

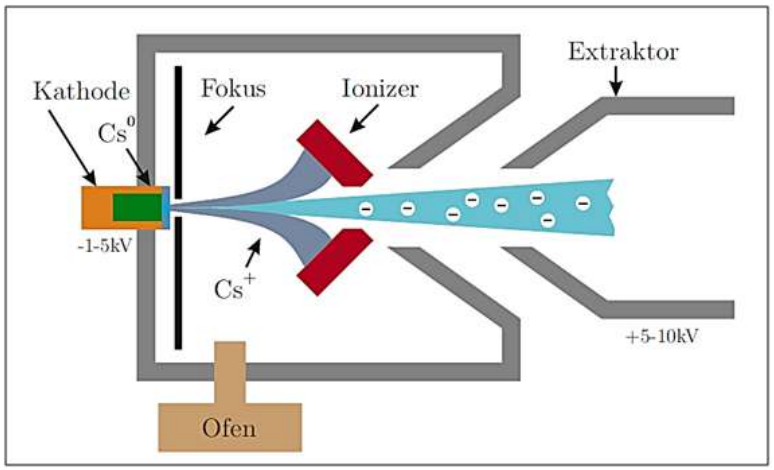

Figure 15: Schematic structure of the Cs (Cesium) source. Cs vapour exiting the oven (sky brown) is ionized at the ionizer (crimson) and accelerated toward the cathode (orange), where it ablates the cathode material. A thin layer of Cs on the cathode surface serves as a stripping medium, so that the beam of negatively charged ions (sky blue) thus generated by the extractor can leave the source with an energy of a few keV [22]

When the negatively charged ions leave the source, these follow the path described by the ion beam (sky blue) in the Figure 16.

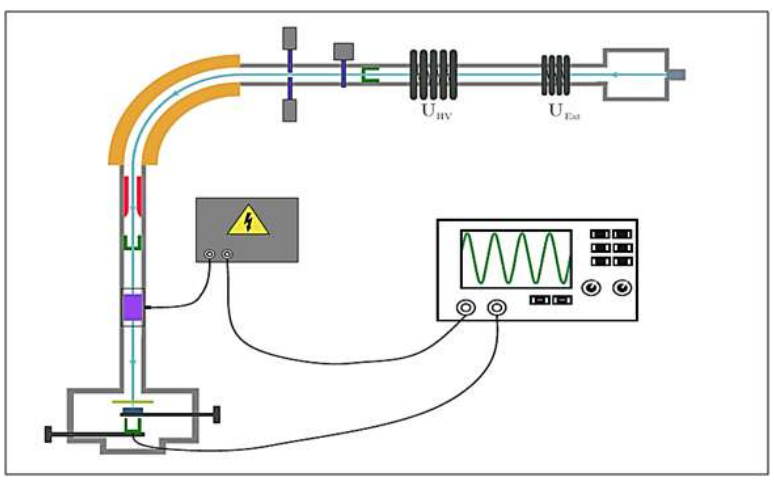

Figure 16: Schematic structure of the 100 keV ion implanter of the Universität Leipzig. The source is marked with the cesium reservoir (gray), the ion beam (sky blue), the 90° magnet for mass separation (orange), the focusing lens (red) followed by blanker (purple) and the sample chamber with position of the sample (dark gray), the mask holder (sky green) and the Faraday cup (dark green). If the particle beam is to be scanned over the sample by a mask, the appropriate settings can be found on the blanker by means of a connected oscilloscope on the Faraday cup in the sample chamber. [22]

These ions have a kinetic energy of 5-10 keV. Subsequently, the particles are accelerated to their desired energy by the accelerating section, which is an arrangement of 5 ring electrodes. The high voltage at the electrodes can be set to a maximum of $U_{HV} = 100\ kV$. Upon leaving this section, the particles have an energy of $E = q \cdot U_{total}$, where the total voltage is $U_{total} = U_{Ca} + U_{Ex} + U_{HV}$. Since the cathode material usually contains not only the desired element but also element compounds or impurities, a 90° - magnet (orange) joins the acceleration section. By exploiting the Lorentz force, this serves as a mass separator for the ions. With a maximum current of $I_{max} = 153\ A$, this generates a magnetic flux density of $B_{max} = 1.05$ T. Assuming that the magnet below I_{max} has no saturation effects, the dependency of the ion mass on the electric current I_{mag} can be determined by:

$$m(I_{mag}) = \frac{I_{mag}^2}{U_{total}} \cdot \frac{qR^2 B_{max}^2}{2I_{max}^2}$$

Since the radius of the circular path $R = 0.5\ m$ is given by the magnet, only those ions which satisfy the equation given above can leave the magnet. For negative ions, the charge q should be $-e$, which has as a consequence that the equation above has to have a minus sign in front of this due to the direction of the magnetic field B. Immediately behind the magnet is a Einzel-lens (red), which makes it possible to refocus and collimate the ion beam by changing the voltage applied to it. In front of the sample chamber is also the scanning unit. This consists of eight axially symmetrically arranged hollow cylinder sections (purple). By applying different voltages to the individual sections, it is possible to deflect the ion beam, as well as to scrape it over the sample. The sample (dark gray) is attached to a positioning stage in the sample chamber via a sample carrier. This allows to position the sample in all directions. A special feature of the sample chamber is a movable mask holder (sky green) directly in front of the sample holder. With it, different masks (made of Muscovite plates of 10-50 μm thickness, which are transparent) can be used in a position close and in front of the sample. Furthermore, Faraday cups (dark green) for measuring the ionic currents are located at three important points of the accelerator setup. The first cup is located behind the acceleration section and it measures the total current produced by the source or by the cathode. Another cup behind the magnet is used to record mass spectra. In order to be able to measure the ion current as close as possible to the sample, the third Faraday cup is located in the sample chamber. As a result, the actual current of the ion to be implanted can be determined with this last cup. Also, a microscope connected to a video camera is coupled to the sample chamber in order to have real-time images during the implantation.

2.5 Measurement equipments on surfaces

2.5.1 Atomic Force Microscopy (AFM)

This subsection is based on the Manual of Advanced Physics Laboratory of Universität Leipzig [23]. The AFM is one of a family of scanning probe microscopes which has grown steadily since the invention of the scanning tunneling microscope by Binning and Rohrer in the early eighties. This completely new microscopy technique works without focusing elements and features atomic resolution (laterally and vertically).

A small sharp probing tip is scanned very closely across the sample's surface, so close that the atomic forces between tip and sample are sensed. The microfabricated cantilever with an integrated tip is fixed onto a platform which can be moved in all three dimensions. Adjustment of the microscope requires in this case coarse and fine approaches of fiber end and cantilever on the one hand and of cantilever and sample on the other hand. This task is solved by a combination

of different piezoelectric actuators involving two concentric piezo tubes for fiber and cantilever positioning, a motor driven by shear piezos for positioning of the probe with respect to the sample and an arrangement of three piezo tubes for scanning. Piezoelectric ceramics are a class of materials that expand or contract in the presence of a voltage gradient or, conversely, create a voltage gradient when forced to expand or contract. Piezoceramics make it possible to create three-dimensional positioning devices of high precision.

AFM can generally measure the vertical and horizontal deflection of the cantilever with picometer resolution. To achieve this, most AFMs today use the optical lever. The optical lever operates by reflecting a laser beam off the back of the cantilever (see Figure 17). Angular deflection of the cantilever causes a twofold larger angular deflection of the laser beam. The reflected laser beam strikes a position-sensitive photodetector consisting of four side-by-side photodiodes. The difference between the four photodiode signals indicates the position of the laser spot on the detector and thus the angular deflection of the cantilever. If the tip is scanned over the sample surface then the deflection of the cantilever can be recorded as an image which represents the three dimensional shape of the sample surface.

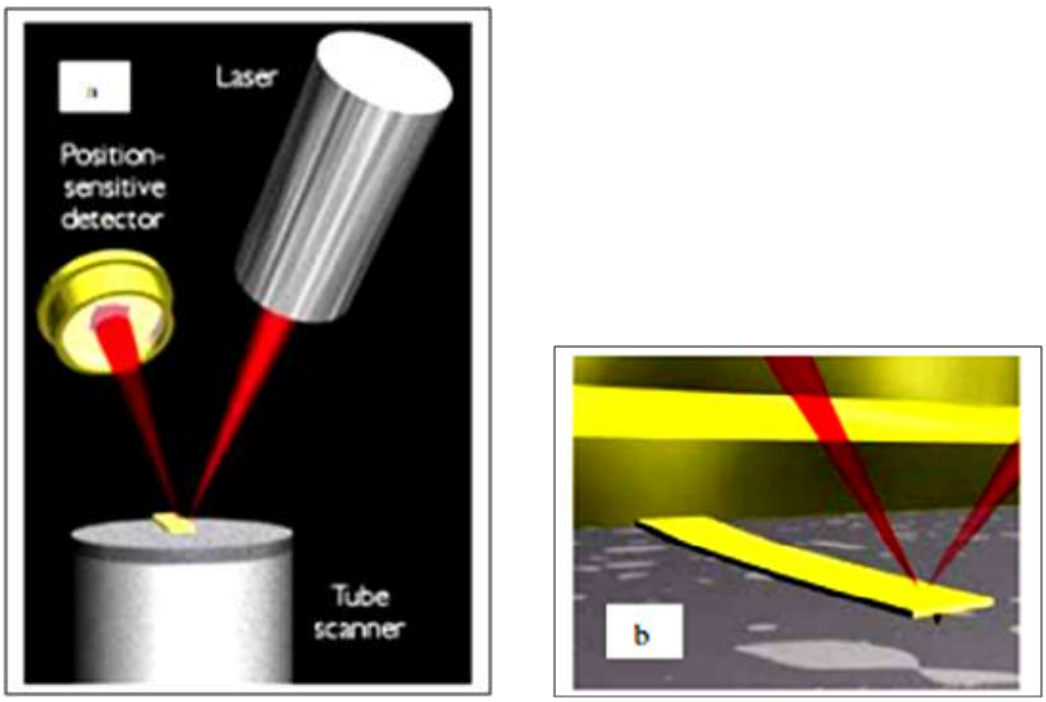

(a) (b)

Figure 17: The laser spot is focussed on the back of the cantilever and the angle of the reflected laser is detected by a PSD (photosensitive detector) [23]

In order to detect local forces or closely related physical quantities, the sharp probe scanning the sample surface at same distance has to be linked to some sort of force sensor. A convenient way to precisely measure forces is to convert them into deflections of a spring according to Hooke´s Law:

$$\Delta z = \frac{\Delta F}{k_c} \,,$$

where the deflection Δz is determinated by the acting force ΔF and the spring constant k_c.

Scan Modes

According to Hooke´s law, the cantilever which is raster-scanned across the sample surface exhibits a locally varying deflection which directly represents the corrugation of the sample surface. The distance regimes are the following (see Figure 18):

- The contact regime, and
- the non-contact regime.

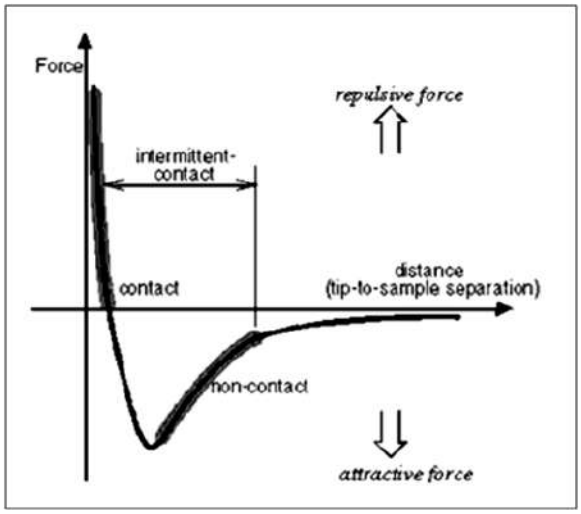

Figure 18: The parts of an approach-retraction cycle of the tip [23]. The closer the tip (contact mode) is to the surface, a repulsive force will act with greater intensity; the farther away from the surface the tip (non-contact mode) is found, an attractive force will act, decreasing at increasing distances.

Contact Mode

In this mode, the AFM tip makes soft physical contact with the surface. As the scanner gently traces the tip across the sample, the contact force causes the cantilever to bend to accommodate changes in topography.

At the right side of the curve of the Figure 18, the atoms are separated by a large distance. As the atoms are gradually brought together, they first weakly attract each other. This attraction increases until the atoms are so close together that their electron clouds begin to repulse each other electrostatically. This electrostatic repulsion progressively weakens the attractive force as the interatomic separation continues to decrease. The force goes to zero when the distance between the atoms reaches a couple of angstroms, about the length of a chemical bound. When the total Van der Waals force becomes positive (repulsive), the atoms are in contact. The slope of the Van der Waals curve is very steep in the repulsive or contact regime. As a result,the repulsive Van der Waals force balances almost any force that attempts to push the atoms closer together. In AFM this means that when the cantilever pushes the tip against the sample, the cantilever bends rather than forcing the tip atoms closer to the sample atoms.

Once the AFM has detected the cantilever deflection, it can generate the topographic data set by operating in one of two modes (see Figure 19):

- The constant-height mode, and
- the constant-force mode.

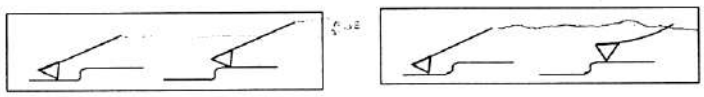

Figure 19: The difference between the two modes: In constant-force mode the cantilever deflection is constant (left) whereas in constant-height mode the z-value is the constant held parameter (right) [23]

In constant-force mode, the deflection of the cantilever can be used as input to a feedback circuit that moves the scanner up and down in z-axis, responding to the topography by keeping the cantilever deflection constant. Instead, in constant-height mode the cantilever deflections and thus variations in applied force are small, and for that reason is often used for taking atomic-scale images of atomically flat surfaces. Constant-height mode is essential for recording real-time images of changing surfaces, where high scan speed is essential.

Non-contact Mode

When lifting the probe by at least one nanometer from the sample surface, only long-range interactions remain. The relevant forces result in general from Van der Waals interactions, electro- and magnetostatic interactions.

Today, non-contact force microscopy usually involves a sinusoidal excitation of the cantilever with a frequency close to its main resonant frequency (see Figure 20). If magnetic interactions are involved, it is possible to externally modulate the oscillation (if the cantilever is coated ferromagnetically). The non-contact mode of operation involving an oscillating cantilever is frequently also called AC mode (or dynamic mode).

In contrast to the detection of a quasistatic force the response of the cantilever in the dynamic mode is more complex. If the cantilever is excited sinusoidally at its clamped end with a frequency ω and an amplitude δ_0, the probing tip likewise oscillates sinusoidally with a certain amplitude δ exhibiting a certain phase shift α with respect to the driving signal. The deflection sensor monitors the motion of the probing tip.

The equation of motion, the solution of which is monitored by the deflection sensor, is given by:

$$\frac{\partial^2 d}{\partial t^2} \; + \; \frac{\omega_0}{Q}\frac{\partial d}{\partial t} \; + \; \omega_0^2(d - d_0) = \delta_0 \; \omega_0 \; cos(\omega t) \; ,$$

where d_0 is the probe-sample distance at zero oscillation amplitude and d the momentum probe sample separation. Q is a constant which describes the intrinsic properties of the cantilever. The steady-state solution is:

$$d(t) = d_0 \; + \; \delta \; cos(\omega t \; + \; \alpha)$$

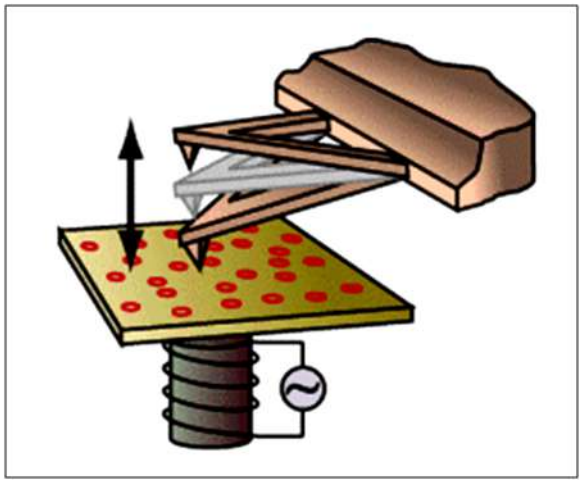

Figure 20: An externally induced periodically changing magnetic field moves the ferromagnetic coated cantilever [23]

This simplified formalism is based on the assumption that the oscillation amplitude δ is sufficiently small in comparison with the length of the cantilevers. All these results describe only free cantilever oscillations. This means, d_0 is still so large that no influence of the sample on the probe´s oscillation can be detected. If d_0 is now decreased such that a force F affects the motion of the cantilever, then a term F/m has to be added. In order to consider almost all interactions which could be interesting in force microscopy, one has to assume:

$$F = F\left(d,\ \frac{\partial d}{\partial t}\right).$$

Since F describes in the various types, i. e. of very different dependence on the probe-sample spacing, the d(t) curves monitored by the deflection sensor usually represent enharmonic oscillations. If $F(d)$ can be substituted by a first-order Taylor approximation for $\delta_0 \ll d_0$, then the force microscope detects the compliance or vertical component of the force gradient $\partial F \ / \ \partial z$. On the basis of this approximation the cantilever behaves under the influence of the probe-sample interaction as if it would have the modified spring constant:

$$c_F = k_c \ - \ \frac{\partial F}{\partial z} \ ,$$

where k_c is the intrinsic spring constant. The change of the apparent spring constant will modify the cantilever´s resonant frequency to:

$$\omega \ = \ \omega_0 \sqrt{1 \ - \ \frac{1}{k_c}\frac{\partial F}{\partial z}}.$$

The most commonly used detection method which is generally referred to as *slope detection* involves driving the cantilever at a fixed frequency ω slightly to resonance. A change in $\frac{\partial F}{\partial z}$ gives rise to a shift in the resonant frequency $\Delta\delta$ in the amplitude of the cantilever vibration. $\Delta\delta$ is obviously a maximum at that point of the amplitude-versus-frequency curve where the slope is a maximum.

In addition, cantilevers used for non-contact AFM must be stiffer than those used for contact AFM because soft cantilevers can be pulled into contact with the sample surface. The small force values in the non-contact AFM and the greater stiffness of the cantilevers used for non-contact AFM are both factors that make the non-contact AFM signal small, and therefore difficult to measure.

2.5.2 DektakXT Stylus Profiler

DektakXT stylus surface profiler by BRUKER [24] (see Figure 21) is an advanced thin and thick film step height measurement tool. In addition to taking two-dimensional surface profile measurements, the DektakXT system can produce three-dimensional measurements and analyses when equipped with the 3D Mapping Option.

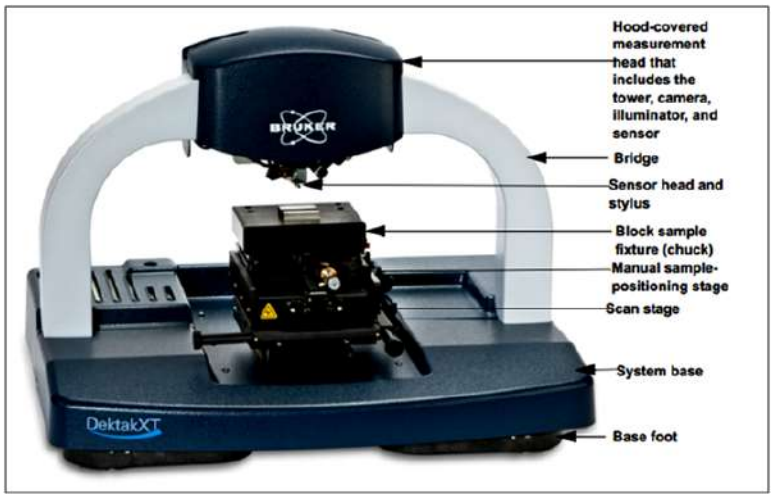

Figure 21: DektakXT Stylus Profiler with the Standard Manual X-Y Sample-Positioning Stage [24]

According to Stout [25], almost all stylus instruments are based around the microcomputer, the measurement system comprises two parts - the traditional stylus instrument responsible for the measurement, amplification and output of the signal, and the microcomputer responsible for motion control of the measurement procedures, processing of data, characterization of the surface and display of the necessary results, including parameters and graphics. These two parts are connected by either a parallel or serial interface, and by an analogue-to-digital (A/D) board which is used by the microcomputer for digitizing data from the analogue signal. Specifically, the DektakXT system takes measurements electromechanically by moving a diamond-tipped stylus over the sample surface according to a user-programmed scan length, speed, and stylus force. The stylus is linked to a Linear Variable Differential Transformer (LDVT), which produces and processes electrical signals that correspond to surface variations of the sample. After being converted to digital format, these surface variations are stored for display and analysis (see Figure 22).

Vision64 measurement and analysis software (see Figure 23) has 64-bit parallel processing architecture. It allows one to adjust the system illumination, position a sample under the stylus, take single-scan or automated measurements, calculate analytical functions, apply analyses and filters, and perform special operations, such as comparing the analytical results from multiple scans.

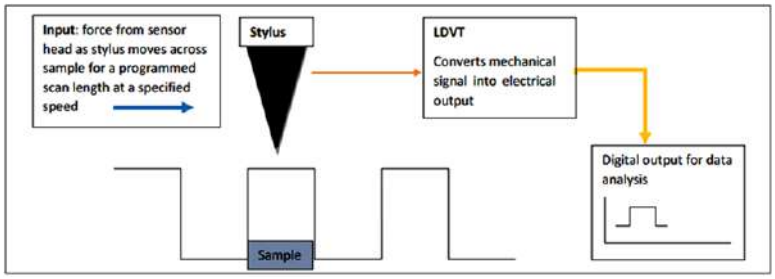

Figure 22: An overview of the profilometer measurement mechanism during data acquisition [26]

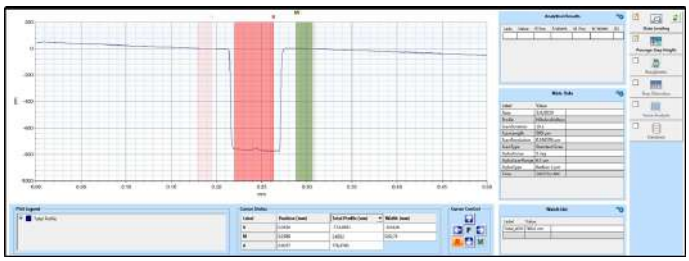

Figure 23: Window displayed by Vision64 after the scan of one sample

2.6 Optical Properties

2.6.1 Refraction Index of Materials

This subsection is based on the script of the course Advanced Materials B.1 by Prof. Dr. Helmut Föll of the University of Kiel [27]. As it is known, light is an electromagnetic wave, which means that there is an electrical field that oscillates with some frequency. When it impinges on a dielectric material (= no free electrons), it will jiggle the charges inside (bound electrons) around a bit. This electrical field causes some *polarization* of the dielectric material, which leads straight to the *dielectric constant* ϵ_r. The dielectric constant is linked to the *index of refraction* **n** by: $n = \epsilon_r^{1/2}$. For oscillating electrical fields we needed to look at the frequency dependence of the polarization and that lead straight to the complex dielectric function $\epsilon_r(\omega) = \epsilon^{'}(\omega) + i\epsilon^{''}(\omega)$, instead of the simple dielectric constant ϵ_r. A complex dielectric function leads to a *complex index of refraction* n^* defined as:

$$n^* = n + i\kappa$$

This new concept of *complex index of refraction* is useful to describe the optical properties of the materials, as it will be seen later. Using the old relation between the index of refraction and the dielectric constant but now write it as:

$$(n + i\kappa)^2 = \epsilon^{'} + i\epsilon^{''}$$

with $n = n(\omega)$; $\kappa = \kappa(\omega)$, since $\epsilon^{'}$ and $\epsilon^{''}$ are frequency dependent. Rearranging for n and κ yields to the following equations:

$$n^2 = \frac{1}{2}((\epsilon^{'2} + \epsilon^{''2})^{1/2} + \epsilon^{'})$$

$$\boldsymbol{\kappa^2 = \frac{1}{2}((\epsilon'^2 + \epsilon''^2)^{1/2} - \epsilon')}$$

In order to understand the meaning of $\boldsymbol{n}$ and $\boldsymbol{\kappa}$, first we have to remember that $\boldsymbol{\epsilon''}$ is connected to the "dielectric" and static (ohmic) conductivity of the material and express $\boldsymbol{\epsilon''}$ in terms of the (total) conductivity $\boldsymbol{\sigma_{DK}}$ as:

$$\boldsymbol{\epsilon''} = \frac{\sigma_{DK}}{\epsilon_0 \cdot \omega};$$

using that in the expression $\boldsymbol{(n + i\kappa)^2}$ gives:

$$\boldsymbol{(n + i\kappa)^2 = n^2 - \kappa^2 + i \cdot 2n\kappa = \epsilon' + i \cdot \frac{\sigma_{DK}}{\epsilon_0 \cdot \omega}}$$

As we have a complex number on both sides of the equality sign, this demands that the real and imaginary parts must be the same on both sides, so that:

$$\boldsymbol{n^2 - \kappa^2 = \epsilon'}$$

$$\boldsymbol{n\kappa = \frac{\sigma_{DK}}{2\epsilon_0 \omega}};$$

separating $\boldsymbol{n}$ and $\boldsymbol{\kappa}$ finally gives:

$$\boldsymbol{n^2 = \frac{1}{2}((\epsilon'^2 + \frac{\sigma_{DK}^2}{4\epsilon_0^2\omega^2})^{1/2} + \epsilon')}$$

$$\boldsymbol{\kappa^2 = \frac{1}{2}((\epsilon'^2 + \frac{\sigma_{DK}^2}{4\epsilon_0^2\omega^2})^{1/2} - \epsilon')}$$

Now, to find the physical meaning of $\boldsymbol{n}$ and $\boldsymbol{\kappa}$, i.e. the real and complex part of the complex index of refraction, we have to look at an electromagnetic wave travelling through a medium with such an index. For that end, we can simply use the general formula for the electrical field strength $\boldsymbol{E}$ of an electromagnetic wave travelling in a medium with refractive index $\boldsymbol{n^*}$. To simplify the process, we can do it just in the x-direction. Then, $\boldsymbol{E_x}$ is given by the expression:

$$\boldsymbol{E_x = E_{0,x} \cdot exp\{i\,(k_x x - \omega t)\}}$$

with $\boldsymbol{k_x}$= component of the wave vector in x-direction, which is equal to $2\pi/\lambda$ and $\omega = 2\pi\nu$.

In order to get the index of refraction in this expression of the electric field strength, one has to introduce the velocity $\boldsymbol{v}$ of the electromagnetic wave in the material and use the relation between frequency, wavelength, and velocity to get rid of $\boldsymbol{k}$ or $\boldsymbol{\lambda}$, respectively. For this end, we have to use:

$$\boldsymbol{v = \frac{c}{n^*}}$$

$$\boldsymbol{v = \nu \cdot \lambda}$$

$$\boldsymbol{k = \frac{2\pi}{\lambda} = \frac{\omega \cdot n^*}{c}}$$

where $\mathbf{c}$ is the speed of light in vacuum. Then we get:

$$\boldsymbol{E_x = E_{0,x} \cdot exp(\frac{i\,\omega n\,x}{c} - \frac{\omega\kappa x}{c} - i\omega t)},$$

where red expression is nothing but the wavevector, so we get the result:

$$\boldsymbol{E_x = exp(-\frac{\omega\kappa x}{c}) \cdot exp(i \cdot (k_x x - \omega t))}$$

The first exponential represents the decreasing amplitude, and the second exponential the plane wave. So, if we use a complex index of refraction, the propagation of electromagnetic waves in a material is whatever it would be for an ideal material with only a real index of refraction times a *attenuation factor* that decreases the amplitude exponentially as a function of depth x.

The imaginary part $\boldsymbol{\kappa}$ of the complex index of refraction thus describes rather directly the attenuation of electromagnetic waves in the material considered. It is known as **damping constant**, **attenuation index**, **extinction coefficient** or **absorption constant**, where $\boldsymbol{\kappa}$ is not constant, but depends on the frequency.

2.6.2 Interference in thin films

This phenomena occurs when light waves are reflected from the front and back surfaces of such thin films, and constructive interference between the two reflected waves (with different path lengths) occurs in different places for different wavelengths. The Figure 24 shows the situation. The light shining on the upper surface of a thin film with thickness t is partly reflected at the upper surface (path abc). Light *transmitted* through the upper surface is partly reflected at the lower surface (path $abdef$). Depending on the phase relationship, they may interfere constructively or destructively. Different colors have different wavelengths, so the interference may be constructive for some colors and destructive for others [28].

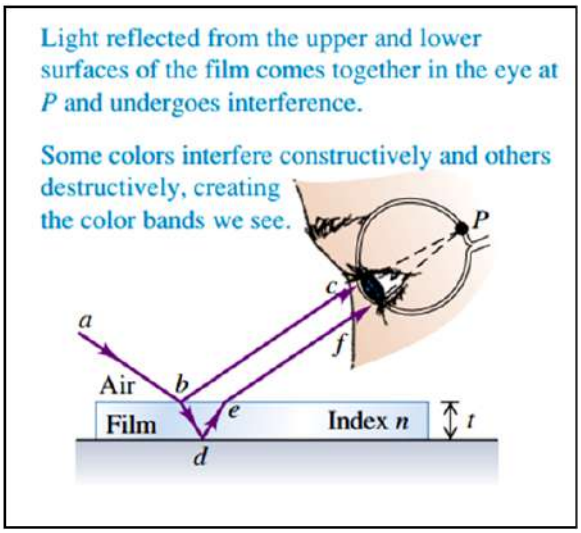

Figure 24: Interference between rays reflected from the two surfaces of a thin film [28]

To analyze the thin-film interference and phase shifts during the reflections, let´s look at a simplified situation in which *monochromatic* light reflects from two nearly parallel surfaces at nearly normal incidence. Then, following the sketch shown in the Figure 25 proposed by Young and Freedman [28], it is going to consider just the interference between the two light waves reflected from the surfaces adjacent to the air wedge. The path difference between the two waves is just twice the thickness t of the air wedge at each point. So, at points where $2t$ is an integer number of wavelengths, we expect to see constructive interference and a bright area; where it is a half-integer number of wavelengths, we expect to see destructive interference and a dark area.

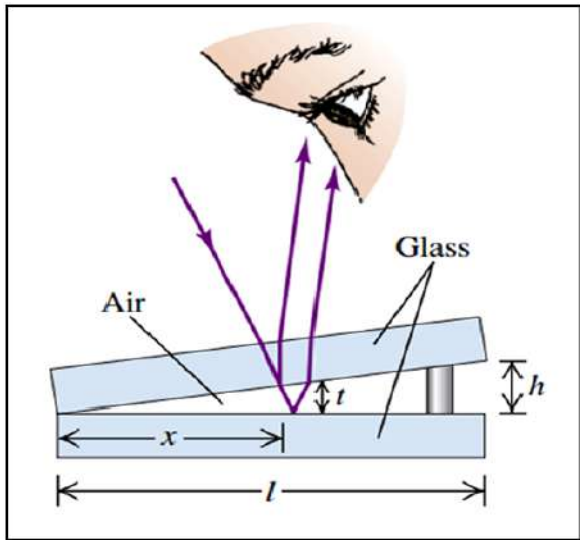

Figure 25: Interference between light waves reflected from the two sides of an air wedge [28]

But, experimentally, the results are interchanged. This suggests that one or the other of the reflected waves has undergone a half-cycle phase shift during its reflection. In fact, this phase shift can be predicted from Maxwell's equations and the electromagnetic nature of light.

This phase shift is explained by Griffiths in his book *Introduction to Electrodynamics* [29]. Suppose a light wave with electric-field amplitude E_i is traveling in an optical material with index of refraction n_a. It strikes, at normal incidence, an interface with another optical material with index n_b. The amplitude E_r of the wave reflected from the interface is proportional to the amplitude E_i of the incident wave and is given by:

$$E_r = \frac{n_a - n_b}{n_a + n_b} E_i$$

This result shows that the incident and reflected amplitudes have the same sign when n_a is larger than n_b and opposite sign when n_b is larger than n_a. Finally, one can summarize that if the film has thickness t, the light is at normal incidence and has wavelength λ in the film; if neither or both of the reflected waves from the two surfaces have a half-cycle reflection phase shift, the conditions for constructive and destructive interference are (for $m = 0, 1, 2, \ldots$):

$$2t = m\lambda \qquad (constructive\ reflection\ from\ thin\ film,\ no\ relative\ phase\ shift)$$

$$2t = \left(m + \frac{1}{2}\right)\lambda \quad (destructive\ reflection\ from\ thin\ film,\ no\ relative\ phase\ shift)$$

If *one* of the two waves has a half-cycle reflection phase shift, the conditions for constructive and destructive interference are reversed (for $m = 0, 1, 2, \ldots$) and we have:

$$2t = \left(m + \frac{1}{2}\right)\lambda \quad (constructive\ reflection\ from\ thin\ film,\ half-cycle\ relative\ phase\ shift)$$

$$2t = m\lambda \qquad (destructive\ reflection\ from\ thin\ film,\ half-cycle\ relative\ phase\ shift)$$

2.7 Effects on the properties of PMMA due to ion implantation

2.7.1 Effects on structural properties

During the trajectory inside the polymer, the ion leaves part of its kinetic energy during the collisions against the cloud of electrons and the nucleus of the atoms. Popok [7] mentions that even for low-energy regimes, the density of energy can be as high as a few hundreds eV per 1 nm of ion track length and, taking into account that the bond dissociation energy in polymers does not exceed 10 eV, the energy deposited by the projectile leads to multiple breakage of the chemical bonds within and around the ion path. In contrast to inorganic materials, breakage of the chemical bonds in polymers occurs by means of both the nuclear and electronic stopping. Thus, both nuclear and electronic stopping of ions in polymers lead to degradation of the organic host. There are two possible competing processes: (i) scission of molecular polymer chains resulting in fractionating and (ii) free radicals formation (branching) leading to cross-linking and bonds conjugation, as can be seen in Figure 26. Since material is modified in a small volume around the individual latent track (i.e. the highly disordered area along the ion trajectory), a number of projectiles bombarding the surface or , in other words, ion dose is a crucial parameter for polymer degradation. Therefore, one can distinguish two implantation regimes: (i) a single-track regime where the tracks are isolated from each other and (ii) a track overlapping regime, where the transition from the single track regime to the overlapping one occurs for doses range of $5 \cdot 10^{12} - 5 \cdot 10^{13}$ ion/cm^2 in the case of light ions and for lower doses in the case of heavy ions. This is because heavy ions produce larger diameter latent tracks.

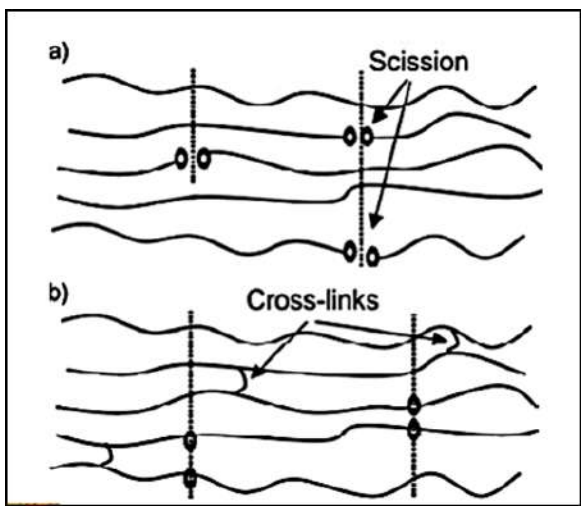

Figure 26: Schematic representation of a) scission of molecular polymer chains and b) cross-linking under ion implantation [7]

Popok [7] also mentions that the radiative and thermal processes interplay in a complex manner in every latent track and, thus, represent a unified phenomenon of radiothermolysis. This phenomenon creates gaseous compounds which can be emitted, leading to degassing from the polymer and it is especially pronounced for the case of low-energy implantation where the damage is formed in a shallow layer and gases can easily escape from low depth. A direct consequence of the degassing is an increase of carbon ratio in the implanted layer, i.e. carbonization of polymer (See Figure 27). The carbon "excess" is especially well pronounced in the case of implantation of heavy ions and located at a certain depth under the surface depending on the implantation energy and

type of polymer. The carbonization process is very sensitive to the nuclear stopping because it is more efficient in bond rupture and, thus, in degassing. Carbonization process is also dependent on type of polymer and its structure. When the initial content of carbon is higher, the carbon concentration in the shallow surface layer can reach 87-89 % under high-doses ($5 \cdot 10^{16} - 1 \cdot 10^{17}$ ion/cm^2). Finally, this process of the ion-induced carbonization of polymers under implantation of heavy ions is practically accomplished at the doses level of $(1-5) \cdot 10^{15}$ ion/cm^2. In the case of lighter ions, this occurs at higher doses.

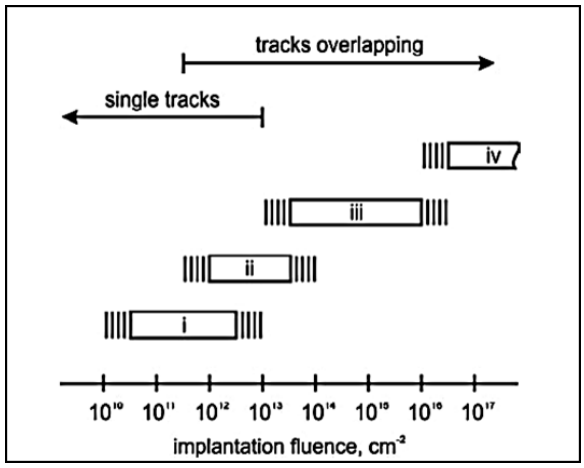

Figure 27: Stages of polymer carbonisation versus implantation dose (=fluence) [7]

Other authors found similar results. For example, Choi et al. [8] performed proton (hydrogen ions) implantation at an energy of 350 keV and doses ranged from $2 \cdot 10^{14}$ to $1 \cdot 10^{15}$ $ions/cm^2$ on PMMA in order to study its structural modification. Doing Infrared Spectroscopy and Raman Spectroscopy on samples of PMMA by proton implanted, it was found that the $C-O$, $C=O$ bonds and CH_2, CH_3 groups diminish with proton irradiation, and the Rutherford Back Scattering measurement showed the decrease of oxygen content; which means that the pendant group ($COOCH_3$) is readily decomposed and eliminated by outgassing with proton irradiation.

Arif et al. [6] explored the effects of C^+ ion implantation on PMMA at 400 keV and doses ranging from $5 \cdot 10^{13} - 5 \cdot 10^{15}$ ion/cm^2. Their Raman and FTIR (Fourier Transform Infrared Spectroscopy) spectra confirmed the cleavage and reconstruction of chemical bonds as well as formation of amorphous sp^2 carbon clusterization in irradiated PMMA. They concluded that the carbonaceous clusters are formed due to dehydrogenation processes during ion implantation and that made that the physical color of the ion implanted samples changes from transparent (pristine) to blackish brown ($5 \cdot 10^{15}$ ion/cm^2).

2.7.2 Effects on optical properties

As it was shown in 2.7.1, the ion implantation creates structural changes on PMMA. This change has further consequences in other properties of the PMMA, like its optical properties. Popok [7] mentions in his review that optically transparent polymers acquire some color after implantation, which changes from pale yellow to deep brown or grey with the dose increase and metallic lustre appears at high doses ($\geq 1 \cdot 10^{15}$ ion/cm^2). He mentioned that this phenomenon is consistent with the red shift of the absorption edge and that this shift is caused by the carbonization, in particular,

by the nanodimensional carbon-enriched clusters. Another optical parameters such as refractive index and extinction coefficient change significantly under irradiation: refractive index is essentially dependent on the implantation energy and it is increasing function of dose.

Many sources show the effects of the ion implantation in the optical properties of the PMMA. Arif et al. [6], doing implantations of C^+ ions at 400 keV on PMMA, studied the optical properties using UV-Visible Spectroscopy and they observed that Pristine PMMA shows 90% transmittance in the visible region (400–800 nm), but, as long as an increasing ion dose from $5 \cdot 10^{13}$ to $1 \cdot 10^{15}$ ion/cm^2 was used, a dramatic decrease in transmission was observed where finally, at dose of to $5 \cdot 10^{15}$ ion/cm^2, the percentage transmittance reduces to zero and the PMMA sample becomes opaque in the wavelength range 200–700 nm, as we can see in the Figure 28.

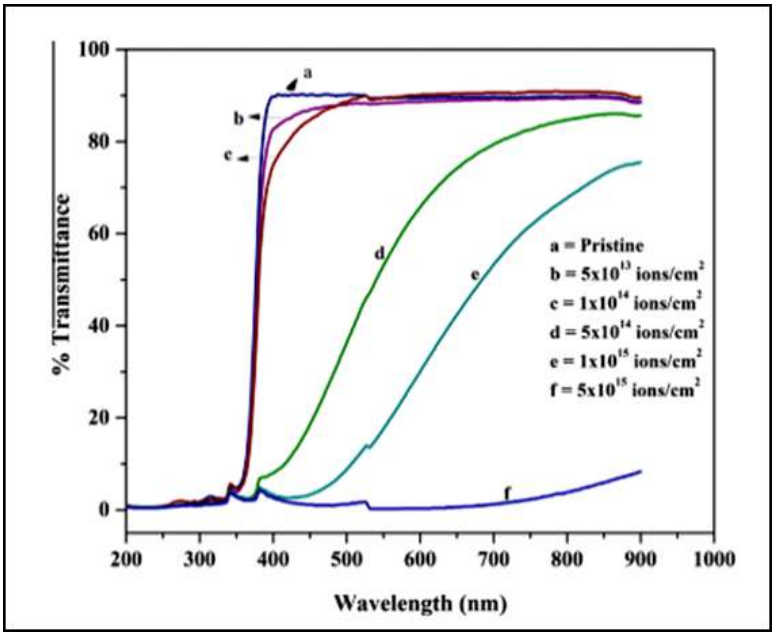

Figure 28: Optical transmission spectra of pristine and $^{12}C^-$ irradiated PMMA with 400 keV at different doses. [6]

Biersack and Kallweit [3] studied the ion beam induced changes of the refractive index of PMMA and they saw that for N^+ ions at dose $2 \cdot 10^{14}$ ion/cm^2 there was a linear dependence of the change of refractive index as a function of ion energy, but just from 100-350 keV. Also they showed that there was a proportional dependence between the change of refractive index and the dose used in the implantation in the range of $(0.1 - 4) \cdot 10^{14}$ ion/cm^2.

Stoyanov et al. [4] implanted Si^+ ions at 50 keV and at $3.2 \cdot 10^{15}$ ion/cm^2 on PMMA. They performed Monte-Carlo simulations of the spatial distributions of the deposited energy in the depth and pointed out that the projected range of the 50 keV Si^+ ions in PMMA should be shorter than 100 nm, so that the refractive index should change drastically close to the surface. Their measurements show that the maximum values of the refractive constants were found in the surface of the Si^+ - implanted PMMA, which revealed a significant modification of PMMA related to the hydrogenated amorphous carbon formation in the ion-modified surface layer.

Hong et al. [30] evaluated the optical property modification of PMMA by proton (i.e. H^+) ion-beam implantation at 350 keV at doses ranging $(2 - 10) \cdot 10^{14}$ ion/cm^2 and it was found that

higher doses introduces large variation of the refractive index. Also, in the depth profile of the refractive index, it was found that the variation of this one is related to the energy transfer ratio from implanted protons to polymer molecules which is directly related to the stopping power of proton.

Gupta et al. [5] studied the optical characterization of PMMA implanted by 100 keV N^+ and Ar^+ ions up to a maximum dose of $2 \cdot 10^{16}$ ion/cm^2. It was found a clear increase in the values of the refractive index as an effect of ion implantation dose corresponding to both of the ions. It has also been observed that the changes induced by the implanted ions are more pronounced for N^+ ions in comparison to Ar^+ ions. They say that this result can be justified by considering the range of these ions in PMMA polymer. As calculated using SRIM, the range of these ions have been found to be 342 nm and 148 nm for N^+ and Ar^+ ion in PMMA, respectively, at the same energy of the incident ion. Since N^+ ion has impinged PMMA deeply as compared to Ar^+ ion in the host polymer, hence, the modifications produced due to ion implantation are more prominent in the case of N^+ ion implantation as compared to Ar^+ ion.

Finally, Balabanov et al. [31] studied the optical properties of Si^+ implanted PMMA at energies $30 - 50$ keV and at ion doses ranging from $1 \cdot 10^{13}$ ion/cm^2 to $1.2 \cdot 10^{17}$ ion/cm^2. Their results demonstrated that the optical absorption of Si^+ implanted PMMA could be significantly altered, both in the visible and the infrared range, depending on the ion energy and dose. For higher energies, the ion beam induced absorption increase with the dose exhibits declination point type of behaviour, which is absent in the lower energy case, which was explained presumably due to an increased defect introduction above some critical concentration causing an abrupt increase of structural disorder.

3 Experimental Methods

3.1 Sample preparation

3.1.1 Cleaning procedures of the silicon wafers

As it was mentioned in the subsection 2.2, there are several types of cleaning processes for silicon wafers. In the present research, two wet cleaning processes were used: the RCA method by Kern and Poutinen [11], and the solvent cleaning using Acetone and Ethanol.

The RCA method (Figure 29) consists of two steps: the first one, called RCA-1, is the alkaline step in which was used a solution of $H_2O_2 - NH_4OH - H_2O$ in the proportion of 1:1:5. It was prepared as follow:

- First, the deionized water was putted in a Pyrex beaker.
- Second, NH_4OH (25%) was added and then heated to 70 ± 5 °C on a hotplate.
- Third, once the temperature was reached, the Pyrex beaker was removed from the hotplate and H_2O_2 (30%) was added.
- Fourth, when the solution started to bubble vigorously after 1-2 minutes, that indicated the solution was ready for use. Then, the silicon wafers were soaked in the solution during 15 minutes.

The second one step, called RCA-2, is the acidic step in which was used a solution of $H_2O_2 - HCl - H_2O$ in the proportion of 1:1:6. It was prepared as follow:

- First, deionized water was putted in a Pyrex beaker.
- Second, HCl (37%) was added and then heated to 70 ± 5 °C on a hotplate.
- Third, once the temperature was reached, the Pyrex beaker was removed from the hotplate and H_2O_2 (30%) was added.
- Fourth, when the solution started to bubble vigorously after 1-2 minutes, that indicated the solution was ready for use. Then, the silicon wafers were soaked in the solution during 10 minutes.

Figure 29: Compounds used in the RCA cleaning method

The solvent cleaning process using Acetone and Ethanol also consists of two steps: the first one with Acetone and the second one with Ethanol using a ultrasonic bath (Figure 30.a). Each step consists of the following:

- Fill a small vial halfway with the respective solvent,
- put the samples in,
- put the vial in a ultrasonic bath (SONOREX ^{TM} by Bandelin) by 10 minutes (Figure 30.b).

(a) Solvents and ultrasonic bath used (b) Vial in the ultrasonic bath

Figure 30: Cleaning process with solvents: Acetone and Ethanol

It should be noted that, in both procedures used, the solution from the surface of the silicon wafer was removed using deionized water after each step. And also, after the final step in both procedures, it was necessary to dry the surface with an Argon jet because the water on the surface can contain organic residues that could redeposit on the wafer surface again. This is an important consideration because this determines the homogeneity (i.e flatness of the surface) of the PMMA coating layer. In the Figure 31, one can see the difference between using and not using the deionized water and Argon jet in the cleaning procedure of the samples.

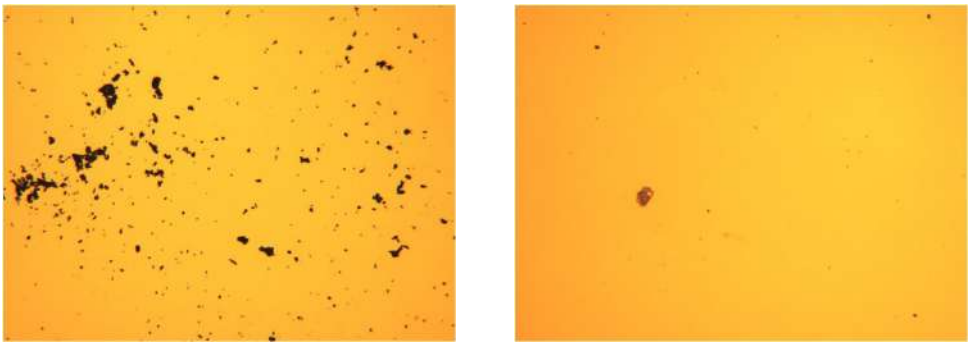

(a) (b)

Figure 31: a) Sample cleaned without deionized water between each step and without the use of the Argon jet at the end of the cleaning procedure, b) Sample cleaned with deionized water between each step and with the use of the Argon jet at the end of the cleaning procedure

After performing any of the cleaning procedures described above, the samples were observed under the microscope (OLYMPUS BX51 Fluorescence Microscope Cutaway Diagram, see Figure 32) in order to observe how successful was the cleaning. At the end, the cleanest ones were selected from the whole set.

Figure 32: Microscope OLYMPUS BX51 Fluorescence Microscope Cutaway Diagram

3.1.2 Coating procedure of the silicon wafers

The procedure used was described in the Subsection 2.3 . The used coating was "E-Beam Resist PMMA 950K AR-P 672.08" by Allresist GmbH. According to the description of the product [32], the solid content is 8.0 % , the viscosity (at 25 °C) is 211 $mPas$ and has a density (at 20 °C) of 1.005 g/cm^3. Two different spin coaters were used: SPIN 150, whose rotational speed reaches up to 6000 RPM (see Figure 33.a); and the spin coater SCC-200 by Novocontrol Technologies GmbH & Co. KG, whose rotational speed reaches up to 12000 RPM (see Figure 33.b).

(a) Coater SPIN 150

(b) Coater SCC-200

Figure 33: Spin coaters used

Different parameters were tested in order to try to obtain different coating thicknesses of the PMMA (see Figure 34). The ranges of the parameters tested were the following:

- Time of spin coating, ranging from 15 to 60 seconds (s);
- Acceleration, ranging from 500 to 1250 RPM/s;
- Quantity of PMMA deposited, ranging from 30 to 70 μL;
- Rotational speed, ranging from 1500 to 10800 RPM.

Figure 34: Set of silicon wafers coated with PMMA

3.2 Implantation

In this research, three different ions were implanted: Germanium ($^{74}Ge^-$), Hydrogen ($^1H^-$) and Carbon ($^{12}C^-$). The ions of Hydrogen (using TiH_2 as a cathode), Germanium (using germanium crystal as a cathode) and Carbon (using Graphite as a cathode) were implanted according to the Table 1:

Ion: $^1H^-$			
Energy and Dose	30 keV at 3E+16	90 keV at 1E+16	83.4 keV at 1E+16
Coating Thickness	9.519 μm 1.521 μm 0.930 μm 0.703 μm	9.519 μm 1.521 μm 0.930 μm —	— — — 0.703 μm
Ion: $^{12}C^-$			
Energy and Dose	30 keV at 1.5E+16	83.4 keV at 1E+16	
Coating Thickness	9.519 μm 1.521 μm 0.930 μm 0.703 μm	9.519 μm 1.521 μm 0.930 μm 0.703 μm	
Ion: $^{74}Ge^-$			
Energy and Dose	30 keV at 1.5E+16	90 keV at 1E+16	
Coating Thickness	— — —	9.519 μm 0.930 μm 0.690 μm	

Table 1: Plan of the implantations

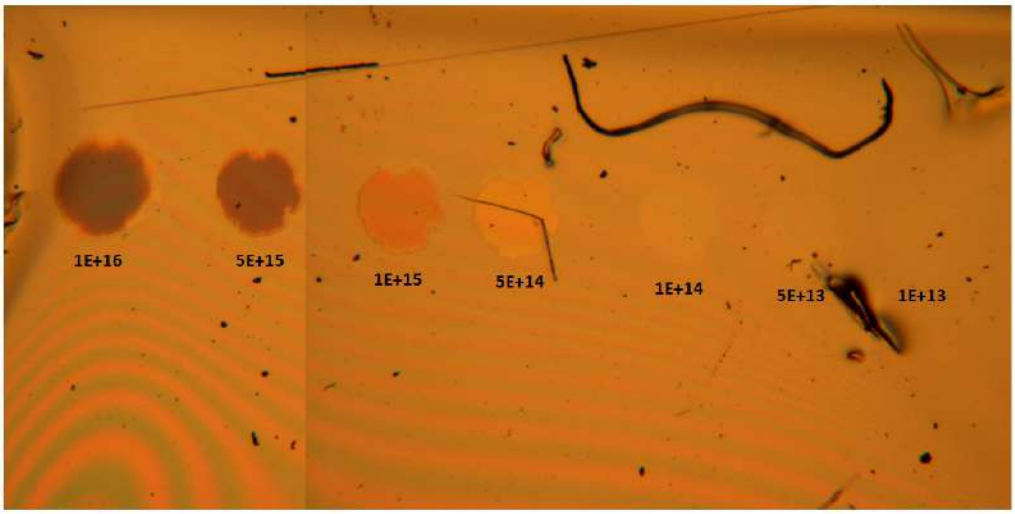

Figure 35: Implantations with $^{74}Ge^{-}$ ions in a sample with PMMA coating thickness of 1.864 μm with doses ranging between 5E+13 ion/cm^2 to 1E+16 ion/cm^2 at 90 keV.

It is necessary to mention one comment about the energies used in the implantations. At the beginning, the plan was to test a low energy and a high energy, 30 keV and 90 keV respectively. However, due to technical reason of the ion implanter, it was not allowed to continue with the initial high energy 90 keV any more. For that reason, the subsequent high energy implantations had to be done with 83.4 keV.

After the implantations that appear in the Table 1, another implantations with $^{1}H^{-}$ ions were performed at doses of 2.5E+15, 6.1E+14, 2.4E+14 and 4.1E+13; one next to the other, and at energy of 83.4 keV, in the sample with coating thickness of 0.703 μm. The same was done with $^{74}Ge^{-}$ ions, which were implanted in the sample with the coating thickness 1.864 μm in seven different spots, where each spot had a different dose: 1E+16, 5E+15, 1E+15, 5E+14, 1E+14, 5E+13 and 1E+13 (see Figure 35). The energy used with $^{74}Ge^{-}$ ions was 90 keV.

3.3 Thickness and topography measurements

Once the coated samples were obtained, the measurement of the coating thickness of the PMMA were performed. For that end, the profilometer DektakXT by BRUKER of the Semiconductor Department of the Universität Leipzig was used. In order to obtain the height step, the coated samples were scratched at the center, where the coating was more homogeneous. A pin that had enough hardness to scratch the PMMA but not the silicon wafer was used. The parameters used in the DektakXT profilometer were the following:

- Profile: Hills and Valleys
- Scan duration: 10 seconds
- Scan length: 500 μm
- Scan type: standard scan
- Stylus scan range: 6.5 μm

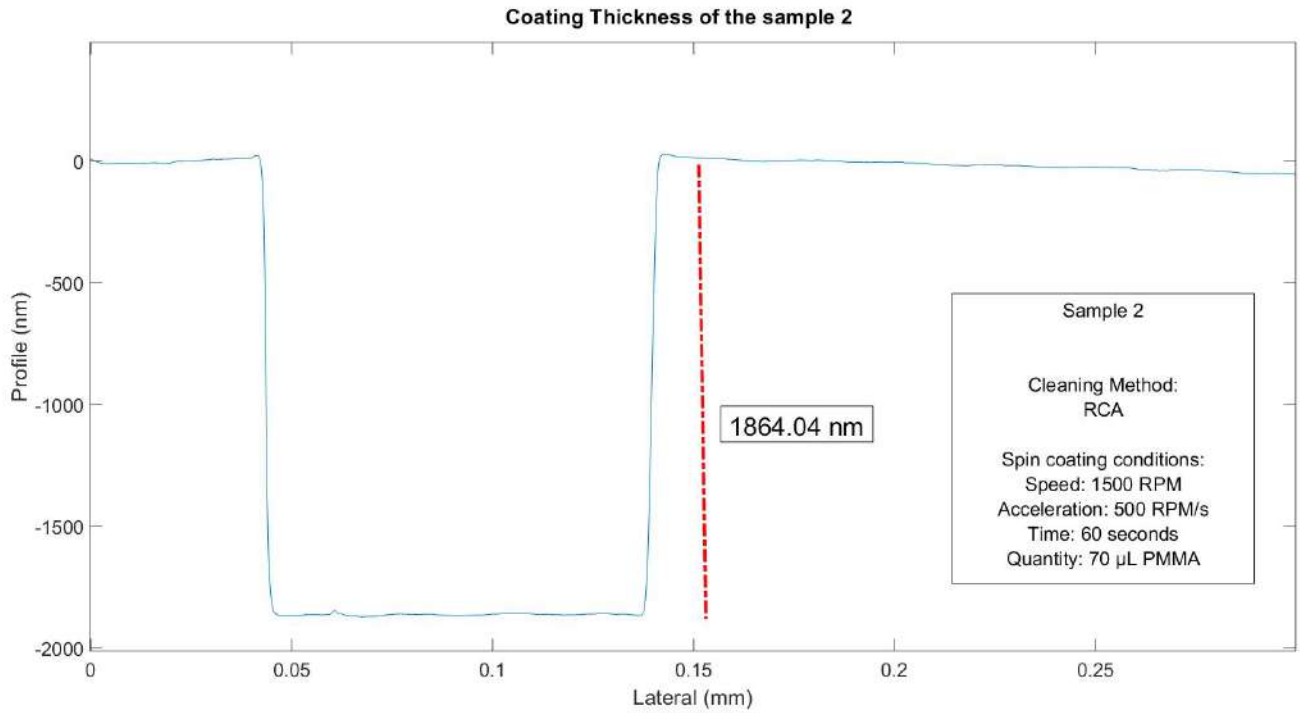

Figure 36: Profile of the sample 2 in the scratched area. The dashed red line represents the scratch depth and thus the thickness of the PMMA coating. The value of the thickness is shown in a box next to the red dashed line in nanometers.

After the scan, the program display a window showing the profile of the scanned path. Positioning two cursors, one labeled as **M**=measurement at the level of the surface of the PMMA and the other one labeled as **R**=reference at the position of the valley, it was possible to measure the value of the thickness of the PMMA.

After all the measurements of the thickness of the PMMA were carried out (see an example of one measurement in the Figure 36), just 6 samples were selected for the ion implantations, which had the following cleaning methods and coating thicknesses:

- Sample 1: Acetone and Ethanol cleaning / 9.519 μm
- Sample 2: RCA cleaning / 1.864 μm
- Sample 3: Acetone and Ethanol cleaning / 1.521 μm
- Sample 4: Acetone and Ethanol cleaning / 0.930 μm
- Sample 5: Acetone and Ethanol cleaning / 0.703 μm
- Sample 6: Acetone and Ethanol cleaning / 0.690 μm

Once the implantations were made, the Atomic Force Microscopy model XE-150 by Park Systems (see Figure 37) of the Semiconductor Department of the Universität Leipzig was used in order to measure the roughness of the PMMA surface layer.

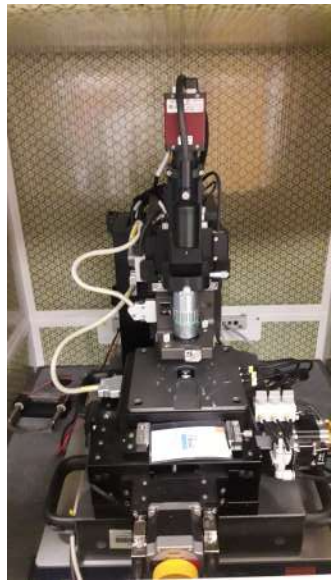

Figure 37: Atomic Force Microscopy (AFM) model XE-150 by Park Systems

For the spots implanted with ions of hydrogen ($^{1}H^{-}$) and germanium ($^{74}Ge^{-}$) at the doses described in the last paragraph of the subsection 3.2, the profilometer DektakXT was used in order to measure if there was a change in the PMMA thickness. As these implanted spots were done one next to each other, then with one single measurement was possible to measure the profile of all of them. The parameters used in the DektakXT profilometer in that case were the following:

- Profile: Hills and Valleys; this option provides 50 % of the measurement range above the zero horizontal grid line and 50 % below, which is a good option if the surface characteristics of the sample are not well known.
- Scan duration: 20 seconds
- Scan length: 800 μm
- Scan type: standard scan
- Stylus scan range: 6.5 μm

4 Results and discussion

4.1 Video Analysis of the implantations

Several sources in 2.7.2 like Arif et al. [6], Popok [7] and Balabanov et al. [31], mention that the color of implanted area changes during the implantation. This is something that can be monitored live with a microscope inside the sample chamber (see Figure 38).

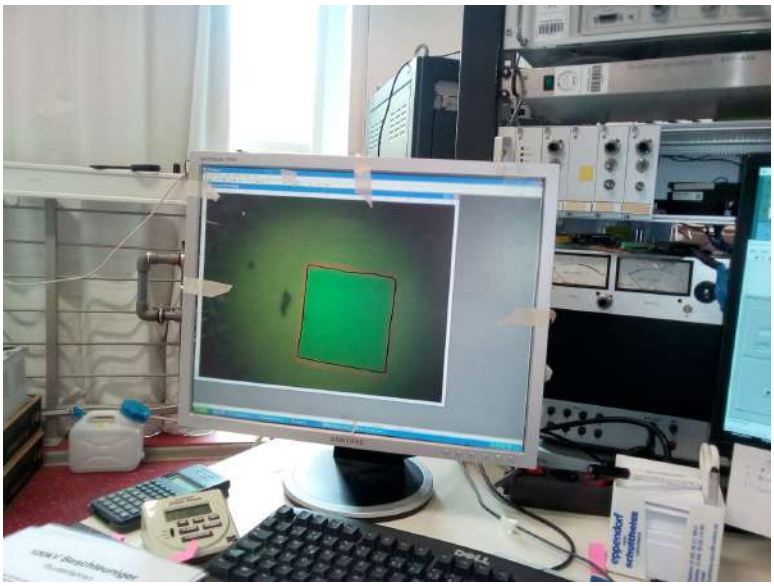

Figure 38: Live monitoring of implantation. The image shows the color of the implanted area in the PMMA with aperture of 240 μm x 240 μm at 90 keV with $^1H^-$ ions at some particular dose in the sample with coating thickness 0.930 μm. The black line bordering the implanted area was drawn with a marker just to identify the position of the spot in the screen; it is not a result of the ion irradiation.

As the microscope is connected with a video-camera program of the computer, I had the idea to record videos of each performed ion implantation, which allowed me to do a better analysis when recording the color of the spot over time. Since a constant current was assumed during the implantation, each timestamp of the video could be converted to implantation dose. And therefore, the color information of the spot during the implantation could be related with one dose.

One video was recorded for each implantation condition presented in the Table 1 of the subsection 3.2. At the end, 19 videos were recorded. Then, using the analysis program MATLAB, the frames of each video were extracted and these ones were converted in the gray scale. Then, the implanted area was selected in each frame in order to generate plots in which one can analyze the change of the intensity in the gray scale against the implanted dose. Using the original frames (i.e. without converting to gray scale), the information of the three primary colors, red-green-blue (RGB) was extracted and, following the same procedure as before, the intensity of each color against the dose was plotted. The original values of the intensities go from 0 to 255. But these ones were normalized in all the plots using as a reference the highest value of each plot. Finally, from these two kind of plots, it was possible to do an analysis between the different coating thicknesses, ion energies and ion species. It is important to say that the parameters of the records were similar in the all videos in order to assure that the information obtained from them were comparable.

4.1.1 Color Change under different coating thicknesses

The PMMA coating thicknesses used in the video recordings of the implantations can be classified in two groups: the thicker samples (9.519 μm and 1.521 μm) and the thinner samples (0.930 μm, 0.703 μm and 0.690 μm). These two groups presented different behaviours in the color change during the implantations, which are going to be described and discussed onwards.

4.1.1.1 Thicker samples

Almost all the plots of the color change with the thicker samples (independently of the ion energy and ion species used) presented a behaviour as it appears as examples in the Figure 39 and Figure 40.

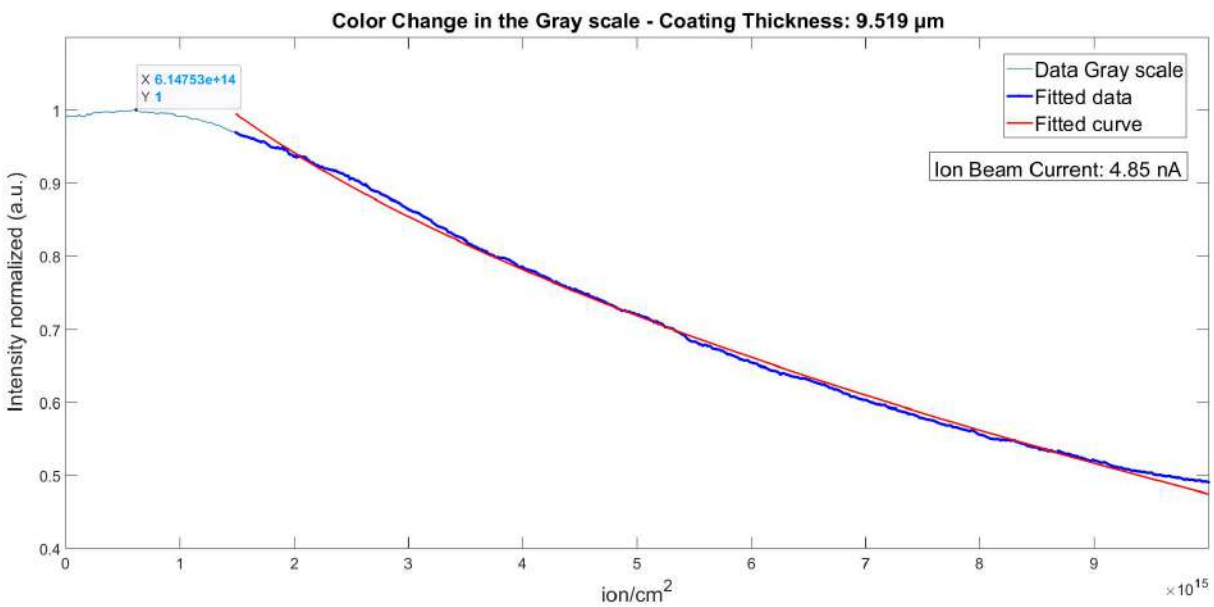

Figure 39: Plot in the gray scale using $^1H^-$ implantation at 90 keV with a dose of 1E+16 ion/cm^2 and coating thickness 9.519 μm.

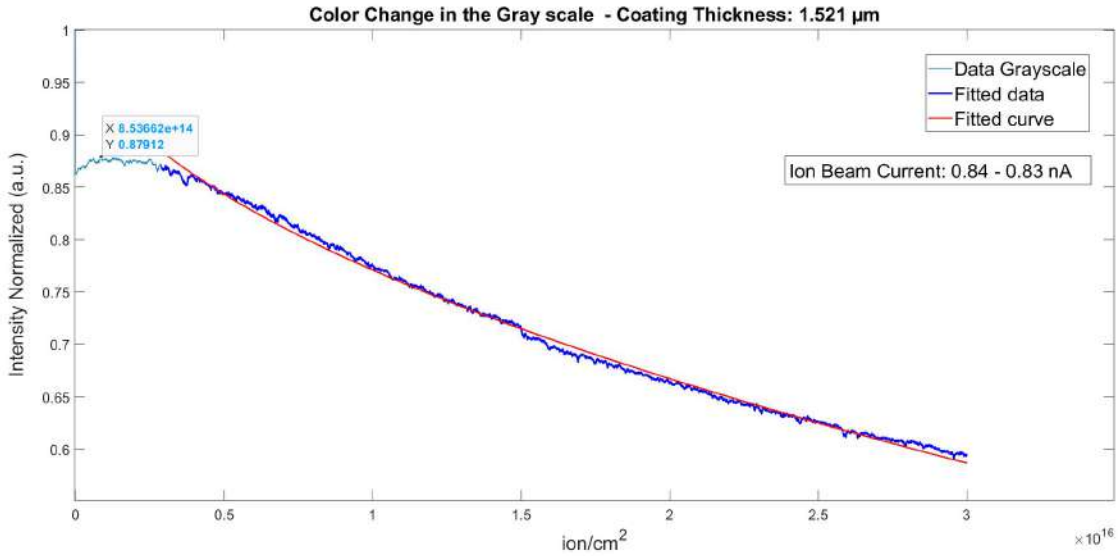

Figure 40: Plot in the gray scale using $^1H^-$ implantation at 30 keV with a dose of 3E+16 ion/cm^2 and coating thickness 1.521 μm.

From the plots, one can see that at the beginning there is not a clear change of the intensity (i.e. there is not a color change in the PMMA which one can observe with the naked eye in the video), no matter if one uses 90 keV, 83.4 keV or 30 keV. But then, at some particular dose (depending of the ion energy, ion species and coating thickness used, see all the values in the Appendix A) the intensity starts to decay as a long tail. In Figure 41 one can see , for instance, a comparison between the $^1H^-$ and $^{12}C^-$ ion at the doses in which the intensity decay begins respect to the ion energy used.

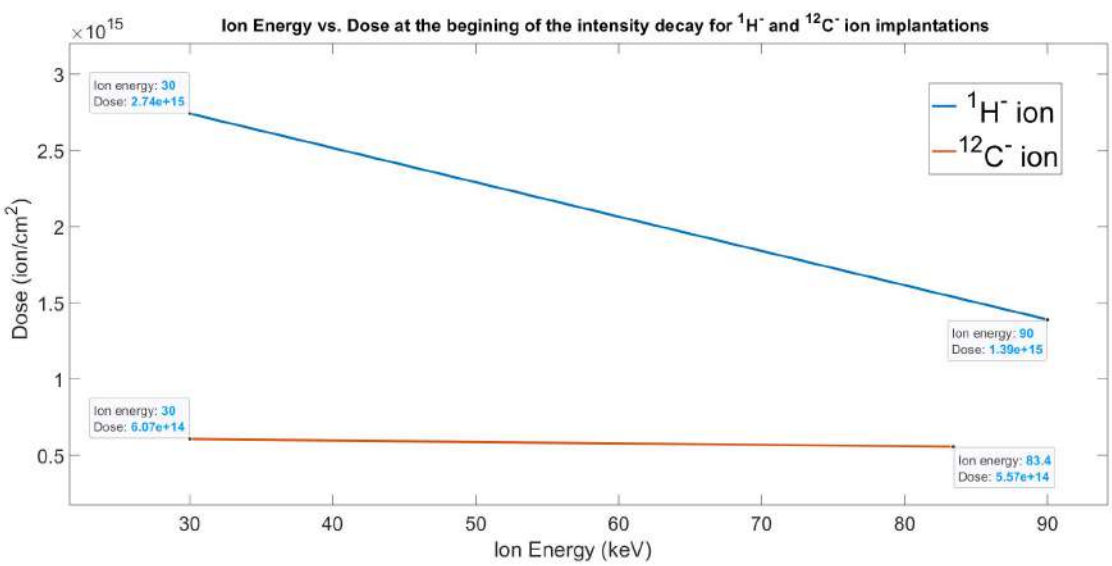

Figure 41: Plot which compares how the doses at the beginning of the decay changes when the ion energy changes with different ion species. The value of doses used in this plot are the average of the doses of all different coating thicknesses for some particular ion energy and ion species (see all the values used in Appendix A).

From this Figure 41, one can see that keeping constant one of the two ions, if one increases the ion energy (from 30 keV to 83.4 or 90 keV), the dose necessary to start to see the decay decreases. On the other hand, keeping constant one of the two ion energy values, if one increases the weight of the ion (from $^{1}H^{-}$ ion to $^{12}C^{-}$ ion), then the dose necessary to start to see the decay also decreases.

The decay of the intensity in the plots is observed in the videos as a darkening of the irradiated area in the PMMA. Comparing these doses with the Figure 27 of the subsection 2.7.1, one can see that these ones are in the stage III of the polymer carbonisation. In this stage III there is an aggregation of the carbon clusters up to formation of the quasi-continuous carbonaceous buried layer characterised by the network of conjugated bonds so that, for doses higher than these ones, the transition of the carbonised phase to amorphous carbon or graphite-like material starts (stage IV of the polymer carbonisation), as Popok [7] mentions. That could explain why the color of the irradiated area starts to change to a darker color (blackish brown color), as also Arif et al. [6] found for the implantation of C^{+}. This explanation has coherence with what was observed in the Figure 41. Heavier ion and higher ion energies produce a greater structural damage in the implanted zone of the PMMA and consequently it accelerates the carbonisation process, being able to observe the beginning of the intensity decay (darkening of the PMMA) with lower doses. The data in the region of intensity decay was fitted with a fitting function. After trying many fitting functions (like exponential, logistic, etc.), the power function ($f(x) = a * x^{b} + c$) was the one that best fit the data in all cases. The coefficients of the power function for each plot that appear in this research are listed in the Appendix B.

As I discussed at the beginning of this section, almost all the plots of the color change with the thicker samples showed a behaviour similar as in the Figure 39 and Figure 40. However, there was one implantation (with $^{1}H^{-}$ ions and at 90 keV) that showed a different pattern before the intensity decay starts, which can be observed in the Figure 42.

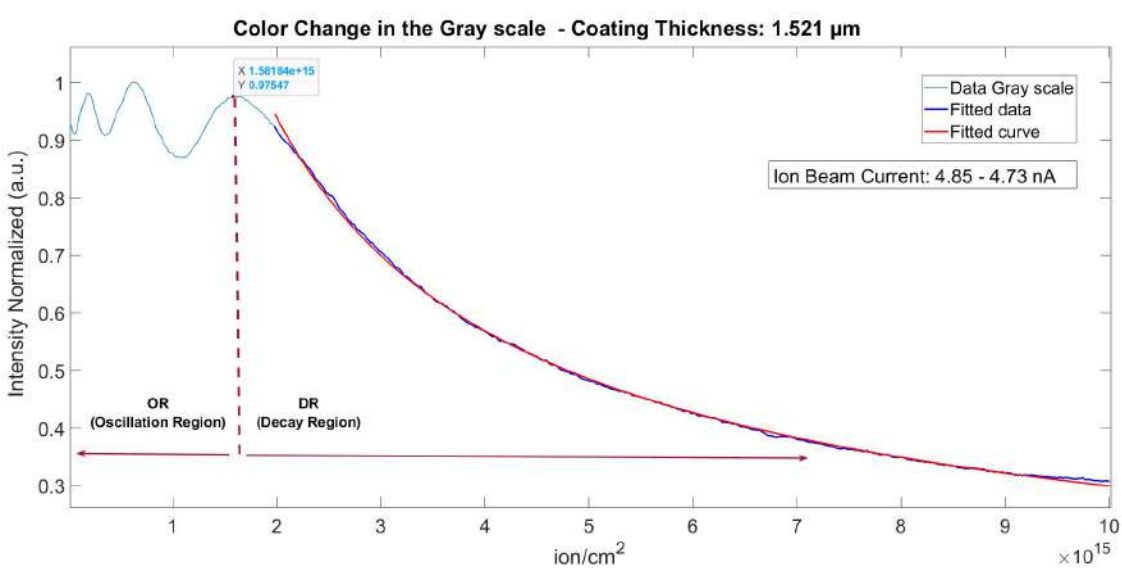

Figure 42: Plot in the gray scale using $^{1}H^{-}$ implantation at 90 keV with a dose of 1E+16 ion/cm^{2} and coating thickness 1.521 μm.

In the Figure 42, we can see clearly that before the intensity decay starts, there is an oscillation of the intensity (i.e. a change of color in the irradiated area before the dose 1.58E+15 ion/cm^{2}, observing in the video an oscillating between the red and green color). At this point, it is better to

label these two observed regions by: oscillation region as OR and decay region as DR, which also are going to be used in the following sections. This oscillation in the OR could be explained using the ion range and the damage plots generated by SRIM simulation using $^1H^-$ ions at 90 keV. The Figure 43 show the respective ion range and penetration depth for this implantation conditions.

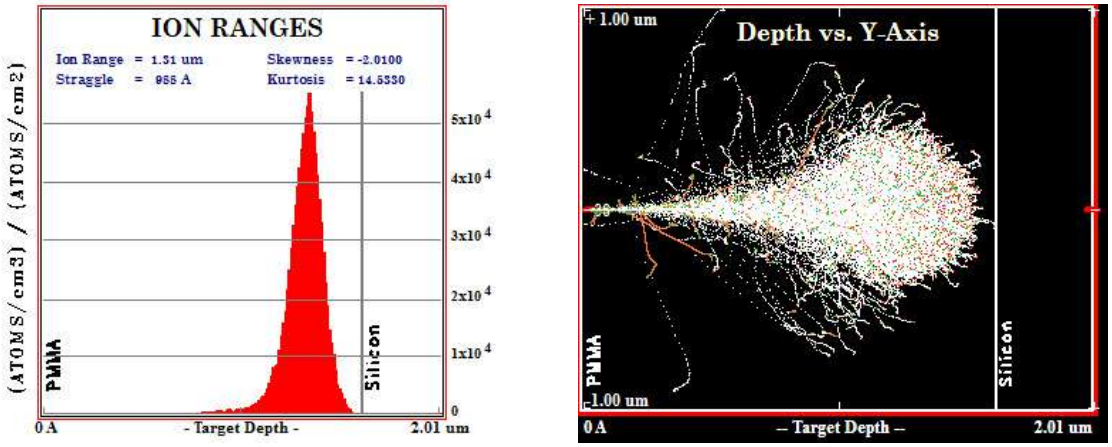

(a) Ion Range distribution

(b) Penetration depth

Figure 43: Plots of the Ion Range distribution (a) and Penetration depth (b) generated by SRIM simulation for $^1H^-$ ions at 90 keV with a PMMA layer of 1.521 μm on a Si substrate, using 10000 ion histories and the full damage cascade option

The peak concentration of $^1H^-$ ions are located 1.31 μm deep from the surface of the PMMA layer, which implies a damage in the PMMA layer until that depth generated during the whole trajectory done by the majority of the $^1H^-$ ions implanted. This can be observed in the Figure 44, which shows the Target (PMMA) displacements generated in this implantation.

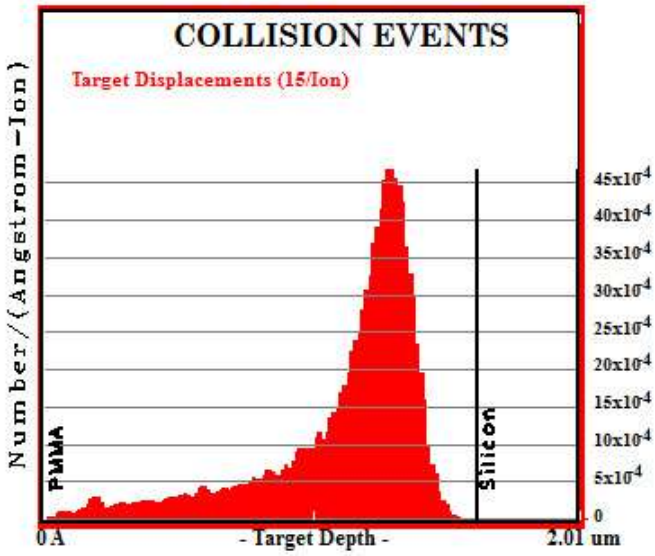

Figure 44: Plot of the Target displacements generated by SRIM simulation for $^1H^-$ ions at 90 keV with a PMMA layer of 1.521 μm on a Si substrate, using 10000 ion histories and the full damage cascade option

As one can see in the Figure 44, there are displacements of the target along the target depth, having a peak which occurs at the similar depth of the ion range. Thus, only the $^1H^-$ ions at 90 keV in a thicker sample could penetrate a substantial amount of the PMMA layer, generating a damage on it (like, for instance, many breakage of the chemical bonds which creates a degradation of the polymer structure) and could causing changes in the optical properties which manifested as a color change of the irradiated area during the implantation.

4.1.1.2 Thinner samples

All the plots of the color change with the thinner samples (independently of the ion energy and ion species used) presented a behaviour similar to those shown in the Figure 45 and Figure 46.

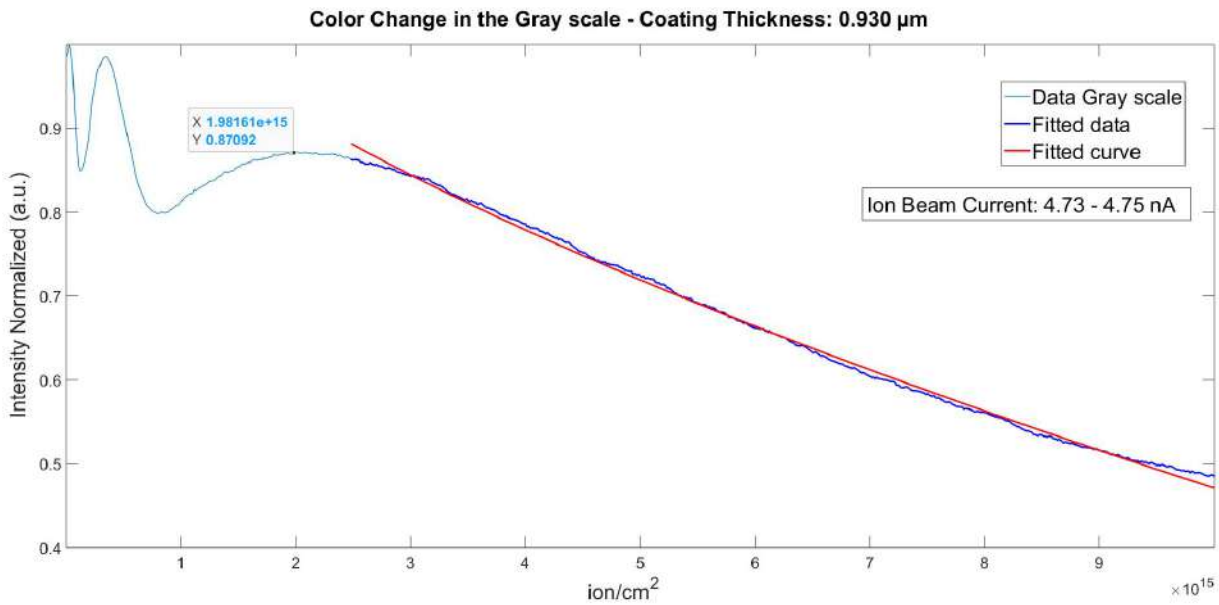

Figure 45: Plot in the gray scale using $^1H^-$ implantation at 90 keV with a dose of 1E+16 ion/cm^2 and coating thickness 0.930 μm.

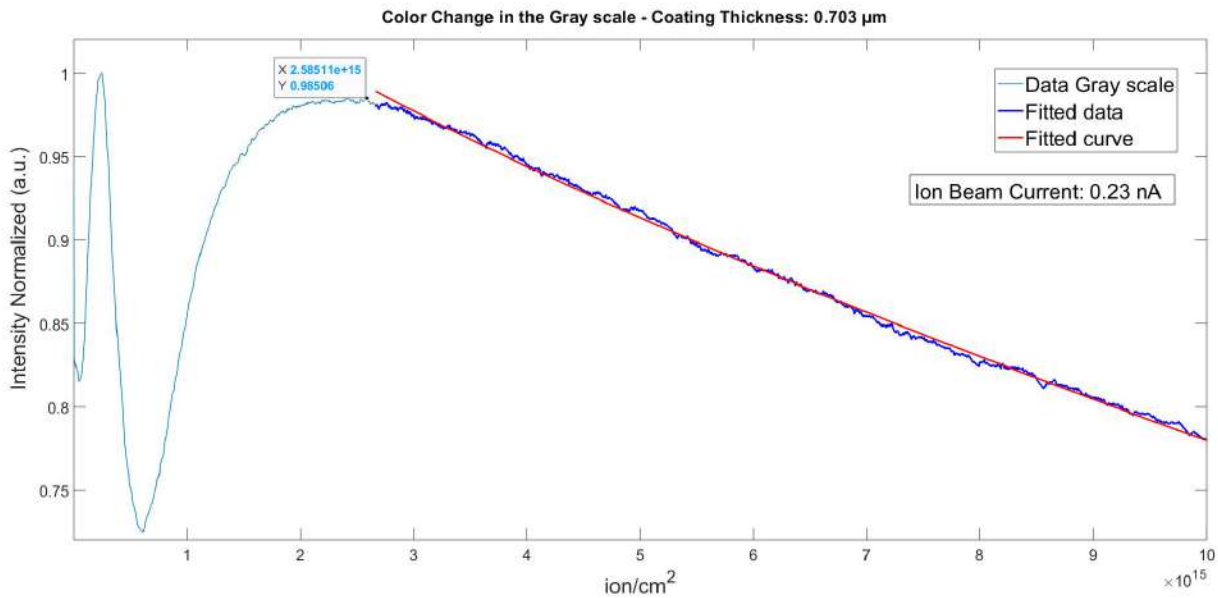

Figure 46: Plot in the gray scale using $^{1}H^{-}$ implantation at 83.4 keV with a dose of 1E+16 ion/cm^2 and coating thickness 0.703 μm.

From these two last figures, it is clear to distinguish the two regions defined in 4.1.1.1. The explanation of why the DR appears was discussed in 4.1.1.1. However, the particular feature of these thinner PMMA coating thicknesses is that the OR always appears , no matter if one uses 90 keV, 83.4 keV or 30 keV. This OR in the plots is observed in the videos as an oscillating color change between red and green. To understand better what could be happening in this region, plots with the Red-Green-Blue (RGB) channels respect to the gray scale were generated in order to get more information. As an example, we are going to use the RGB plot generated for the $^{12}C^{-}$ implantation at 83.4 keV with dose 1E+16 ion/cm^2 and coating thickness 0.703 μm (see Figure 47).

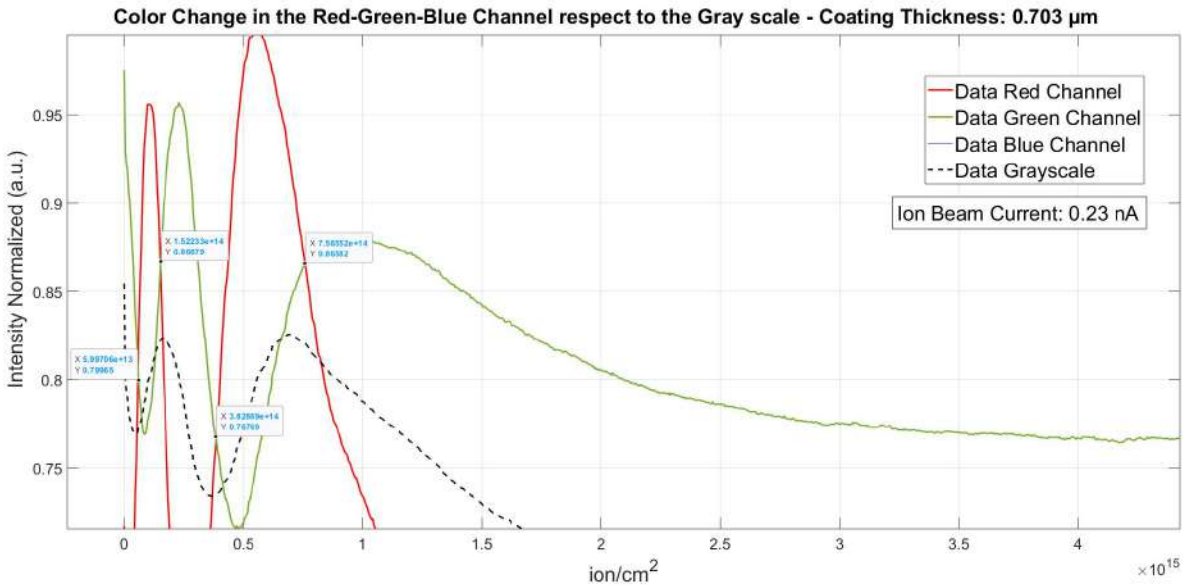

(a)

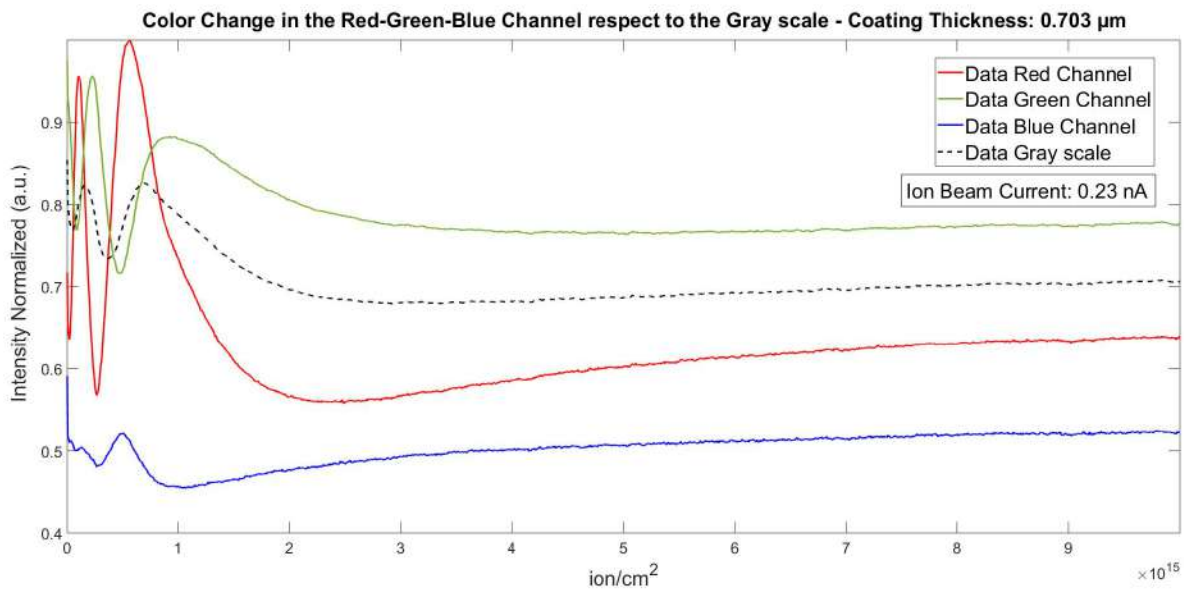

(b)

Figure 47: a) Part of the plot of the RGB channels respect to the Gray scale using $^{12}C^{-}$ implantation at 83.4 keV with a dose of 1E+16 ion/cm^2 and coating thickness 0.703 μm, which shows the doses and the intensities of the crossing points between the green and red channels in OR; and b) complete plot of the RGB channels of the same implantation.

From Figure 47, one can note that when the red and green channels curves cross each other, the dose in which that occurs coincides close to the dose when one peak or valley in the gray scale happens. This crossing always is placed between two continuous peaks or valleys of the two different color channels (green and red). It is also important to mention that the peaks of the color channels corresponded to the color observed in the implanted area during the implantation. In the Figure 48, one can see such prominent peaks for the $^{12}C^{-}$ implantation at 83.4 keV with dose 1E+16 ion/cm^2 and coating thickness 0.703 μm. Also, in the Figure 49 one can observe the frames of the video at the doses of the peaks in the green and red channels and at the doses of the peaks and valleys in the gray scale for the same $^{12}C^{-}$ ion implantation.

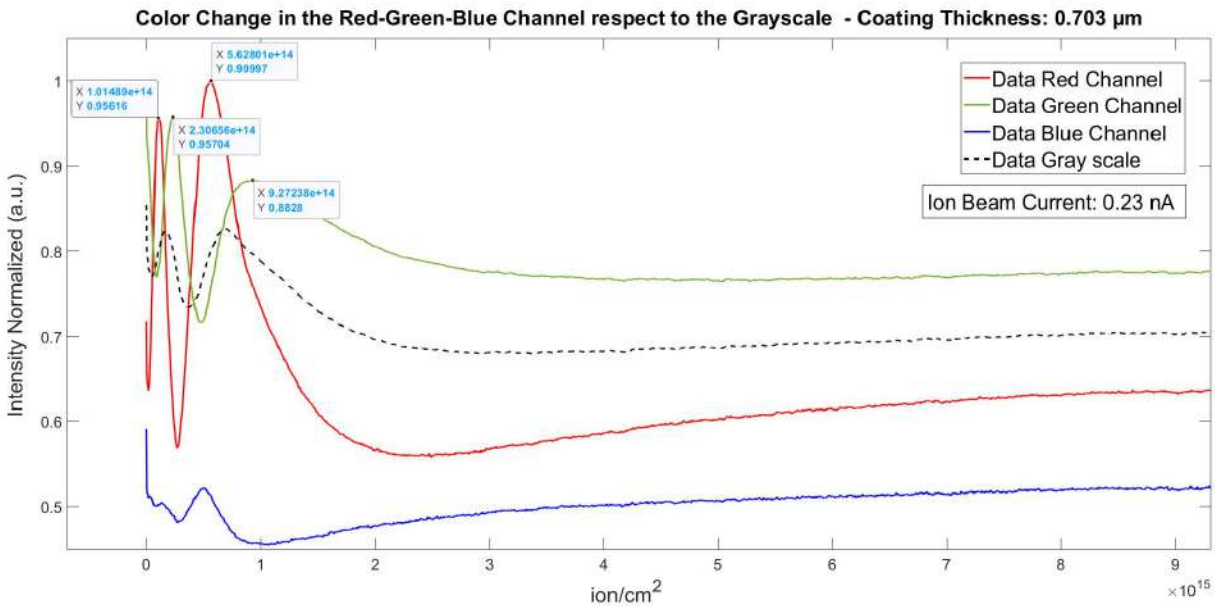

Figure 48: Plot of the RGB channels respect to the Gray scale using $^{12}C^{-}$ implantation at 83.4 keV with a dose of 1E+16 ion/cm^2 and coating thickness 0.703 μm. The plot shows the doses and the intensities in the peaks of the green and red channels

Many sources make reference to the final color (dark color) of the spot obtained after using doses equal to or greater than 10^{14} ion/cm^2, which is the well known result of the carbonisation process. But none of the found sources explain why there is an oscillation in the color before this darkening of the irradiated area of the PMMA. The Figure 49 clearly shows that the frames at some doses seem to repeat (49.a with 49.e, 49.c with 49.h and 49.b with 49.f), which could be telling me that there is an interference phenomenon involved during the implantation at the doses located in the OR.

(a) Dose: 5.07 E+13 ion/cm^2

(b) Dose: 1.01 E+14 ion/cm^2

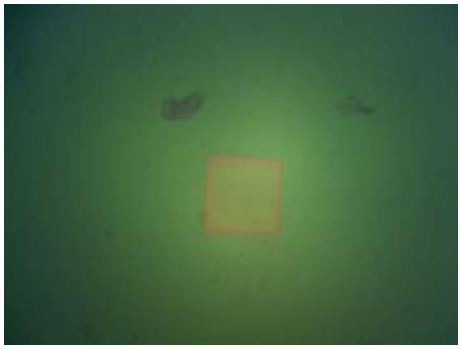

(c) Dose: 1.66 E+14 ion/cm^2

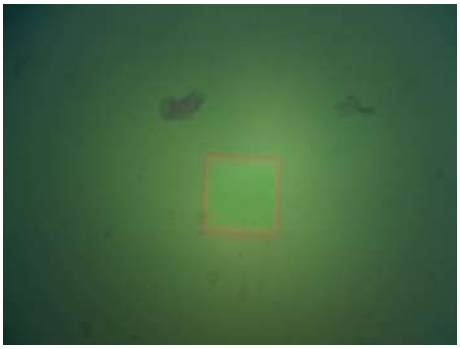

(d) Dose: 2.31 E+14 ion/cm^2

(e) Dose: 3.64 E+14 ion/cm^2

(f) Dose: 5.63 E+14 ion/cm^2

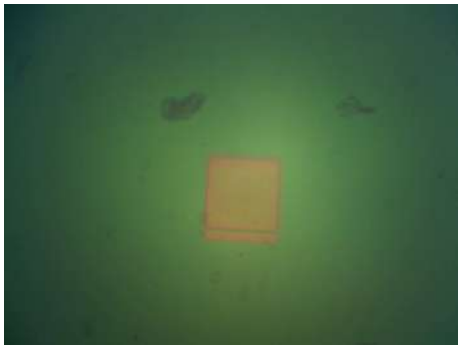

(g) Dose: 6.97 E+14 ion/cm^2

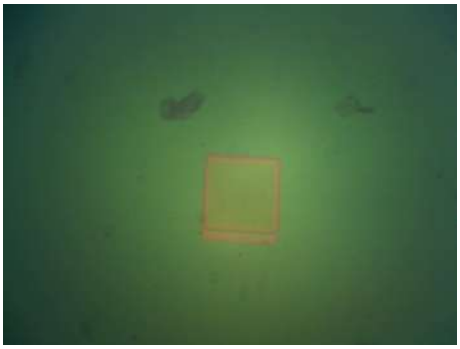

(h) Dose: 9.27 E+14 ion/cm^2

Figure 49: Frames of the video at the doses of the peaks in the green and red channels (b, d, f and h) and at the doses of the peaks and valleys in the gray scale (a, c, e and g) for the $^{12}C^-$ ion implantation at 83.4 keV in the sample with coating thickness of 0.703 μm

4.1.2 Color Change under different ion energies

The two classes of energies used in this research were: High Energy (90 keV or 83.4 keV) and Low Energy (30 keV). I used different doses for the different ion energies (1E+16 ion/cm^2 to 90 keV or 83.4 keV and 1.5E+16 or 3E+16 ion/cm^2 to 30 keV) in order to get approximately the same final deposited energy for both classes of energy. Such values of the doses were chosen because the value of the high energy was almost three times the value of the low energy. For some implantations at 30 keV I used a factor lower than three (one and a half) for the dose, which was enough to reproduce a comparable pattern of the color change respect to the high energy.

For the cases of $^1H^-$ and $^{74}Ge^-$ ion implantations, the general pattern and the number of peaks in the OR in the gray scale plots kept constant, no matter if we used the high or low energy. A good example is observed between the Figure 50.a and Figure 50.b.

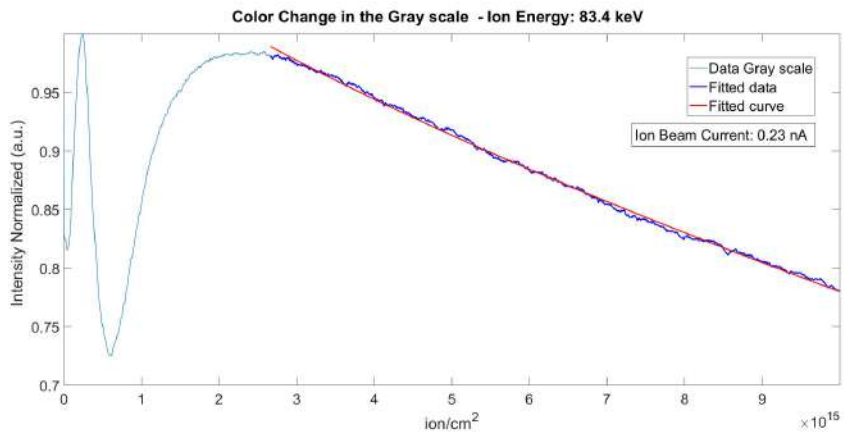

(a)

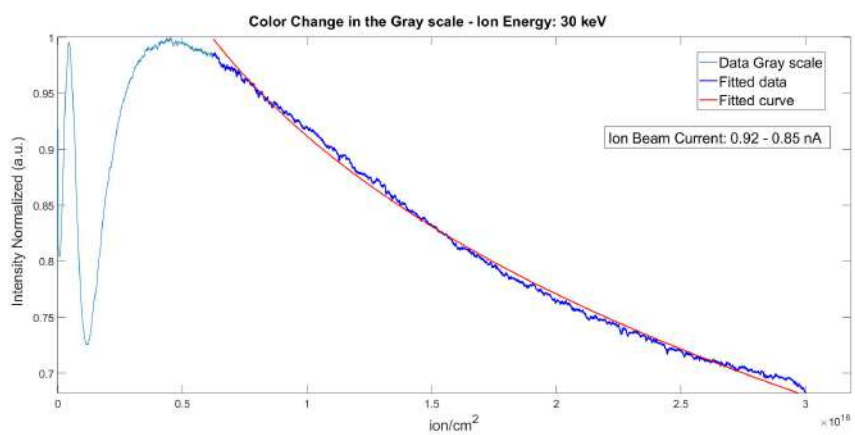

(b)

Figure 50: a) Plot in the gray scale using $^1H^-$ implantation at 83.4 keV with a dose of 1E+16 ion/cm^2 and coating thickness 0.703 μm and b) Plot in the gray scale using $^1H^-$ implantation at 30 keV with a dose of 3E+16 ion/cm^2 and coating thickness 0.703 μm. Comparing these two plots is clear that when one reduces the ion energy in approximately a factor of 3, then one have to increase the dose in approximately the same factor in order to reproduce the pattern with low energy as similar as possible to the high energy

However, for thinner samples, a notorious change related with the level of energy used was observed in the OR for the $^{12}C^{-}$ ion implantations, as one can see between the Figure 51.a and Figure 51.b.

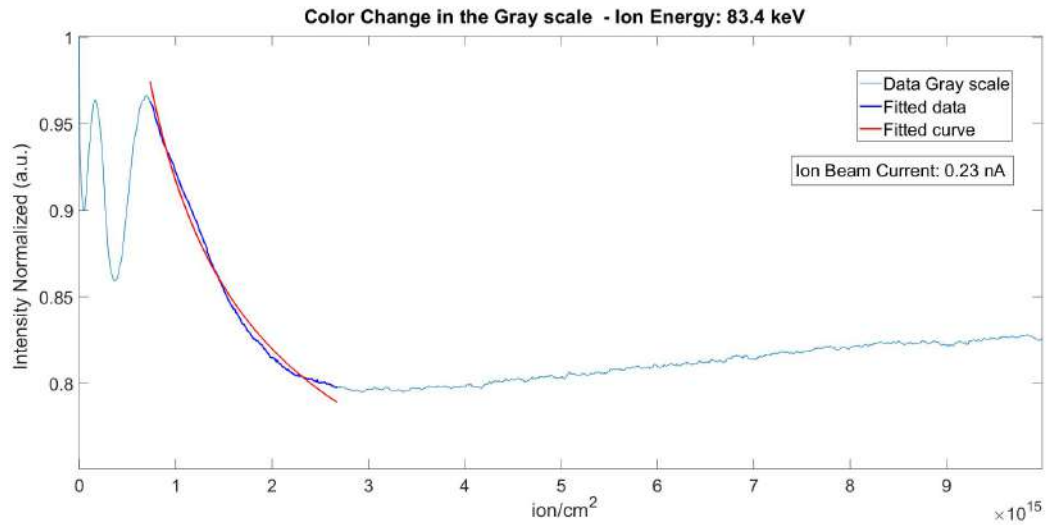

(a)

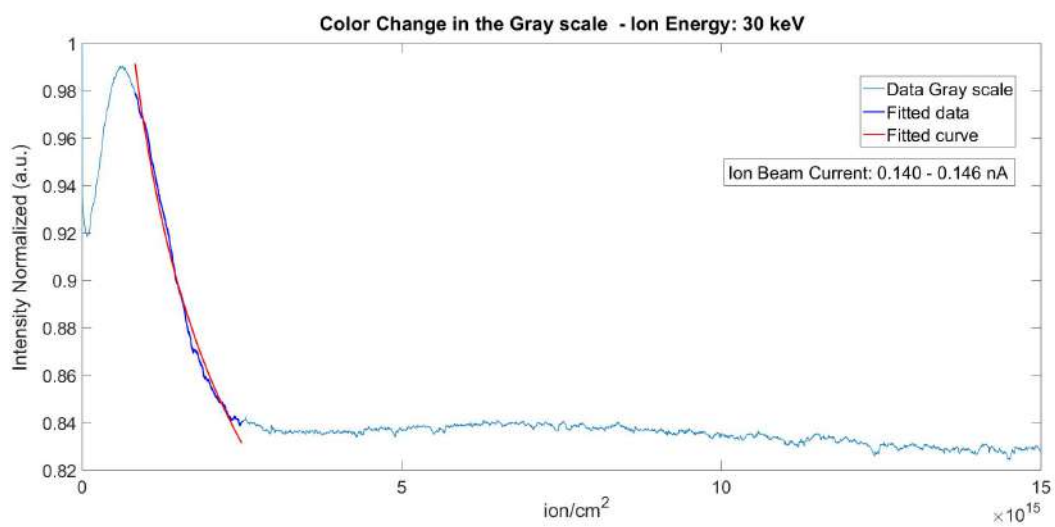

(b)

Figure 51: a) Plot in the gray scale using $^{12}C^{-}$ implantation at 83.4 keV with a dose of 1E+16 ion/cm^2 and coating thickness 0.703 μm and b) Plot in the gray scale using $^{12}C^{-}$ implantation at 30 keV with a dose of 1.5E+16 ion/cm^2 and coating thickness 0.703 μm

As one can note, at high energy (in this case 83.4 keV) one finds two peaks in the OR, but at low energy (30 keV) just one peak is seen. Also, this is seen with the coating thickness 0.930 μm for the $^{12}C^{-}$ ion implantations. In order to understand what could be the explanation for this difference, SRIM simulations were performed for these two energies. The first thing that one finds is that the average ion ranges are clearly different for these two cases (for 30 keV is 1684 Å = 0.1684 μm and for 90 keV is 4631 Å = 0.4631 μm), as one can note in the Figure 52.

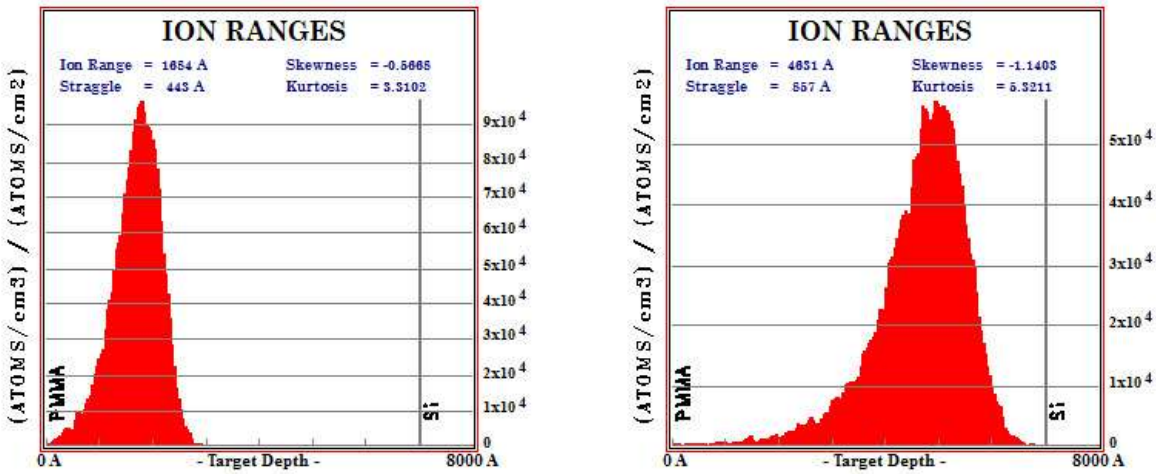

(a) (b)

Figure 52: a) Ion range under $^{12}C^{-}$ ions implantation at 30 keV with a total number of ions of 10000 and PMMA coating thickness 0.703 μm on Si substrate using SRIM simulation and b) Ion range under $^{12}C^{-}$ ions implantation at 83.4 keV with a total number of ions of 10000 and PMMA coating thickness 0.703 μm on Si substrate using SRIM simulation.

Also, comparing the energy losses between these two ion energies using the ionization plots generated by SRIM simulation, one can find that the loss of energy due to the interaction between the ion and the target electrons occurs in a greater region in the PMMA implanted with 90 keV respects to 30 keV (See Figure 53).

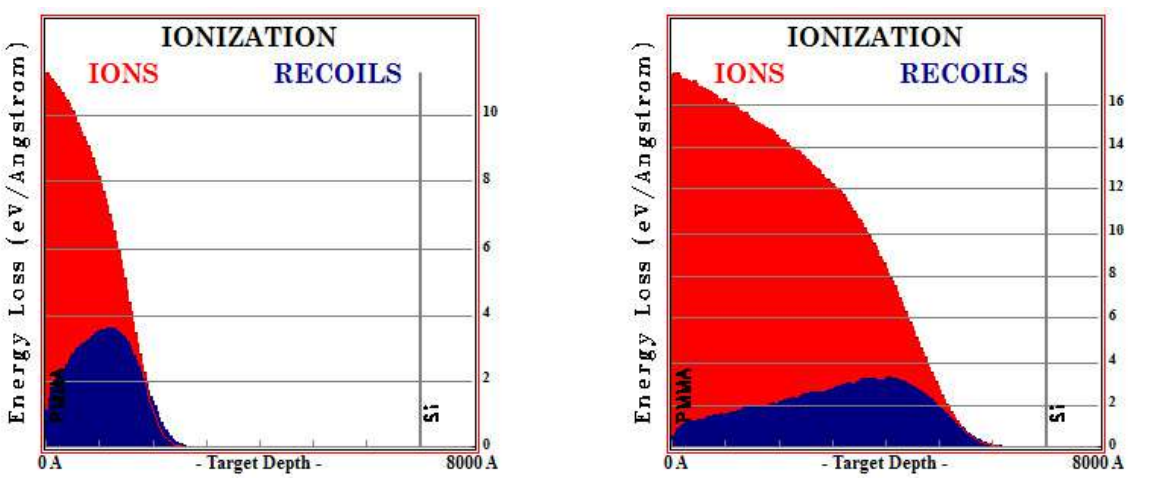

(a) (b)

Figure 53: a) Ionization under $^{12}C^{-}$ ions implantation at 30 keV with a total number of ions of 10000 and PMMA coating thickness 0.703 μm on Si substrate using SRIM simulation and b) Ionization under $^{12}C^{-}$ ions implantation at 83.4 keV with a total number of ions of 10000 and PMMA coating thickness 0.703 μm on Si substrate using SRIM simulation.

According to [7], breakage of the chemical bonds in polymers occurs by means not only of the nuclear stopping (= nuclear energy loss), but also by electronic stopping (= electronic energy loss) and thus, electronic stopping in polymers (in this case PMMA) can also lead to degradation of the organic host. So, this higher degradation along of the PMMA structure with 90 keV could explain why we see another peak in the plot in the OR (which means, watching the video, another oscillation in the change of the colors of the PMMA during the implantation).

As the level of the degradation of the polymer structure is related with the average penetration depth of the ion in the PMMA (which is also related with the ion species and ion energy), then we can say that the larger the ion range, the larger the number of peaks observed in the OR of the gray scale color change plots. This trend is something that we can see comparing the ion ranges and the number of peaks observed for the different implantations performed in the thinner samples (See Table 2).

Ion Range vs. Number of Peaks					
	$^{1}H^{-}$ at 90 keV	$^{1}H^{-}$ at 30 keV	$^{12}C^{-}$ at 83.4 keV	$^{12}C^{-}$ at 30 keV	$^{74}Ge^{-}$ at 90 keV
Ion Range (μm)	1.12	0.57	0.46	0.17	0.13
Number of peaks	3-2	2	2	1	1

Table 2: Table that shows how the number of peaks in the gray scale plots decreases for smaller ion ranges in the thinner samples (0.703 μm and 0.930 μm)

4.1.3 Color Change under different ion species

Three different ions species were used in this research: hydrogen ($^{1}H^{-}$), carbon ($^{12}C^{-}$) and germanium ($^{74}Ge^{-}$). A first difference related with the different ion species was observed in the four $^{12}C^{-}$ ion implantations at high energy (83.4 keV), where a small increase of the intensity at the end of the DR occurred, as one can see in the comparative example between low and high energy implantations in the Figure 54.

This behaviour (that the implanted zone get shinier, instead of darker for higher doses) was not found in the different sources for this research. However, Popok [7] mentions that metallic lustre appears at high doses ($\geq 1 \cdot 10^{15}\ ion/cm^{-2}$), and the reason is again related with the carbonization process, which produces the red shift of the absorption edge (See Figure 28, subsection 2.7.2) caused by the nanodimensional carbon-enriched clusters. Thus, although this behaviour was not observed for hydrogen and germanium ions at high doses and energies, it makes more sense that this intensity increasing (becoming shinier) occurs just (or maybe faster) with the $^{12}C^{-}$ ion implantations.

Based on the transmission spectra obtained by implanting $^{12}C^{-}$ ions on PMMA at 400 keV (see Figure 28) in the research of Arif et al. [6], one would expect to see in the RGB plots of all implantations that the blue channel would have to be the first one in decrease the intensity, followed by the green one and finally by the red one as the dose increases. However, in my implantations, the order and doses in which they occurred not coincides with such reference, as we can see in the Figure 55.

One clearly observes that the order in which one channel predominates with respect to the other one is not equal for all the ion species. Then, according to my results, there would be an influence of the ion species used in how the irradiated PMMA transmits and absorbs the different wavelengths during the implantation.

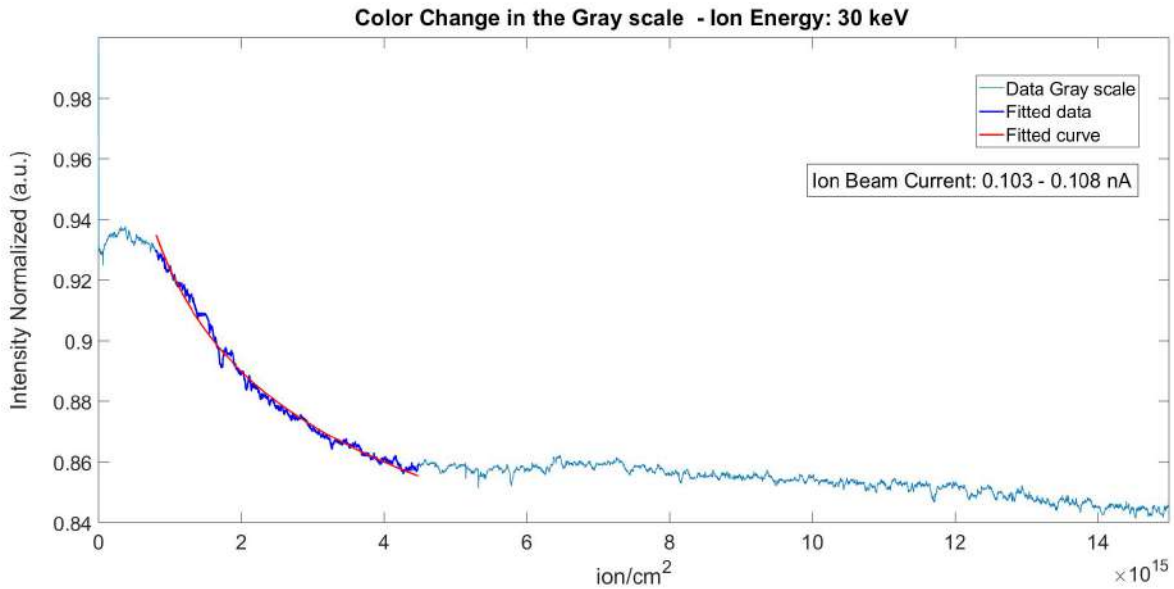

(a)

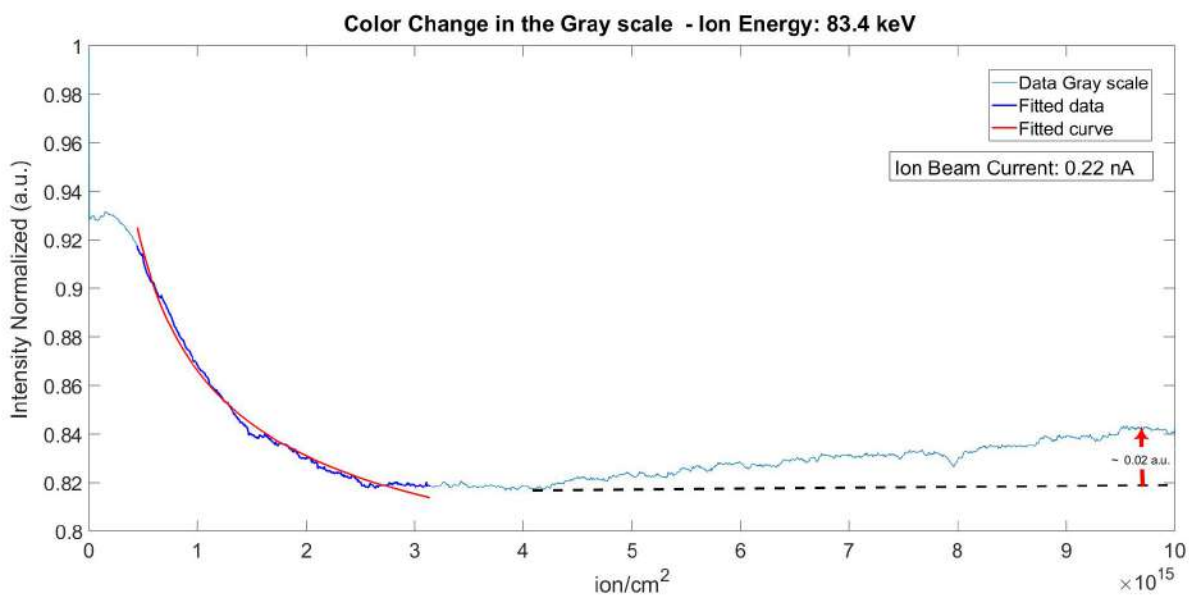

(b)

Figure 54: a) Plot in the gray scale using $^{12}C^-$ implantation at 30 keV with a dose of 1.5E+16 ion/cm^2 on a sample with coating thickness 9.519 μm and b) Plot in the gray scale using $^{12}C^-$ implantation at 83.4 keV with a dose of 1E+16 ion/cm^2 on a sample with coating thickness 9.519 μm. In b) one can see a small increase of the intensity ($\sim$ 0.02 a.u.) at the end of the implantation.

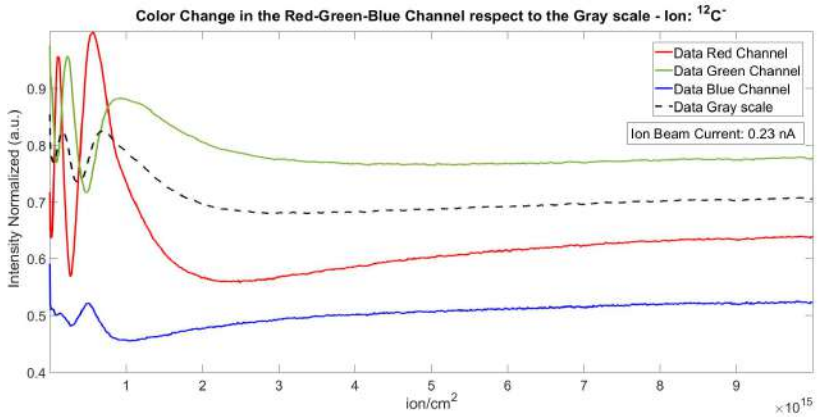

(a)

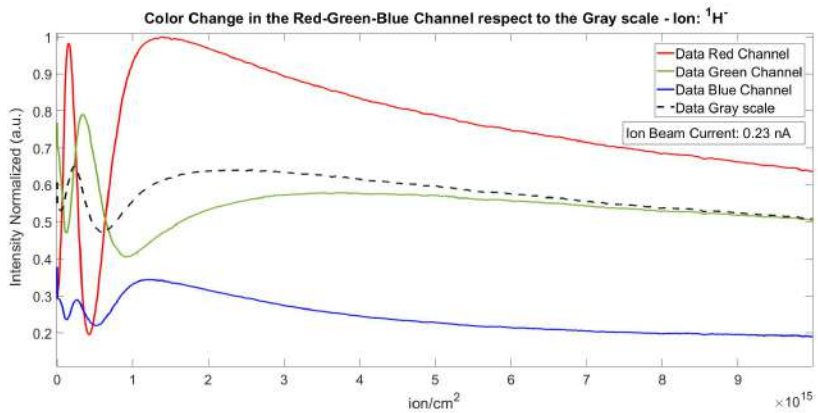

(b)

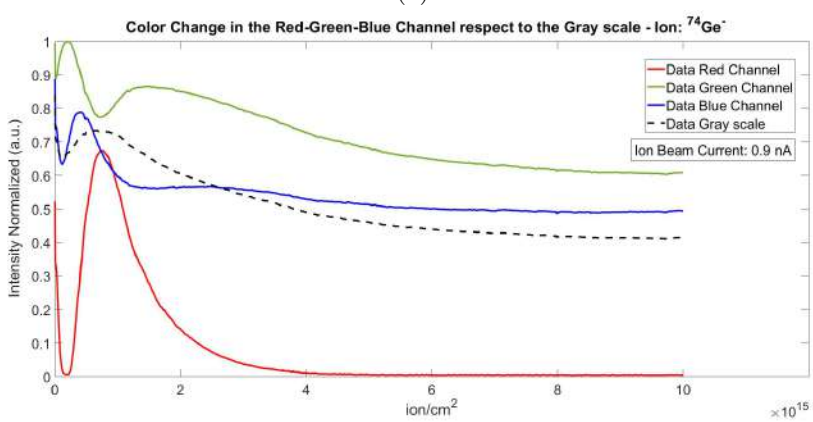

(c)

Figure 55: a) Plot of the RGB channels respect to the gray scale using $^{12}C^-$ implantation at 83.4 keV with a dose of 1E+16 ion/cm^2 and coating thickness 0.703 μm, b) Plot of the RGB channels respect to the gray scale using $^{1}H^-$ implantation at 83.4 keV with a dose of 1E+16 ion/cm^2 and coating thickness 0.703 μm and c)Plot of the RGB channels respect to the gray scale using $^{74}Ge^-$ implantation at 90 keV with a dose of 1E+16 ion/cm^2 and coating thickness 0.930 μm. One can observe that the order in which one color channel predominates respect to the other ones at high doses ($\geq\ 1 \cdot 10^{15}\ cm^{-2}$) depends of the used ion species.

4.2 Topography of the PMMA surface

4.2.1 Thickness change under ion irradiation

As it was described in the section 4.1.1, the behaviour in the OR is different depending of the thickness of the PMMA coating. For the thicker ones, there was not a clear oscillation of the intensity and then no change of the PMMA color during that lapse of time of the implantation. Instead, for the thinner ones, there was an oscillation of the intensity and the PMMA color was changing during the implantation. In the section 4.1.1, I proposed a possible interference effects as an explanation for this color change in the spot because the colors were repeated during the implantation. Thus, something should be happening either with the thickness or with the diffraction index of the PMMA layer. The best way to clear up that was performing height profile measurements on the implanted surface of the PMMA in order to see if there was change after the implantations.

The first spot evaluated for such measurement was the implanted one in the sample 2 (coating thickness 1.864 μm) with germanium ions at dose of 1E+16 ion/cm^2 and at 90 keV. This first measurement was performed with the AFM. The measurement was performed in the edge of the implanted zone in order to see the difference with respect to the surface of the PMMA layer (see Figure 56). The mode used for such measurement was the non-contact mode. The height profile of this spot is shown in the Figure 57.

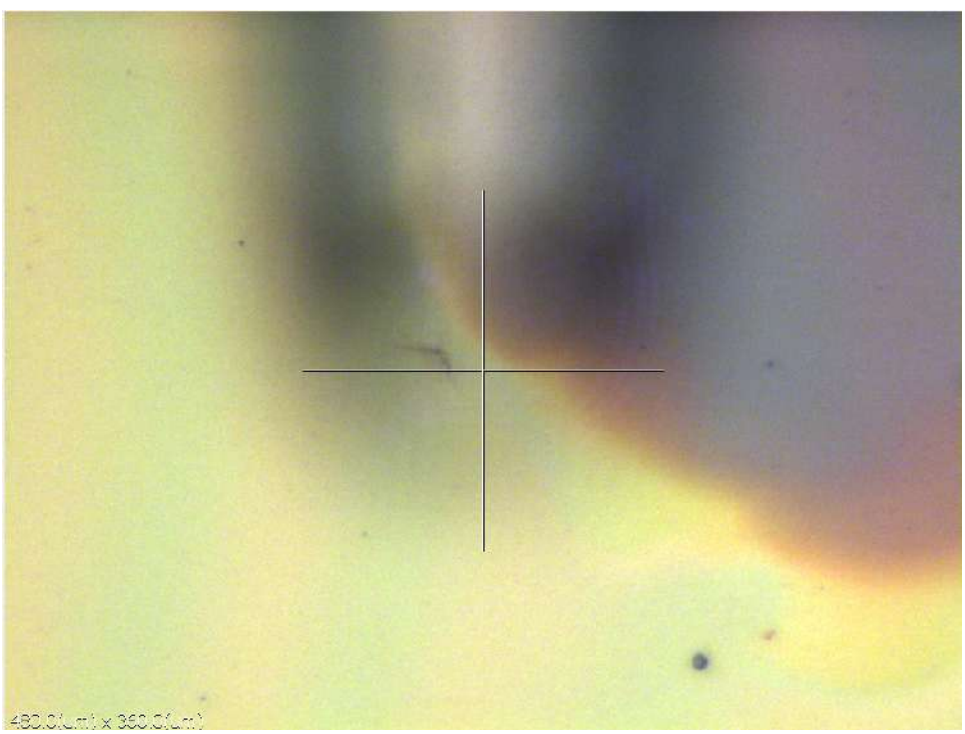

Figure 56: Microscope image of the evaluated zone with the AFM. The measurement was done in the edge of the implanted zone with $^{74}Ge^-$ ion at dose 1E+16 ion/cm^2 and energy of 90 keV in a sample with coating thickness of 1.864 μm

The profile with AFM showed that there is a sinking or compacting in the implanted zone of the PMMA. In this case, the PMMA suffered a sinking of 0.4 μm (or 400 nm), approximately. For the height profile measurements of some other implanted spots of germanium (1E+14 ion/cm^2, 5E+14 ion/cm^2 and 1E+15 ion/cm^2), the DektakXT by BRUKER was used, because this one

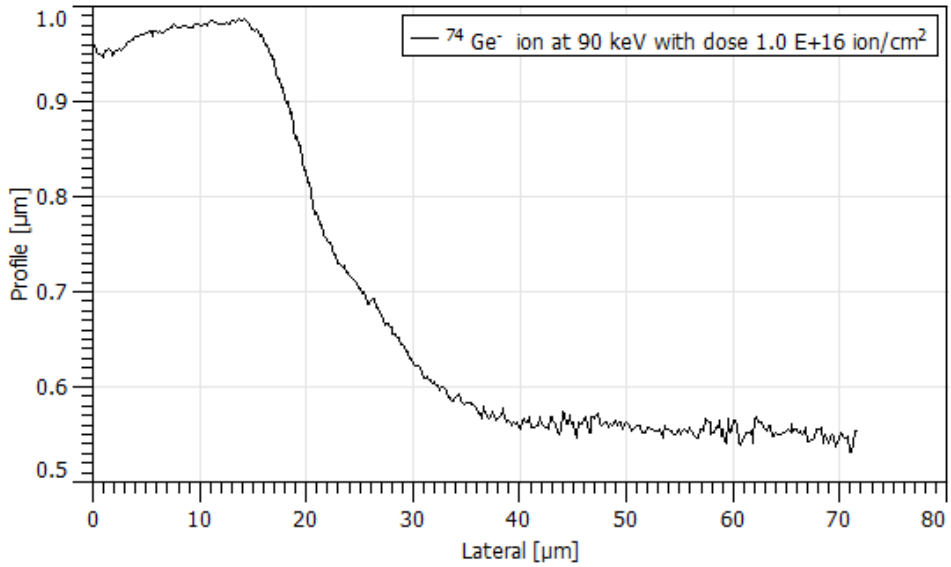

Figure 57: Height profile in the edge of the implanted zone with $^{74}Ge^{-}$ ion at dose 1E+16 and at energy of 90 keV in a sample with coating thickness of 1.864 μm evaluated with the AFM

was accurate enough to measure the sinking of the PMMA in the implanted zone. The same was done with the hydrogen ion. The doses implanted at 83.4 keV in the sample with coating thickness 0.703 μm (sample 5) were: 4.1E+13 ion/cm^2, 2.4E+14 ion/cm^2, 6.1E+14 ion/cm^2 and 2.5E+15 ion/cm^2. These particular doses were chosen for the hydrogen ion because, after the video analysis, these ones corresponded to the peaks and valleys of the oscillation observed in the intensity plot of the gray scale with hydrogen implantation at high energy in the sample 5. For that reason, it was necessary to implant such doses in different spots in order to see if there were some change in the surface of the PMMA layer. As an example of the measurements done with DektakXT, the height profile of the implanted zone with hydrogen ions at different doses is shown in the Figure 58.

The Figure 59 shows how the PMMA sinking changes with respect to the applied dose. The fitting curve which matches best to this behaviour is a power function of the form $f(x) = a * x^b + c$. From the curves is clear that for higher doses, there are deeper PMMA sinkings, but the rate of the PMMA sinking decreases as the dose increases and also it seems that it is going to reach a final PMMA sinking value. It is interesting that the doses in which the sinking values seem not to change anymore coincide with the necessary doses to reach a advanced stage (stage III) in the carbonisation process. These obtained sinkings are in good agreement with Popok [7], who says that degassing and carbonisation phenomena lead to compaction of the implanted layer.

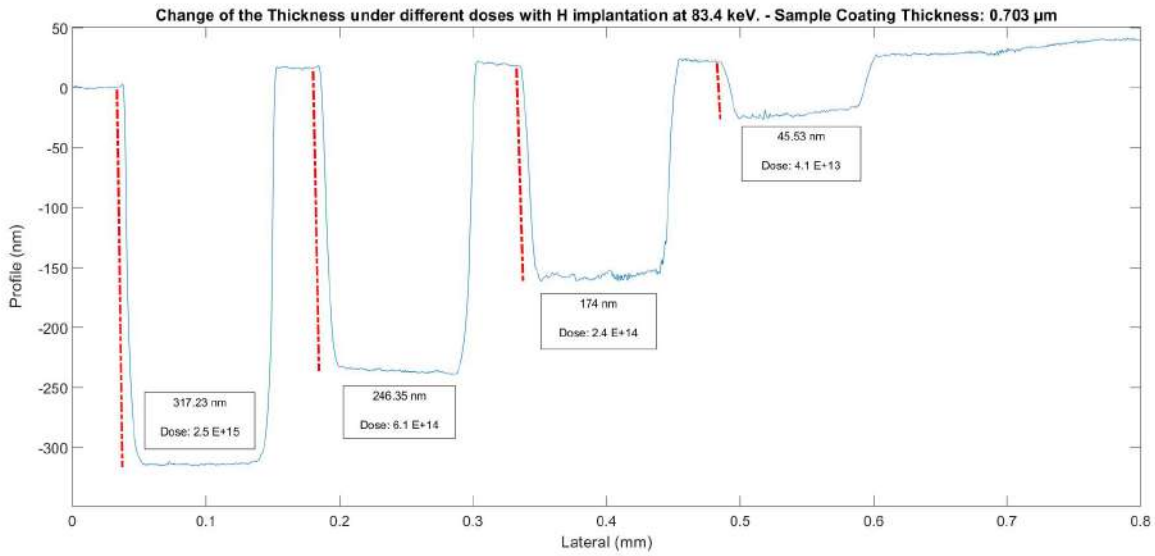

Figure 58: Profilometer of the implanted zone with $^{1}H^{-}$ ion at doses 4.1E+13 ion/cm^2, 2.4E+14 ion/cm^2, 6.1E+14 ion/cm^2 and 2.5E+15 ion/cm^2, at energy of 83.4 keV in the sample 5 (coating thickness: 0.703 μm) evaluated with the DektakXT

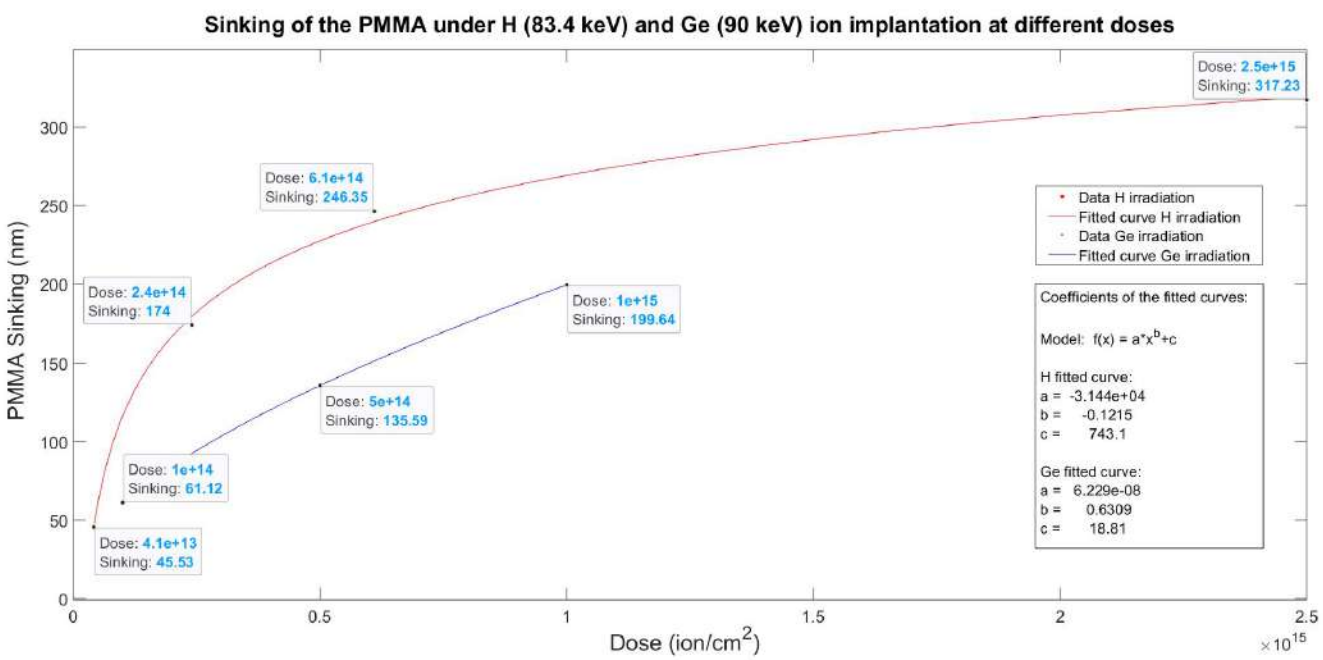

Figure 59: Plot which describes the sinking of the PMMA under different doses, ions ($^{1}H^{-}$ and $^{74}Ge^{-}$) at high energy implantations. The fitted curve for hydrogen (red) and germanium (blue) data is the power function.

4.2.2 Relation between the thickness change and the color change in PMMA

The fact that there is a change of the coating thickness of the PMMA due to the ion implantation could explain the change of color before the decay behaviour starts in the thinner coatings (0.690 μm, 0.703 μm and 0.930 μm). The explanation is based in the interference phenomenon in thin films. One can make some calculations in order to corroborate this statement. Here, we are going to do the calculations for the case of $^{74}Ge^{-}$ ion implanted at 90 keV in the sample with coating thickness of 0.690 μm because the color changes were most pronounced in this implantation. As it was described in the subsubsection 2.6.2, first one needs to identify if the reflected waves coming from the interfaces vacuum-PMMA and PMMA-Silicon are in phase or have a half-cycle phase shift during its reflection. That can be solved knowing the refraction index of each media. The refraction index of vacuum (the media of the chamber where the sample is) is around $n_{vacuum} = 1$; for the PMMA is $n_{PMMA} = 1.49$ [10] and for the silicon wafer is $n_{Si_{(visible\ spectrum)}} > 3.7$ [33]. It is important to mention that many authors that studied the optical properties of the PMMA after ion implantation found that the n_{PMMA} could vary, depending of the ion species, ion energy and dose used in the implantation [3; 4; 5; 30]. However, the values of these new refraction index are between the values of the n_{vacuum} and $n_{Si_{(visible\ spectrum)}}$, so that the following relation always apply:

$$n_{vacuum} < n_{PMMA} < n_{Si_{(visible\ spectrum)}}$$

That implies that the reflected waves coming from the top and the bottom of the PMMA coating layer have a half-cycle reflection phase shift each one. Thus, the half-cycle reflection phase shift produced both in the interface vacuum-PMMA and in the interface PMMA-Si cancel each other and as a consequence there is no a relative phase shift between the two reflected waves. Then, the relation which describes a constructive interference from thin film in this case is (and also taking into account the optical path length inside the PMMA coating layer):

$$2tn_{PMMA} \ = \ m\lambda, \ \ (m = 0, 1, 2, 3 \ldots)$$

$$t \ = \ t_0 - s$$

where λ is the predominant wavelength, t is the thickness of the PMMA at some implanted dose, t_0 is the initial thickness of the PMMA before the implantation and s is the sinking of the PMMA due to the implantation at some dose; all these values in nm. As the source of light used was white light and not a monochromatic one, then the wavelength observed is the one whose constructive interference is predominant.

So, using the fitted equation for the sinking of PMMA under germanium ion implantation which appears in the Figure 59 and selecting some doses in which one can observe distinguishable colors in the video, the calculation of the predominant wavelength was performed. The results are shown in the table 3. The frames from the video at the selected doses for the calculations are shown in the Figure 60.

Calculation of the predominant wavelength λ				
Dose (ion/cm^2)	sinking ($= s$)	$2tn_{PMMA} = 2(t_0 - s)n_{PMMA}$	$m = 0, 1, 2, 3 \ldots$	wavelength λ
1.32E+14	6.93E+01	1.85E+03	4	462 (blue zone)
1.32E+14	6.93E+01	1.85E+03	3	617 (red zone)
2.62E+14	9.66E+01	1.77E+03	3	589 (yellow zone)
4.85E+14	1.33E+02	1.66E+03	3	553 (green zone)
1.17E+15	2.19E+02	1.40E+03	3	468 (blue zone)
1.17E+15	2.19E+02	1.40E+03	2	702 (red zone)

Table 3: Predominant wavelength λ calculated using the interference phenomena in thin films for the germanium ion implantation at 90 keV in the PMMA coating thickness 0.690 μm

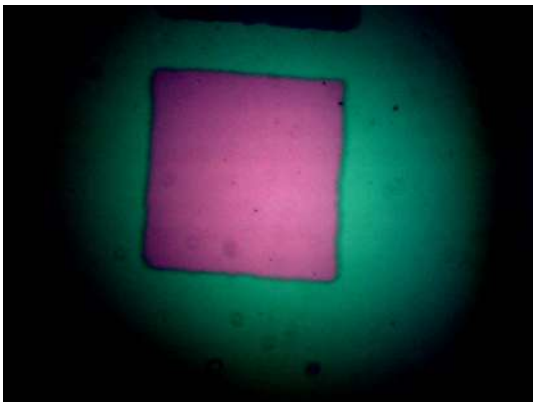

(a) Dose: 1.32 E+14 ion/cm^2

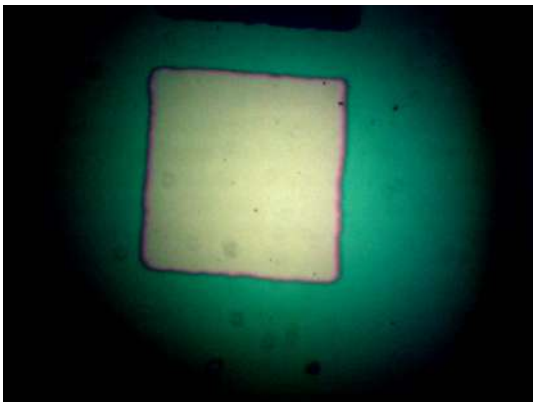

(b) Dose: 2.62 E+14 ion/cm^2

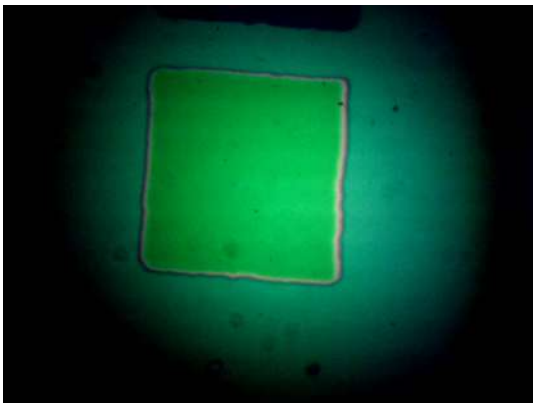

(c) Dose: 4.85 E+14 ion/cm^2

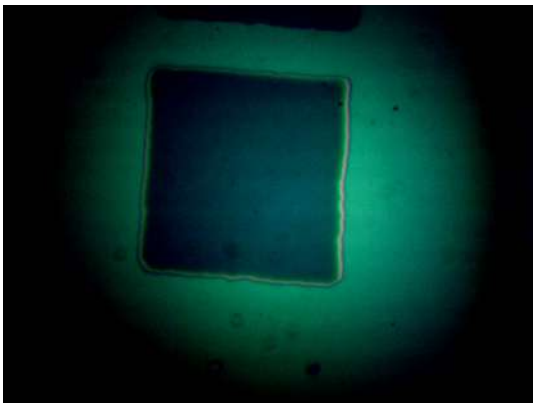

(d) Dose: 1.17 E+15 ion/cm^2

Figure 60: Frames at the selected doses for the calculations of the predominant wavelength from the video of $^{74}Ge^-$ ion implantation at high energy (90 keV) in the sample with coating thickness of 0.690 μm

The value of $m = 3$ was used in the calculation because the sample had an initial thickness (0.690 μm), so that a higher order was applied at the beginning. Then it starts to sink, observing the color transition in the visible spectrum from the red zone to the blue zone. If the thickness of the PMMA could be compacted even more, then we should be able to see again the same color transition, but this time with $m = 2$. One can check this if at the dose 1.17E+15 ion/cm^2 of the Table 3, instead of using $m = 3$, one uses $m = 2$. What one gets is that the value of the wavelength will be 702 nm (red zone, again). In the other direction, if the thickness of the PMMA could get thicker and thicker, then one should be able to see the color transition in the the direction from red zone to blue zone for orders higher than 3. One can check this if at the dose 1.32E+14 ion/cm^2 of the Table 3, instead of using $m = 3$, one uses $m = 4$. What one gets is that the value of the wavelength will be 462 nm (blue zone).

The color of the spot in the frames shown in the Figure 60 match pretty well with the calculated predominant wavelengths at some particular doses, which shows that interference phenomenon in thin films (in this case 0.690 μm, 0.703 μm and 0.930 μm) plays a relevant role in the description of the color change of the PMMA before the effect of the carbonisation plays the predominant role in the color of the PMMA. However, for the thick films (in this research 1.521 μm and 9.519 μm) one did not observe this pattern. The reason, explained by Young and Freedman [28], is that light bulbs emit light in a stream of short bursts, each of which is only a few micrometers long, and if light reflects from the two surfaces of a thick film then the two reflected waves will belong to different bursts. That implies there is no definite phase relationship between different light bursts, so the two waves are incoherent and there is no fixed interference pattern. Also, the thicker the sample, the more higher orders of the different wavelengths come into a constructive interference (with different m values) and so there will not be a predominant wavelength to distinguish.

Just in the frame of the Figure 60.a one can see that the color of the spot not coincide with the calculated predominant wavelength (red zone). Instead, it seems to be in the violet zone of the visible spectrum. If one observe the RGB plot for this implantation (see Figure 61), one could note that the intensities of the blue and red channel do not have the enough difference between each other in order to the red channel predominates, which results in the dark tone of purple observed in the spot at that dose (1.32E+14 ion/cm^2).

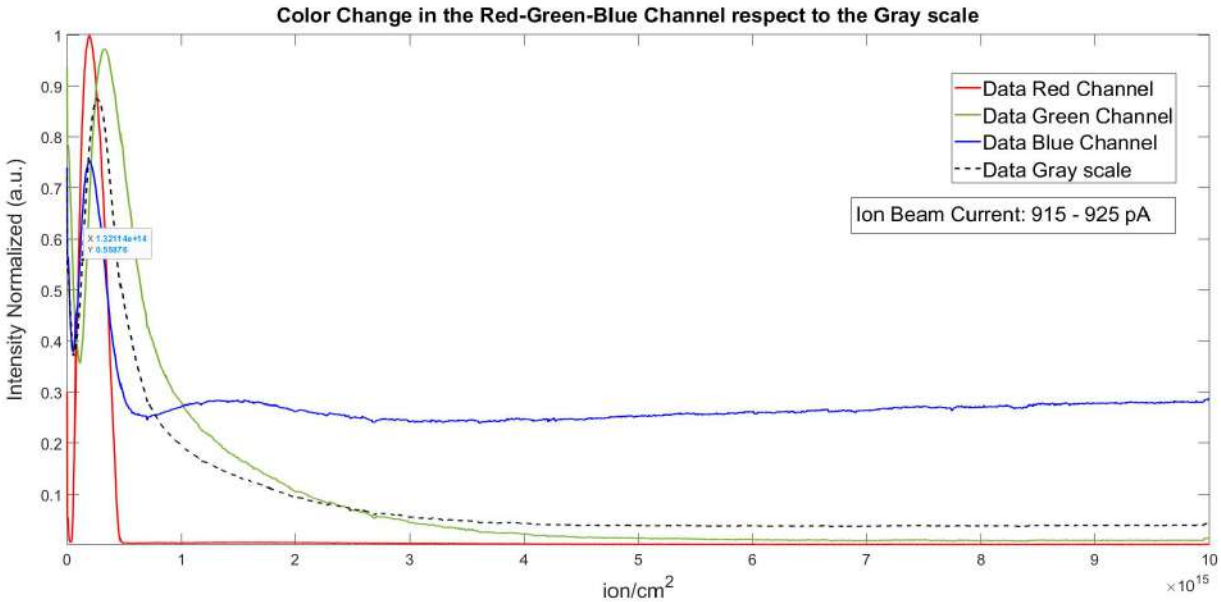

(a)

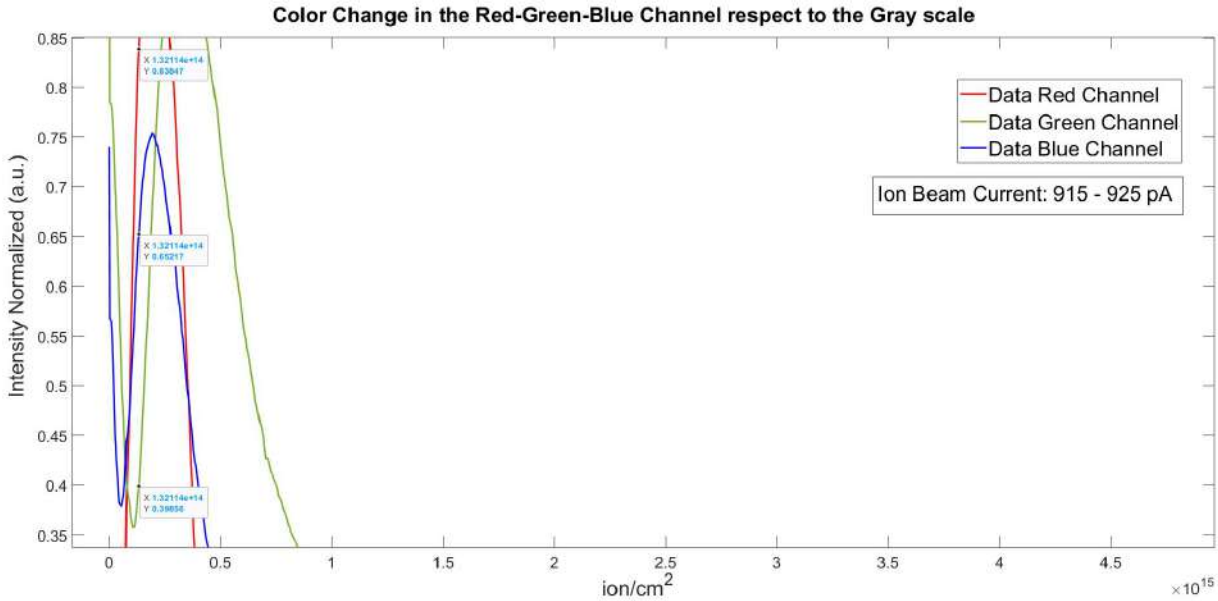

(b)

Figure 61: a) Complete plot of the RGB channels respect to the Gray scale using $^{74}Ge^{-}$ ion implantation at 90 keV on the sample with coating thickness 0.690 μm pointing the dose of the Figure 60.a in the gray scale curve, and b) Zoom of the plot of the RGB channels, which apparently shows that blue and red channel do not have the enough difference in intensity in order that the red channel predominates and thus a dark purple tone appears at 1.32E+14 ion/cm^2 implantation.

5 Conclusions and Outlook

With thicker samples (1.521 μm and 9.519 μm) at the beginning there is no a change of color in the PMMA layer, independently of the ion energy and ion species used in the implantation. But, after a particular dose of the implantation (in the range of 1.48E+14 ion/cm^2 to 4.53E+15 ion/cm^2), one can see a clear darkening of the implanted area (decay of the intensity in the color change plots). This was previously known from the literature, which explains that this darkening is because all these doses are in the stage III of the polymer carbonisation process (between 1.0E+14 ion/cm^2 to 1.0E+16 ion/cm^2), when an aggregation of the carbon clusters up to formation of the quasi-continuous carbonaceous buried layer appears in the implanted area. However, for the thick sample of 1.521 μm there was an exception, because a change of color at the beginning was observed. This case can be explained by the large ion range of the $^1H^-$ ions implanted at 90 keV, which reached a depth of 1.31 μm in PMMA layer causing a large damage in its structure and thus changes in its optical properties.

With thinner samples (0.690 μm, 0.703 μm and 0.930 μm) there is a clear change of color at the beginning (OR), independently of the ion energy and ion species used in the implantation. The Red-Green-Blue (RGB) channel plots in the thinner samples revealed that there is a predominant oscillation of the green and red channels in the range of the doses corresponding to the OR of the gray scale plots. These RGB channel plots also showed that close to the doses in which the green and red channels curves cross each other, one can observe a peak or valley in the gray scale plots. Also, when the peaks of one color channel have a really high value respect with the other color channels, then this color is observed clearly in the video. The blue channel also gives us an additional information to explain why some colors appear in the video, as in the case of the $^{74}Ge^-$ ion implantation at 90 keV in the sample with coating thickness 0.690 μm used as an example in the section 4.2.2. The fact that one can see a change of color in the thinner PMMA coatings with low doses (between 1E+13 ion/cm^2 to 1E+14 $ions/cm^2$) is very helpful in the laboratory as a tool for finding the beam spots specially in such dose range, because one could detect these beam spots quicker.

The number of oscillations of the colors observed in the spot in the thinner samples during the implantation is related with the level of depth at which the damage of the PMMA structure occurs. As the depth of the damage is related with the ion range of the implantation, then the ion species and the ion energy will determine how many oscillations we could see.

Another interesting conclusion from RGB channel plots is that the ion species used influences in how the irradiated PMMA transmits and absorbs the different wavelengths during the implantation, which differs with the literature found that says the carbonization process produced a red shift of the absorption edge, no making distinction of the ion used

The ion implantation on the PMMA surface produce a sinking of it, and it was observed that a higher dose produces a higher PMMA sinking. However, the rate of the PMMA sinking decreases as the dose increases. The sinking of the PMMA surface produced by the ion implantation allows me to conclude that the interference phenomenon plays an important role in the color change of the PMMA in thin films (in this research: 0.690 μm, 0.703 μm and 0.930 μm) before an advanced stage of the carbonisation process (stage III) starts to play a more important role in the color of

the PMMA. As the interference phenomenon can not be observed for thicker films, then this could explain why for the thicker PMMA coatings (in this research: 1.521 μm and 9.519 μm) was not possible to see some change of color before the carbonisation starts to play the important role.

It is recommended to test in thin coating thickness samples more different ions at different doses and energies in order to evaluate how the sinking of PMMA, the oscillation of colors and RGB plots behave.

6 Bibliography

[1] M. Nastasi and J. Mayer, *Ion Implantation and Synthesis of Materials.* Springer, 2006.

[2] N. Semaltianos, "Spin-coated pmma films," *Microelectronics Journal*, vol. 38, no. 6-7, pp. 754–761, 2007.

[3] J. Biersack and R. Kallweit, "Ion beam induced changes of the refractive index of pmma," *Nuclear Instruments and Methods in Physics Research Section B: Beam Interactions with Materials and Atoms*, vol. 46, no. 1-4, pp. 309–312, 1990.

[4] H. Stoyanov, I. Stefanov, S. Russev, G. Tsutsumanova, and G. Hadjichristov, "Optical properties of nano-structured material in ion-implanted polymer," *Bulg. J. Phys*, vol. 40, pp. 193–197, 2013.

[5] R. Gupta, V. Kumar, P. K. Goyal, and S. Kumar, "Optical characterization of poly (methyl methacrylate) implanted with low energy ions," *Applied Surface Science*, vol. 263, pp. 334–338, 2012.

[6] S. Arif, M. S. Rafique, F. Saleemi, R. Sagheer, F. Naab, O. Toader, A. Mahmood, R. Rashid, and M. Mahmood, "Influence of 400 kev carbon ion implantation on structural, optical and electrical properties of pmma," *Nuclear Instruments and Methods in Physics Research Section B: Beam Interactions with Materials and Atoms*, vol. 358, pp. 236–244, 2015.

[7] V. N. Popok, "Ion implantation of polymers: formation of nanoparticulate materials," *Rev. Adv. Mater. Sci*, vol. 30, no. 1, pp. 1–26, 2012.

[8] H. Choi, H. Woo, W. Hong, J. Kim, S. Lee, and C. Eum, "Structural modification of poly (methyl methacrylate) by proton irradiation," *Applied surface science*, vol. 169, pp. 433–437, 2001.

[9] D. Fink, *Fundamentals of Ion-Irradiated Polymers.* Springer, 2004.

[10] J. Mark, *Polymer Data Handbook.* Oxford University Press, 1999.

[11] W. Kern, "The evolution of silicon wafer cleaning technology," *Journal of the Electrochemical Society*, vol. 137, no. 6, pp. 1887–1892, 1990.

[12] M. Itano, F. W. Kern, M. Miyashita, and T. Ohmi, "Particle removal from silicon wafer surface in wet cleaning process," *IEEE Transactions on semiconductor manufacturing*, vol. 6, no. 3, pp. 258–267, 1993.

[13] J. R. Vig, "Uv/ozone cleaning of surfaces," *Journal of Vacuum Science & Technology A: Vacuum, Surfaces, and Films*, vol. 3, no. 3, pp. 1027–1034, 1985.

[14] R. Sherman, "Carbon dioxide snow cleaning," *Particulate Science and Technology*, vol. 25, no. 1, pp. 37–57, 2007.

[15] U. of Louisville, "Spincoatinginfo." https://louisville.edu/micronano/files/document/standard-operating-procedures/SpinCoatingInfo.pdf/view, Oct 2013. Accessed on 08-08-2018.

[16] N. Sahu, B. Parija, and S. Panigrahi, "Fundamental understanding and modeling of spin coating process: A review," *Indian J. Phys*, vol. 83, no. 4, pp. 493–502, 2009.

[17] C. B. Walsh and E. I. Franses, "Thickness and quality of spin-coated polymer films by two-angle ellipsometry," *Thin solid films*, vol. 347, no. 1-2, pp. 167–177, 1999.

[18] C. B. Walsh and E. I. Franses, "Ultrathin pmma films spin-coated from toluene solutions," *Thin Solid Films*, vol. 429, no. 1-2, pp. 71–76, 2003.

[19] E. Mohajerani, F. Farajollahi, R. Mahzoon, and S. Baghery, "Morphological and thickness analysis for pmma spin coated films," *Journal of Optoelectronics and Advanced Materials*, vol. 9, no. 12, p. 3901, 2007.

[20] T. Tippo, C. Thanachayanont, P. Muthitamongkol, C. Junin, M. Hietschold, and A. Thanachayanont, "The effects of solvents on the properties of ultra-thin poly (methyl methacrylate) films prepared by spin coating," *Thin Solid Films*, vol. 546, pp. 180–184, 2013.

[21] J. Ziegler, J. Biersack, and M. Ziegler, *SRIM - The Stopping and Range of Ions in Matter*. SRIM Co., 2008.

[22] J. Küpper, "Änderung des ladungszustandes von nv-zentren durch p-i-p dioden in diamant," Master's thesis, Universität Leipzig - Fakultät für Physik und Geowissenschaften, 2017.

[23] I. für Experimentelle Physik II Universität Leipzig, "Manual of advanced physics laboratory -atomic force microscopy," Oct 2005.

[24] Bruker, *DektakXT Stylus Profiler - User Manual*. May 2011.

[25] K. J. Stout and B. L., *Three-Dimensional Surface Topography*. Penton Press, 2000.

[26] C. for Nano-Micro Manufacturing UC Davis, *Dektak XT 2D Profilometer*. July 2015.

[27] H. Föll, "Advanced materials b part 1: Overview of electronic, magnetic and optical properties of materials." https://www.tf.uni-kiel.de/matwis/amat/admat_en/. Accessed on 21-05-2019.

[28] H. Young and R. Freedman, *Sears and Zemansky's UNIVERSITY PHYSICS : with modern physics*. Addison-Wesley, 2012.

[29] D. Griffiths, *Introduction to Electrodynamics*. Pearson Education, 2014.

[30] W. Hong, H.-J. Woo, H.-W. Choi, Y.-S. Kim, and G.-d. Kim, "Optical property modification of pmma by ion-beam implantation," *Applied surface science*, vol. 169, pp. 428–432, 2001.

[31] S. Balabanov, T. Tsvetkova, E. Borisova, L. Avramov, L. Bischoff, and J. Zuk, "Optical properties of si+ implanted pmma," in *Journal of Physics: Conference Series*, vol. 223, p. 012032, IOP Publishing, 2010.

[32] ALLRESIST, "Ar-p 630 ...670." http://www.allresist.com/ebeamresists-ar-p-631-679/, Jan 2014. Accessed on 05-06-2019.

[33] D. E. Aspnes and A. A. Studna, "Dielectric functions and optical parameters of si, ge, gap, gaas, gasb, inp, inas, and insb from 1.5 to 6.0 ev," *Phys. Rev. B*, vol. 27, pp. 985–1009, Jan 1983.

7 Appendix

7.1 Appendix A: Table of the dose values before the decay of the intensity starts

Ion: $^{1}H^{-}$			
	30 keV. at 3E+16	90 keV. at 1E+16	83.4 keV. at 1E+16
9.519 μm	1.22 E+15 ion/cm^2	6.18 E+14 ion/cm^2	—
1.521 μm	8.54 E+14 ion/cm^2	1.58 E+15 ion/cm^2	—
0.930 μm	4.37 E+15 ion/cm^2	1.98 E+15 ion/cm^2	—
0.703 μm	4.53 E+15 ion/cm^2	—	2.59 E+15 ion/cm^2
Ion: $^{12}C^{-}$			
	30 keV. at 1.5E+16	83.4 keV. at 1E+16	
9.519 μm	3.79 E+14 ion/cm^2	1.48 E+14 ion/cm^2	
1.521 μm	3.21 E+14 ion/cm^2	1.54 E+14 ion/cm^2	
0.930 μm	1.09 E+15 ion/cm^2	1.23 E+15 ion/cm^2	
0.703 μm	6.37 E+14 ion/cm^2	6.97 E+14 ion/cm^2	
Ion: $^{74}Ge^{-}$			
	90 keV. at 1E+16		
9.519 μm	2.09 E+14 ion/cm^2		
0.930 μm	6.62 E+14 ion/cm^2		
0.690 μm	2.62 E+14 ion/cm^2		

7.2 Appendix B: Table of coefficients of the fitting curves

Coefficients of the fitting curves with the form $f(x) = a * x^b + c$	
Figure 39	a = -3.607E-08 b = 0.462 c = 1.365
Figure 40	a = -1.075E-09 b = 0.5216 c = 1.009
Figure 41	a = 2.985E+11 b = -0.7526 c = 0.02782
Figure 45	a = -7.138E-11 b = 0.6247 c = 1.178
Figure 46 and Figure 49.a	a = -1.627E-12 b = 0.7078 c = 1.124
Figure 49.b	a = -0.001996 b = 0.1717 c = 2.027
Figure 50.a	a = 6.531E+07 b = -0.5555 c = 0.613
Figure 50.b	a = 3.403E+04 b = -0.3219 c = 0.4552
Figure 53.a	a = 159.8 b = -0.1833 c = 0.6395
Figure 53.b	a = 1.994E+06 b = -0.4804 c = 0.7422

8 Acknowledgements

After many days of work in this thesis, I have been able to reach the goal that I set four years ago: graduate with a bachelor's degree in physics abroad. I have to say that these four years were a long and a hard journey, and it is for that reason that I have only to thank all those people who helped me and supported me during all this time.

First of all, I have to thank eternally my family, my mother Maria Esther Aguilar, my father Marco Bassallo and my sister Claudia Bassallo, who all the time supported me in every sense and in any moment that I needed it.

Also, I have to thank the Abteilung Angewandte Quantensysteme, like Prof. Dr. Jan Meijer for accepting me into the group as the head of the department, as well as Tobias Lühmann and many other members who helped me with their suggestions and the experimental part of the thesis.

I have special thanks to Dr.-Ing. Michael Kieschnick, who was with whom more closely I worked in the thesis. Thanks so much for all your suggestions, advices, corrections and time during the thesis, which helped me and will help me for the rest of my professional life.

There were several persons out of my department who support me with the measurements. From the Abteilung Halbleiterphysik, I have to start with Prof. Dr. Marius Grundmann and Prof. Dr. habil. Michael Lorenz, who coordinated with the other members of the department in order to use some of their equipments. I have to thank M. Sc. Stefan Hohenberger for helping me with the Atomic Force Microscopy measurements, as well as to M.Sc. Max Kneiss, Dr. Peter Schlupp and Dr. Daniel Splith for helping me with the DektakXT measurements. Another person to whom I am very grateful is to my friend Marvin Mellado, who helped me with the programming language that I needed in MATLAB.

After remembering all the contribution and help that you gave me in the thesis and during these four years, I have nothing left to say again: thank you very much!!

9 Statement of authorship

I hereby certify that this bachelor thesis has been composed by myself and describes my own work, unless otherwise acknowledged in the test. All references and verbatim extracts have been quoted and all sources of information have been specifically acknowledged. It has not been accepted in any previous application for a degree.

Leipzig, September 2019 Mauricio Omar Bassallo Aguilar